

# Influence of a cavity on the dynamical behaviour of an airfoil

**Citation for published version (APA):**

Olsman, W. F. J. (2010). *Influence of a cavity on the dynamical behaviour of an airfoil*. [Phd Thesis 1 (Research TU/e / Graduation TU/e), Applied Physics]. Technische Universiteit Eindhoven. <https://doi.org/10.6100/IR673149>

**DOI:**

[10.6100/IR673149](https://doi.org/10.6100/IR673149)

**Document status and date:**

Published: 01/01/2010

**Document Version:**

Publisher's PDF, also known as Version of Record (includes final page, issue and volume numbers)

**Please check the document version of this publication:**

- A submitted manuscript is the version of the article upon submission and before peer-review. There can be important differences between the submitted version and the official published version of record. People interested in the research are advised to contact the author for the final version of the publication, or visit the DOI to the publisher's website.
- The final author version and the galley proof are versions of the publication after peer review.
- The final published version features the final layout of the paper including the volume, issue and page numbers.

[Link to publication](#)

**General rights**

Copyright and moral rights for the publications made accessible in the public portal are retained by the authors and/or other copyright owners and it is a condition of accessing publications that users recognise and abide by the legal requirements associated with these rights.

- Users may download and print one copy of any publication from the public portal for the purpose of private study or research.
- You may not further distribute the material or use it for any profit-making activity or commercial gain
- You may freely distribute the URL identifying the publication in the public portal.

If the publication is distributed under the terms of Article 25fa of the Dutch Copyright Act, indicated by the "Taverne" license above, please follow below link for the End User Agreement:

[www.tue.nl/taverne](http://www.tue.nl/taverne)

**Take down policy**

If you believe that this document breaches copyright please contact us at:

[openaccess@tue.nl](mailto:openaccess@tue.nl)

providing details and we will investigate your claim.

# Influence of a cavity on the dynamical behaviour of an airfoil



W.F.J. Olsman



INFLUENCE OF A CAVITY ON THE DYNAMICAL  
BEHAVIOUR OF AN AIRFOIL

Copyright © 2010 W.F.J. Olsman  
Cover design by W.F.J. Olsman  
Printed by Universiteitsdrukkerij TU Eindhoven, Eindhoven,  
The Netherlands

A catalogue record is available from the Eindhoven University of  
Technology Library

Olsman, W.F.J.

Influence of a cavity on the dynamical behaviour of an airfoil / by Willem  
Frederik Jurriën Olsman. – Eindhoven : Technische Universiteit Eindhoven,  
2010. – Proefschrift.  
ISBN: 978-90-386-2230-9  
NUR: 968

Trefwoorden: caviteit / trapped vortex / dynamisch gedrag vleugel / vleugel  
Subject headings: cavity / trapped vortex / dynamical behaviour wing /  
wing

INFLUENCE OF A CAVITY ON THE DYNAMICAL  
BEHAVIOUR OF AN AIRFOIL

PROEFSCHRIFT

ter verkrijging van de graad van doctor aan de  
Technische Universiteit Eindhoven, op gezag van de  
rector magnificus, prof.dr.ir. C.J. van Duijn, voor een  
commissie aangewezen door het College voor  
Promoties in het openbaar te verdedigen  
op dinsdag 25 mei 2010 om 16.00 uur

door

Willem Frederik Jurriën Olsman

geboren te Hilversum

Dit proefschrift is goedgekeurd door de promotoren:

prof.dr.ir. G.J.F. van Heijst

en

prof.dr.ir. A. Hirschberg

Copromotor:

dr.ir. R.R. Trieling

Part of this research has been supported by the European project VortexCell2050 within the Sixth Framework, under contract number AST4-CT-2005-012139.

# Contents

<b>Contents</b>	<b>vii</b>
<b>1 Introduction</b>	<b>1</b>
<b>2 Theoretical considerations</b>	<b>7</b>
2.1 Oscillating object versus oscillating flow . . . . .	7
2.2 Linearised thin airfoil theory . . . . .	8
2.3 Effect of finite airfoil thickness . . . . .	17
2.4 Apparent mass . . . . .	20
2.5 Wall interference effects . . . . .	22
2.6 Numerical methods . . . . .	23
2.6.1 Discrete vortex method . . . . .	23
2.6.2 Solutions of Euler equations . . . . .	25
2.6.3 Navier–Stokes solutions . . . . .	28
<b>3 Experimental method</b>	<b>33</b>
3.1 Introduction . . . . .	34
3.2 Experimental method . . . . .	35
3.3 Acoustics without main flow . . . . .	39
3.3.1 Infinite duct . . . . .	40
3.3.2 Acoustical validation setup . . . . .	40
3.3.3 Finite duct . . . . .	41
3.3.4 Test section with wing installed . . . . .	45
3.3.5 Test section in wind tunnel without wing . . . . .	47
3.3.6 Test section in wind tunnel with wing installed . . . . .	49
3.3.7 Determination of the transversal velocity . . . . .	50
3.4 Numerical method for flow field . . . . .	51
3.5 Measurements on a NACA0018 airfoil . . . . .	52



3.5.1	Steady flow . . . . .	52
3.5.2	Unsteady flow . . . . .	53
3.5.3	Estimation of plunging velocity . . . . .	55
3.5.4	Relation to plunging motion . . . . .	56
3.5.5	Dependency of $\Delta C_{pu}$ on excitation amplitude . . . . .	57
3.6	Conclusion . . . . .	58
<b>4</b>	<b>Numerical simulation of flow without forcing</b>	<b>61</b>
4.1	Introduction . . . . .	61
4.2	Numerical method based on Euler equations . . . . .	63
4.3	Numerical method based on Navier–Stokes . . . . .	68
4.4	Experimental facility . . . . .	71
4.5	Results . . . . .	72
4.5.1	NACA0018 . . . . .	72
4.5.2	NACA0018 with cavity . . . . .	77
4.6	Conclusion . . . . .	84
<b>5</b>	<b>Flow visualisation and three-dimensional flow effects</b>	<b>87</b>
5.1	Water channel setup . . . . .	87
5.2	Cavity modes . . . . .	88
5.3	Three-dimensional flow effects . . . . .	93
5.3.1	Two closed end plates . . . . .	93
5.3.2	One end plate removed . . . . .	95
5.3.3	External forcing . . . . .	97
5.4	Conclusion . . . . .	98
<b>6</b>	<b>Airfoils with cavities and applied forcing</b>	<b>101</b>
6.1	Introduction . . . . .	101
6.2	Numerical results of Navier–Stokes method . . . . .	103
6.2.1	Clean airfoil . . . . .	104
6.2.2	Airfoil with cavity A . . . . .	107
6.2.3	Airfoil with cavity B . . . . .	107
6.3	Wind tunnel experiments . . . . .	109
6.3.1	Steady flow . . . . .	109
6.3.2	Hot-wire anemometry . . . . .	112
6.3.3	Unsteady flow . . . . .	122
6.4	Conclusion . . . . .	125
<b>7</b>	<b>Conclusions</b>	<b>127</b>

<b>A</b>	<b>Geometry of NACA0018 airfoils</b>	<b>131</b>
<b>B</b>	<b>Added mass of a flat plate</b>	<b>134</b>
<b>C</b>	<b>Kármán–Trefftz airfoil</b>	<b>138</b>
	C.1 Quasi-steady solution . . . . .	139
	C.2 Added mass . . . . .	140
<b>D</b>	<b>Pressure difference without Kutta condition</b>	<b>141</b>
<b>E</b>	<b>Lock-in method</b>	<b>143</b>
<b>F</b>	<b>Hot-wire measurements for cavity <math>B</math></b>	<b>145</b>
	<b>Bibliography</b>	<b>153</b>
	<b>Summary</b>	<b>159</b>
	<b>Samenvatting</b>	<b>161</b>
	<b>Dankwoord</b>	<b>163</b>
	<b>Curriculum Vitae</b>	<b>165</b>



# Chapter 1

## Introduction

Ever since the early days of the first successful heavier-than-air flight by the Wright brothers, the aircraft industry has grown rapidly. This rapid growth was accompanied by faster, more advanced and larger aircraft. It is expected that the trend for larger aircraft will continue, and hence future aircraft will be huge. One of the consequences of such very large aircraft is that the emphasis in the design will be on the structural strength rather than on aerodynamic efficiency. With identical material an increase in weight scales with approximately the third power of the typical length scale, while structural strength scales with the square of the typical length. Therefore these future aircraft will need thick wings (to provide stiffness) compared to conventional airfoils in use nowadays. However, thick wings promote flow separation, which will degrade the aerodynamic performance. The contradictory design requirements of structural strength versus aerodynamic efficiency will call for a thick wing without flow separation. Such a wing has been the subject of study within the project VortexCell2050. This project was funded by the European Community within its Sixth Framework program. The idea pursued in the project is to suppress massive vortex shedding by trapping a vortex inside a cavity in the airfoil. Figure 1.1 shows such an airfoil with a cavity as considered in the project. The idea is that separation is not too detrimental as long as one prevents the shedding of large scale-vortices. It is also possible to consider the opening of the cavity as a moving wall, which prevents the boundary layer from slowing down. An idealised illustration of successful vortex trapping is shown in figures 1.2(a) and 1.2(b). In figure 1.2(a) a thick airfoil is shown which displays a massive separation of the boundary layer on the upper surface. Figure

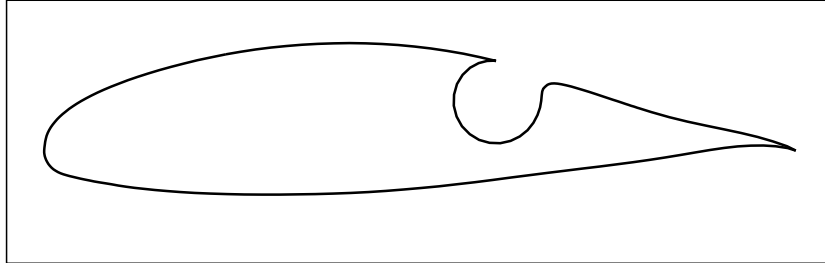


**Figure 1.1** – Graphical illustration of an airfoil with vortex trapping cavity considered in the VortexCell2050 project.

1.2(b) shows the same airfoil for the same flow conditions, but here a cavity is placed in the airfoil. The flow separates from the upstream edge of the cavity and reattaches on the downstream edge of the cavity, with a vortex trapped inside the cavity. Within the Vortexcell2050 project also flow control is considered to stabilise the flow. However, in this thesis we will not consider flow control.

The concept of a trapped vortex was inspired by Kasper’s Vortex wing design. This vortex trapping airfoil is shown in figure 1.3. Kasper claimed to achieve significant higher aerodynamic efficiency (lift over drag ratio) by trapped vortices on the wing of a glider. However, wind tunnel tests performed by Kruppa (1977) did not confirm this claim and demonstrated that the vortex wing’s performance was lower than that of a conventional airfoil, in terms of maximum lift to drag ratio. It was suggested that the discrepancy between the wind tunnel experiments and the claimed flow with trapped vortices was due to the Reynolds number being too low during the wind tunnel tests. Although the wind tunnel measurements did not confirm higher aerodynamic efficiency, many theoretical studies have shown that wings with trapped vortices can have significant benefits over a conventional airfoil, see Saffman & Sheffield (1977); Rossow (1978); Huang & Chow (1982). These theoretical results motivate the search for real airfoils with trapped vortices.

A large amount of literature is available for the case of grazing flow over rectangular cavities in plane walls, see Rockwell & Naudasher (1978, 1979). However, only a limited number of studies have been devoted to cavities with circular shapes or cavities mounted on objects, e.g. a wing with a vortex trapping cavity. Worth mentioning here are the studies of Fletcher & Stewart (1986); Baranov *et al.* (2000); Isaev *et al.* (2000). For rectangular cavities in plane walls the literature reports two main flow in-

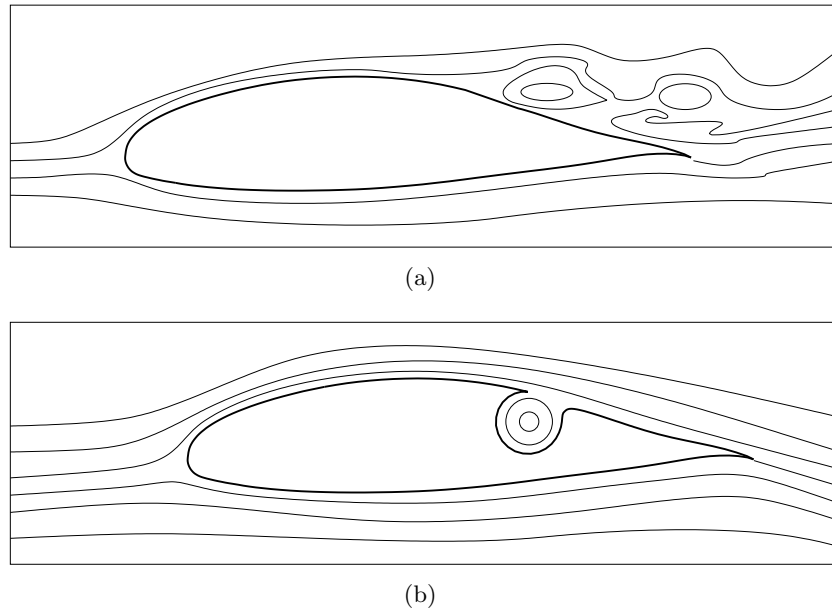


**Figure 1.2** – Graphical illustration of streamlines over a thick airfoil with massive flow separation (a) and the same airfoil with attached flow and a vortex trapped inside a cavity (b).

stabilities, namely, the shear layer instability mode and the cavity wake mode. The shear layer mode is most commonly encountered in experiments and is related to the Kelvin Helmholtz instability of the shear layer separating the low velocity flow inside the cavity and the high velocity flow outside. In figures 1.4(a) and 1.4(b) the first and second shear layer mode are illustrated. The wake mode is described in Gharib & Roshko (1987) but is rarely observed in experiments due to its sensitivity to perturbations. An illustration of the wake mode is given in figure 1.4(c). It corresponds to the build up of a large vortex deep in the cavity followed by a sudden shedding of the entire vortex. This process is then repeated periodically.

An important phenomenon in modern wing design is prevention of wing flutter. Flutter is a self-sustained oscillation of the wing, due to a coupling of mechanical vibration modes of the wing with the unsteady aerodynamic forces on the wing. Wing flutter can be hazardous and many aircraft have crashed due to wing flutter in the past, for references see Fung (1955). For this reason knowledge of the unsteady forces on a wing is crucial for successful wing design. For conventional wings the linear theory proposed

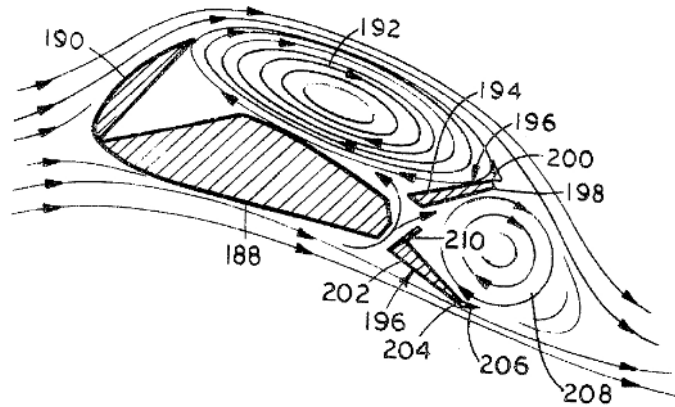


**Figure 1.3** – Sketch of streamlines around the Kasper vortex wing, with two trapped vortices. From US patent No. 3,831,885.

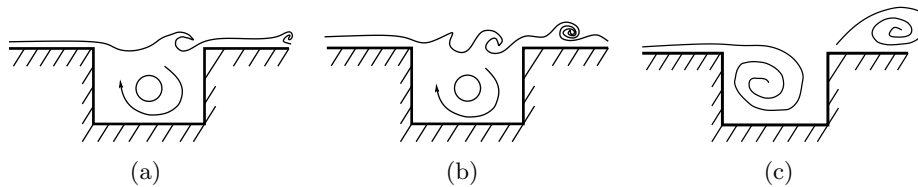


**Figure 1.4** – Graphical illustration of the first shear layer mode (a), the second shear layer mode (b) and the cavity wake mode (c).

by Theodorsen (1935) has been applied successfully and is the standard in classical wing flutter analysis. However, a wing with a vortex trapping cavity may give rise to a dynamical behaviour that is not captured by Theodorsen's theoretical model. Based on the aforementioned literature about cavity flows we can expect oscillations of the shear layer over the cavity. These oscillations may be enhanced by (and/or couple with) vibrations of the wing, possibly leading to high amplitude oscillatory forces on the wing and a dynamical behaviour very different from that of a conventional wing without cavity. Shear layer modes are expected to occur at Strouhal numbers, based on the cavity width and the main flow velocity, of order unity, see Rockwell & Naudasher (1978, 1979). Due to the rather high Strouhal numbers of these phenomena, they are not anticipated to affect classical wing bending-torsion flutter modes, but they could potentially contribute to undesirable high-frequency structural vibrations. We developed a new experimental method allowing to study the unsteady flow

around an airfoil oscillating at such high Strouhal numbers. The key idea is to place a fixed airfoil in an acoustically driven oscillating flow rather than to make the airfoil oscillate.

In this thesis the dynamical behaviour of a wing with a cavity will be investigated and compared to a conventional airfoil without cavity. We will focus on oscillations of the airfoil in the direction perpendicular to the main flow, this is known as a plunging motion. For this investigation we will use wind tunnel and water channel experiments, complemented with numerical simulations.

## **Thesis outline**

This thesis consists of seven chapters and is organised as follows. First, in Chapter 2, the analytical model of Theodorsen (1935) for the plunging motion of a flat plate is introduced. This analytical model will be used throughout this thesis as a reference. In this chapter several corrections to the original analytical model will be discussed. Also the numerical tools that will be used are introduced. Then, in Chapter 3, the experimental technique to perform measurement of a dynamical plunging airfoil, at high values of the reduced frequency, is presented. This new method is validated by measurements carried out for a standard airfoil without cavity and the results are compared to results from a numerical method for two-dimensional flow. The results of numerical simulations for two-dimensional flow at low Reynolds number around an airfoil with and without cavity, in the absence of external forcing, are discussed in Chapter 4. These numerical results are complemented by flow visualisations in a water channel for an airfoil with cavity, which is the subject of Chapter 5. Here also three-dimensional aspects of the flow over an airfoil with a cavity are discussed. The effects of external forcing on an airfoil with cavity are treated in Chapter 6, both numerically and experimentally. Finally the main results are summarised in Chapter 7.





## Chapter 2

# Theoretical considerations

This chapter introduces an analytical method for the unsteady flow around an oscillating flat plate as well as the used terminology. In the experiments, which are described in the next chapter, the flow is oscillating and the airfoil is fixed to the wind tunnel. Therefore this chapter starts with a brief discussion about the fundamental difference between an oscillating object in a steady flow and a fixed object in an oscillating flow, see section 2.1. Thereafter in section 2.2 the theoretical solution for an oscillating flat plate in a steady flow will be presented. We will use this theory throughout the thesis as a reference. Various corrections and details of this theoretical method are discussed in sections 2.3 to 2.5. And lastly, the numerical methods used in this thesis are introduced in section 2.6.

### 2.1 Oscillating object versus oscillating flow

We compare the flow around an oscillating object in an unbounded fluid observed by an observer fixed with respect to the fluid at large distance from the object to the same flow observed by an observer fixed to the object. In both cases the observed velocity fields around the object are identical, however, the pressure fields are not. The fundamental difference between the two cases is the presence of a time dependent uniform pressure gradient in the case of an observer fixed to the object. This pressure gradient is necessary to accelerate the fluid.

We assume the first reference system to be inertial. If we use a coordinate system which is fixed to the object and moving along with it one should be aware that one is now in an accelerating coordinate system, which

introduces extra terms in the equations of motion. In Streeter (1961) this is explained in detail. The acceleration  $\vec{a}$  relative to inertial space is:

$$\vec{a} = \frac{D\vec{W}}{Dt} + \vec{S} + 2\vec{\Omega} \times \vec{W} + \vec{\Omega} \times (\vec{\Omega} \times \vec{r}) + \frac{d\vec{\Omega}}{dt} \times \vec{r}, \quad (2.1)$$

where  $\vec{S}$  and  $\vec{\Omega}$  are respectively the acceleration and angular velocity of the coordinate system,  $\vec{W}$  is the velocity in the accelerating reference frame and  $\vec{r}$  is the position.  $\frac{D\vec{W}}{Dt}$  is the acceleration perceived by an observer in the accelerating coordinate system. The remaining terms are contributions due to the accelerating coordinate system. In the absence of rotation only the first two terms in equation 2.1 remain.

The effect of an oscillating flow on the force on an object is identical to the Archimedes force in a time dependent gravitational field, as described in Batchelor (1967) (page 177).

## 2.2 Linearised thin airfoil theory

The problem of an oscillating airfoil has been the subject of study for a long time. A major breakthrough in the understanding of the unsteady forces on an oscillating airfoil was accomplished by Theodorsen (1935), who found an analytical solution of the problem by using linearised potential flow theory. A brief description of this linear theory will be given here. More elaborate treatments can be found in Fung (1955) or Sears & Von Kármán (1938). In this section the analysis of Fung (1955) is followed. Later on in the thesis we will refer to the theory described in this section as “Theodorsen’s theory”.

The problem is illustrated in figure 2.1 below. A flat plate with chord  $c$ , centered at the origin, with zero thickness and infinite span in the  $z$ -direction, indicated by the thick solid line, performs a prescribed oscillation in the direction normal to the oncoming flow (the  $y$ -direction) with uniform velocity  $U_\infty$ . We assume a two-dimensional flow. Due to the unsteady motion vorticity is shed from the trailing edge of the plate, which results in the formation of a vortex sheet, with strength  $\gamma(x, t)$ . The aim of the analysis is to find the aerodynamic forces on the plate. The problem can be formulated and solved separately for translational (plunging) and rotational (pitching) motion. Only the translational case will be discussed here because this will be the main focus of our experiments.

The problem will be solved by using the acceleration potential, denoted by  $\phi_{ac}$ , where the underscript  $ac$  is added to prevent confusion with the ve-

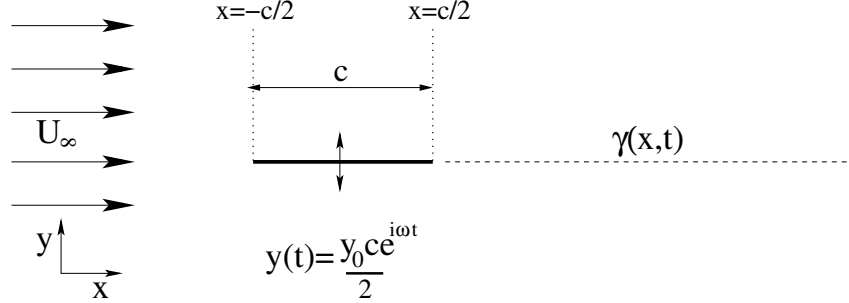


**Figure 2.1** – Oscillating flat plate in a steady oncoming flow with uniform velocity  $U_\infty$ .

locity potential. This means that the acceleration of the fluid  $\vec{a} = (a_x, a_y)$  is given by the gradient of the acceleration potential  $\vec{a} = \nabla\phi_{ac}$ . The advantage of using the acceleration potential is that it is continuous across the wake, in contrast to the velocity potential which is discontinuous across the wake. Similar to the velocity potential, the acceleration potential for small perturbations in an incompressible irrotational flow is governed by the Laplace equation. Assume a two-dimensional incompressible inviscid flow around a flat plate of zero thickness, with chord  $c$ , stretching from  $x = -c/2$  to  $x = c/2$  and a mean fluid flow with velocity  $(U_\infty, 0)$ . The velocity of the fluid is given by  $(U_\infty + u', v')$ , where  $u'$  and  $v'$  are small velocity perturbations in the  $x$  and  $y$ -direction, respectively. In this section primed variables will indicate perturbations. Neglecting second and higher-order terms the acceleration of a fluid particle is given by

$$a'_x = \frac{\partial u'}{\partial t} + U_\infty \frac{\partial u'}{\partial x}, \quad (2.2)$$

$$a'_y = \frac{\partial v'}{\partial t} + U_\infty \frac{\partial v'}{\partial x}. \quad (2.3)$$

Neglecting second-order and higher terms is appropriate if the amplitudes of the velocities  $|u'|$  and  $|v'|$  are small with respect to  $U_\infty$ . From a physical point of view this means that the vorticity shed from the trailing edge of the plate is relatively weak and as a consequence the effect of roll-up of the wake can be neglected, which justifies treating the wake as a straight vortex sheet. Similar to the complex velocity potential one can also construct a complex acceleration potential  $w = \phi_{ac} + j\psi_{ac}$ , where  $j^2 = -1$  and  $\psi_{ac}$  is the acceleration stream function. The boundary conditions require that the acceleration and velocity of the fluid normal to the plate are equal to the

acceleration and velocity of the plate normal to itself respectively, i.e.

$$v' \Big|_{\text{plate}} = \frac{dy_{\text{plate}}}{dt}, \quad (2.4)$$

$$a'_y \Big|_{\text{plate}} = \frac{\partial \phi_{ac}}{\partial y} \Big|_{\text{plate}} = \frac{d^2 y_{\text{plate}}}{dt^2}. \quad (2.5)$$

In inviscid flow theory, the velocity becomes infinite at sharp edges, such as the trailing edge of a flat plate. Experimental observations, however, do not display these infinite velocities. In a real fluid the flow separates at these sharp edges and a vortex sheet is formed. The pressure across such a vortex sheet is continuous. Prescribing a separation point in inviscid flow theory and enforcing continuity of pressure across the shed vortex sheet is known as the Kutta condition.

The Kutta condition is imposed at the trailing edge, which determines the generation of vorticity. Assuming harmonic oscillations  $y_{\text{plate}}(t) = \frac{y_0 c}{2} e^{i\omega t}$ ,  $\phi'_{ac} = \widehat{\phi}(x, y) e^{i\omega t}$  with  $i^2 = -1$ , and  $v' = \widehat{v}(x, y) e^{i\omega t}$  and using equation (2.3) gives

$$\frac{\partial \widehat{\phi}(x, y)}{\partial y} = i\omega \widehat{v}(x, y) + U_\infty \frac{\partial \widehat{v}(x, y)}{\partial x}. \quad (2.6)$$

This equation can be solved for  $\widehat{v}(x, y)$  using the fact that  $v = 0$  for  $x = -\infty$  so that

$$\widehat{v}(x, y) = \frac{e^{-i\omega(x/U_\infty)}}{U_\infty} \int_{-\infty}^x \frac{\partial \widehat{\phi}(\xi, y)}{\partial y} e^{i\omega(\xi/U_\infty)} d\xi. \quad (2.7)$$

Equation (2.7) gives the relation between the vertical velocity amplitude of the fluid oscillation at a point  $(x, y)$  and the amplitude of the acceleration potential,  $\widehat{\phi}(x, y)$ . In order to find the acceleration potential satisfying all the boundary conditions, the plate in the physical plane, where  $z = x + jy$  with  $j^2 = -1$  and the origin at the center of the plate, is transformed to a circle with radius  $b = c/2$ , centered at the origin, in the  $\zeta$ -plane using the method of a conformal mapping, known as the Joukowski mapping. The mapping is given by

$$z = \frac{1}{2} \left( \zeta + \frac{b^2}{\zeta} \right), \quad (2.8)$$

where  $\zeta = \xi + j\eta$ . The boundary conditions on the plate should also be satisfied on the circle with radius  $b$ . Since on the circle  $|\frac{dz}{d\zeta}| = |\sin \theta|$ , the

acceleration of the plate is related to the acceleration of the circle by

$$a'_n \Big|_{\text{circle}} = a'_y \Big|_{\text{plate}} \sin \theta \quad , \quad (2.9)$$

where  $\theta$  is the angle with respect to the  $\xi$ -axis and  $a'_n$  is the acceleration normal to the circle in the  $\zeta$ -plane. In the physical  $z$ -plane the accelerations at infinity approach zero as  $z$  tends to infinity. This corresponds to the condition that the real part of the complex acceleration potential is a constant at infinity. Since infinity in the  $z$ -plane corresponds to infinity in the  $\zeta$ -plane it follows that

$$\lim_{|\zeta| \rightarrow \infty} \Re(w) = \phi'_{ac} |_{\infty} = \text{constant}. \quad (2.10)$$

Since  $\psi'_{ac}$  is related to  $\phi'_{ac}$  as

$$a'_x = \frac{\partial \phi'_{ac}}{\partial x} = \frac{\partial \psi'_{ac}}{\partial y}, \quad (2.11)$$

$$a'_y = \frac{\partial \phi'_{ac}}{\partial y} = -\frac{\partial \psi'_{ac}}{\partial x}, \quad (2.12)$$

this implies that  $\lim_{|\zeta| \rightarrow \infty} \psi'_{ac} = \text{constant}$ . As a result the complex potential  $w$  can be written as the principal part of a Laurent series (since the analytic part would diverge for  $|\zeta| \rightarrow \infty$ ), i.e.

$$w(\zeta) = C + \frac{A_1}{\zeta} + \frac{A_2}{\zeta^2} + \frac{A_3}{\zeta^3} + \dots \quad . \quad (2.13)$$

The constant  $C$  can be omitted because it has no influence on the accelerations, which are given by the gradient of the acceleration potential. The constants  $A_n$  should be chosen to satisfy the boundary conditions. One will find, however, that the boundary condition for the velocity cannot be satisfied. In order to satisfy this condition one must add a dipole to the complex acceleration potential. This dipole must be located at the leading edge with its direction perpendicular to the  $x$ -axis (the direction of the dipole is defined as the direction from source to sink), which gives

$$w(\zeta) = \frac{jA_0}{\zeta + b} + \frac{A_1}{\zeta} + \frac{A_2}{\zeta^2} + \frac{A_3}{\zeta^3} + \dots \quad . \quad (2.14)$$

Note that  $A_0$  is a real constant. The Kutta condition is satisfied if the series above converges at the trailing edge  $\zeta = b$ .

For the case of uniform vertical translation (also known as plunging motion) the oscillation of the plate with chord  $c$  can be described as

$$y_{\text{plate}}(t) = \frac{y_0 c}{2} e^{i\omega t} = \frac{y_0 c}{2} e^{i \frac{2U_\infty}{c} kt}, \quad (2.15)$$

where  $k = \frac{\omega c}{2U_\infty}$  is the reduced frequency and  $y_0$  is the non-dimensional amplitude of the oscillation. Note that  $i\omega t$  with  $i^2 = -1$  denotes a phase change in time whereas the variable  $j$ , introduced earlier, is used to separate the real and imaginary part of the complex acceleration potential or to separate the real and imaginary part of the complex variable  $\zeta$  corresponding to two directions in space (so  $ij \neq -1$ ). Using equation (2.15), the velocity and acceleration of the plate are given by

$$\frac{dy_{\text{plate}}}{dt} = iU_\infty k y_0 e^{i \frac{2U_\infty}{c} kt}, \quad (2.16)$$

$$\frac{d^2 y_{\text{plate}}}{dt^2} = -\frac{2}{c} U_\infty^2 k^2 y_0 e^{i \frac{2U_\infty}{c} kt}. \quad (2.17)$$

Using equation (2.9), the normal component of the acceleration on the circle in the  $\zeta$ -plane is given by

$$a'_n(|\zeta| = b) = \left. \frac{\partial \phi'_{ac}}{\partial r} \right|_{r=b} = -U_\infty^2 k^2 y_0 \frac{2}{c} e^{i \frac{2U_\infty}{c} kt} \sin \theta. \quad (2.18)$$

In polar coordinates, with radius  $r$  and angle  $\theta$ , the complex variable  $\zeta$  and the complex acceleration potential  $w$  can be written as

$$\zeta = r(\cos \theta + j \sin \theta), \quad (2.19)$$

$$w(r, \theta) = \phi_{ac}(r, \theta) + j\psi_{ac}(r, \theta), \quad (2.20)$$

respectively. Rewriting equation (2.14) in terms of the variables  $r$  and  $\theta$  gives

$$\begin{aligned} w(r, \theta) &= \frac{jA_0}{r(\cos \theta + j \sin \theta) + b} + \frac{A_1}{r(\cos \theta + j \sin \theta)} + \frac{A_2}{r^2(\cos \theta + j \sin \theta)^2} + \dots \\ &= A_0 \frac{rj \cos \theta + r \sin \theta + jb}{r^2 + 2rb \cos \theta + b^2} + A_1 \frac{\cos \theta - j \sin \theta}{r} + A_2 \frac{\cos 2\theta - j \sin 2\theta}{r^2} + \dots \end{aligned} \quad (2.21)$$

Recall that the acceleration of the circle is given by equation (2.18). This acceleration should be equal to  $\frac{\partial \phi'_{ac}}{\partial r}$  on the circle. From this it can be

seen that in order to satisfy the boundary condition for the acceleration (proportional to  $\sin \theta$ ) the complex acceleration should be of the form

$$w(\zeta) = \frac{jA}{\zeta + b} + \frac{jB}{\zeta}, \quad (2.22)$$

where  $A$  and  $B$  are real constants. The constant  $B$  is determined from the boundary condition for the acceleration

$$a'_n(r = b) = \left. \frac{\partial \phi'_{ac}}{\partial r} \right|_{r=b} = -\frac{4B \sin \theta}{c^2} e^{i \frac{2U_\infty}{c} kt} = -U_\infty^2 k^2 y_0 \frac{2}{c} e^{i \frac{2U_\infty}{c} kt} \sin \theta, \quad (2.23)$$

which gives

$$B = U_\infty^2 k^2 y_0 \frac{c}{2}. \quad (2.24)$$

The constant  $A$  is determined from the boundary condition, equation (2.4), for the vertical velocity, on the plate substituted in equation (2.7). Now the left hand side corresponds to the velocity of the plate and the right hand side is related to the velocity of the fluid. This boundary condition leads to an integral equation for the acceleration potential, which is only valid on the plate  $-b \leq x \leq b$ ,

$$iU_\infty k y_0 e^{i\omega t} = \frac{e^{-ikx/b}}{U_\infty} \int_{-\infty}^x \frac{\partial \hat{\phi}(\xi, 0)}{\partial y} e^{i\omega t} e^{ik\xi/b} d\xi, \quad -b \leq x \leq b, \quad (2.25)$$

which can be solved for the constant  $A$ , see Fung (1955), i.e.

$$A = -iU_\infty^2 k y_0 c \frac{K_1(ik)}{K_0(ik) + K_1(ik)} = -iU_\infty^2 k y_0 c C(k). \quad (2.26)$$

Here,  $K_0$  is a modified Bessel function of the second kind of order zero and  $K_1$  is a modified Bessel function of the second kind of order one and  $C(k) = \frac{K_1(ik)}{K_0(ik) + K_1(ik)}$ , is known as Theodorsen's function. Recall that the symbol  $i$  is used to denote a phase change in time, so that  $A$  is still a real variable with respect to  $j$ . The acceleration potential  $\phi$  and the stream function,  $\psi$ , can now be calculated by taking the real and imaginary part of equation (2.22), respectively. If we take  $\zeta = r e^{j\theta}$

$$\hat{\phi}(x, y) = \Re(w(r, \theta)) = \frac{Ar \sin \theta}{r^2 + 2rb \cos \theta + b^2} - \frac{B \sin \theta}{r}. \quad (2.27)$$



On the surface of the plate,  $r = b$ , this becomes

$$\hat{\phi}(\theta) = -2iU_\infty^2 ky_0 C(k) \tan \frac{\theta}{2} - U_\infty^2 k^2 y_0 \sin \theta. \quad (2.28)$$

Now both the acceleration potential  $\phi_{ac}$  and the stream function,  $\psi_{ac}$ , are known and the problem is solved.

The pressure is related to the acceleration potential by the Bernoulli equation  $p = -\rho\phi$ . The function of time is omitted here, because it is zero in this case. Application of the Bernoulli equation yields the following equation for the pressure difference over the plate

$$\Delta p = -2\rho U_\infty^2 y_0 k i C(k) \tan \frac{\theta}{2} + 2\rho U_\infty^2 y_0 k^2 \sin \theta, \quad (2.29)$$

with  $\Delta p$  positive when the pressure on the upper side of the plate is lower than the pressure on the lower side. The lift force can be obtained by integration of this pressure difference along the plate, which gives

$$l = \frac{1}{2} \pi \rho U_\infty^2 y_0 k^2 c \left[ 1 - \frac{2i}{k} \frac{K_1(ik)}{K_1(ik) + K_0(ik)} \right] e^{i\omega t}. \quad (2.30)$$

Because it is difficult to measure unsteady lift forces experimentally, we choose to measure local unsteady pressures. Since the lift force is obtained by the integration of the surface pressure over the airfoil surface, the local pressure difference  $\Delta p$  over the plate is closely related to the lift force. The pressure difference given by equation (2.29) can be made non-dimensional by the freestream density  $\rho$ , the freestream velocity  $U_\infty$  and the plunging velocity amplitude  $v_{\text{plate}} = iU_\infty ky_0$  (see also equation (2.16)):

$$\Delta C_{pu} = \frac{\Delta p}{\frac{1}{2} \rho U_\infty v_{\text{plate}}} = -4 \left[ C(k) \tan \frac{\theta}{2} + ik \sin \theta \right]. \quad (2.31)$$

The subscript  $u$  emphasises that this is an unsteady non-dimensional difference in pressure coefficient. Here we have considered the case where the plate is moving. However, if the plate is fixed and the flow is oscillating, an upward motion of the plate corresponds to a downward motion of the flow, thus for the case of an oscillating flow  $v_{\text{plate}}$  should be replaced with  $-\tilde{v}'$  in equation (2.31), where  $\tilde{v}'$  is the amplitude of the oscillating flow.

The lift force given in equation (2.30) can also be expressed as a non-dimensional lift force by dividing equation (2.30) by the quasi-steady lift force

$$l_0 = -\pi \rho U_\infty^2 c i k y_0 e^{i\omega t}, \quad (2.32)$$

(this is obtained by taking the limit  $k \rightarrow 0$  in equation (2.30)). The minus sign reflects the fact that an upward motion in the  $y$ -direction of the airfoil gives a force in the negative  $y$ -direction and the symbol  $i$  indicates that the velocity is 90 degrees out of phase with the displacement of the plate. The non-dimensional lift force is then given by

$$\frac{l}{l_0} = \frac{K_1(ik)}{K_1(ik) + K_0(ik)} + \frac{ik}{2} = 1 - \frac{K_0(ik)}{K_1(ik) + K_0(ik)} + \frac{ik}{2} \quad (2.33)$$

According to Sears & Von Kármán (1938), three contributions to the lift force can be recognised in equation (2.33): the first term in equation (2.33) corresponds to the quasi-steady lift, the second term represents the lift generated by the wake and the last term is related to the apparent mass of the plate. A derivation of the apparent mass of a flat plate is provided in Appendix B. The quasi-steady lift force is always in phase with the velocity whereas the lift force associated with the apparent mass always leads the velocity of the plate by 90 degrees. The lift force associated with the wake tends to diminish the total lift force. The non-dimensional lift

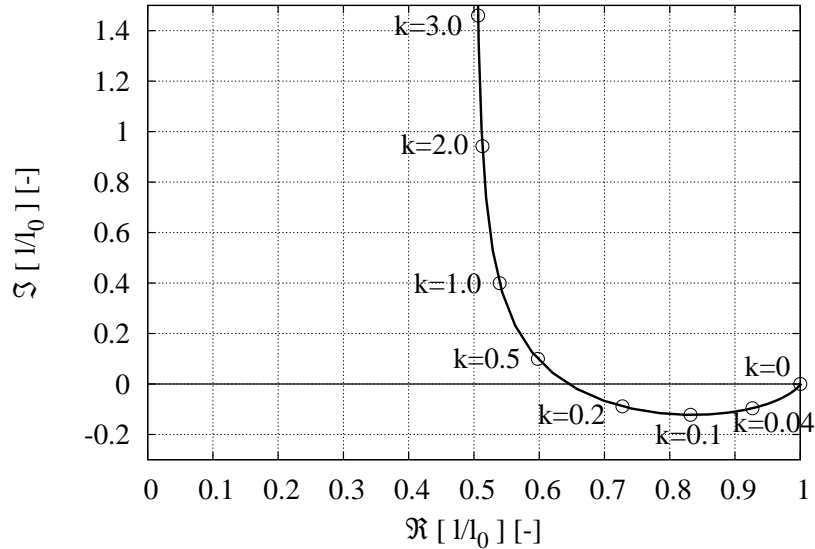


**Figure 2.2** – Non-dimensional lift force for different values of the reduced frequency  $k$ .

force can be plotted in the complex plane, where the amplitude of a point in the complex plane represents the amplitude of the oscillation and the phase of the complex point represents the phase shift in time with respect

to the velocity of the plate. Such a plot is shown in figure 2.2 for reduced frequencies in the range  $0 < k < 3$ .

The vertical asymptote in figure 2.2 is due to the apparent mass term which grows linearly with the reduced frequency because the accelerations become larger for higher reduced frequencies, for high  $k$  values  $C(k) \rightarrow 0.5$ . In the limit of  $k \rightarrow 0$  the non-dimensional lift force obviously approaches 1, i.e. the lift force approaches the quasi-steady lift force  $l_0$ .

When we divide equation (2.31) by the quasi-steady non-dimensional pressure difference over a flat plate we obtain

$$\Delta C_{pu} = 1 - \frac{K_0(ik)}{K_0(ik) + K_1(ik)} + ik(1 + \cos \theta). \quad (2.34)$$

The imaginary part of equation (2.34) is plotted as a function of the real part for different values of  $k$ , in figure 2.3. Here  $\theta = 2.395$ , which corresponds to the location on the plate at 13.3% of the chord length from the leading edge. This location corresponds to one of the locations where we experimentally measure the pressure difference. As expected figures 2.2 and

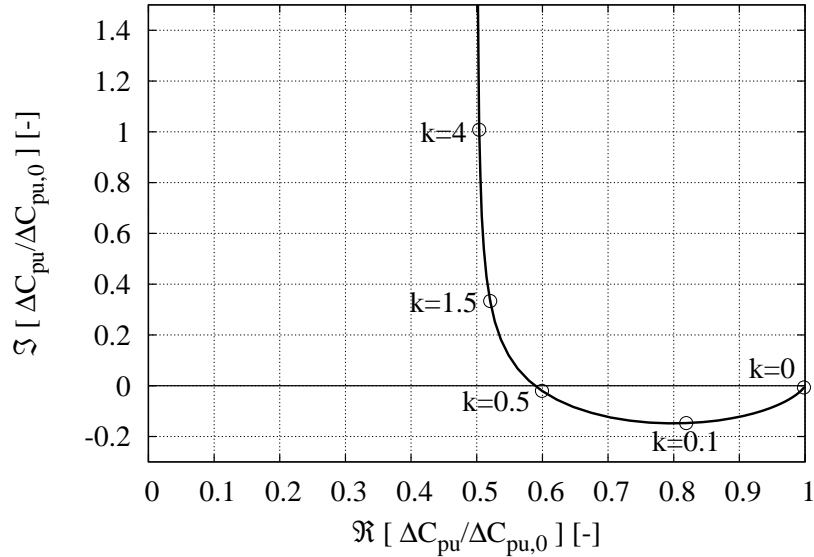


**Figure 2.3** – Non-dimensional pressure difference at 13.3% of the chord length from the leading edge, for different values of the reduced frequency  $k$ .

2.3 are similar, illustrating the close relationship between the local pressure difference and the lift force, for a flat plate. In the rest of this thesis we will mainly present results as local differences in the pressure coefficient as

given by equation (2.31).

The theoretical solution derived in this section is a simplified model of the reality. The flow was assumed two-dimensional, inviscid and incompressible. The effect of viscosity at the sharp trailing edge was taken into account by imposing a Kutta condition (removing the singularity of the potential flow at this point). Furthermore the airfoil was modelled as a flat plate without thickness. Even though these assumptions may seem severe simplifications of reality, the theoretical model has proven to correctly predict the unsteady behaviour of attached flow over thin airfoils with finite thickness and is well known in the literature on unsteady aerodynamics of airfoils. The model also provides significant physical insight into the flow over oscillating airfoils.

### 2.3 Effect of finite airfoil thickness

In the preceding section the linearised potential theory for a flat plate has been introduced. In reality, however, airfoils have a finite thickness. In our experiments we will use a NACA0018 airfoil with a chord length of 165 mm. This is a symmetric airfoil with 18% thickness, which means it is a relatively thick airfoil. Because of its structural stiffness (due to its thickness) this airfoil is mainly used in vertical axis wind turbines. More information about the NACA0018 airfoil can be found in appendix A. In this section we will correct Theodorsen's theory for the effect of finite airfoil thickness.

The local pressure difference over the plate, given by equation (2.29), can be split up in three different contributions in a similar manner as was done for the lift force given by equation (2.30). Using  $\tilde{v} = iU_\infty k y_0$  and  $k = \frac{\omega c}{2U_\infty}$ , the pressure difference given by equation (2.29) can be written as

$$\Delta p = -2\tilde{v}\rho U_\infty \tan \frac{\theta}{2} + 2\tilde{v}\rho U_\infty \frac{K_0}{K_0 + K_1} \tan \frac{\theta}{2} - \tilde{v}\rho i \omega c \sin \theta, \quad (2.35)$$

or in non-dimensional form

$$\Delta C_{pu} = -4 \tan \frac{\theta}{2} + 4 \frac{K_0}{K_0 + K_1} \tan \frac{\theta}{2} - 4i \frac{\omega c}{2U_\infty} \sin \theta. \quad (2.36)$$

Here, the first term is the quasi-steady linearised pressure difference over a flat plate, the second term is due to the wake and the third term is the added mass contribution.

Now that we have recognised three different contributions to  $\Delta C_{pu}$ , we can estimate the deviations that may be expected for an airfoil with finite thickness by correcting the quasi-steady lift and added mass contributions and assuming that the contribution of the wake is independent of the airfoil thickness.

It is possible to obtain a numerical solution for the exact NACA0018 airfoil by the use of a panel method. However, here we will approximate the NACA0018 airfoil by a Von Kármán–Trefftz airfoil because this yields analytical results. The details of the derivation are given in appendix C.

The quasi-steady non-dimensional pressure difference  $\Delta C_{pu}$  over a Von Kármán–Trefftz airfoil ( $\varepsilon = 0.12$ ,  $n = 1.93$ , see appendix C for the definition of these parameters) is plotted in figure 2.4 as a function of the chord position  $x/c$  along the airfoil, by the solid line. The distribution for a flat plate is shown by a dashed line. From figure 2.4 it can be seen that the

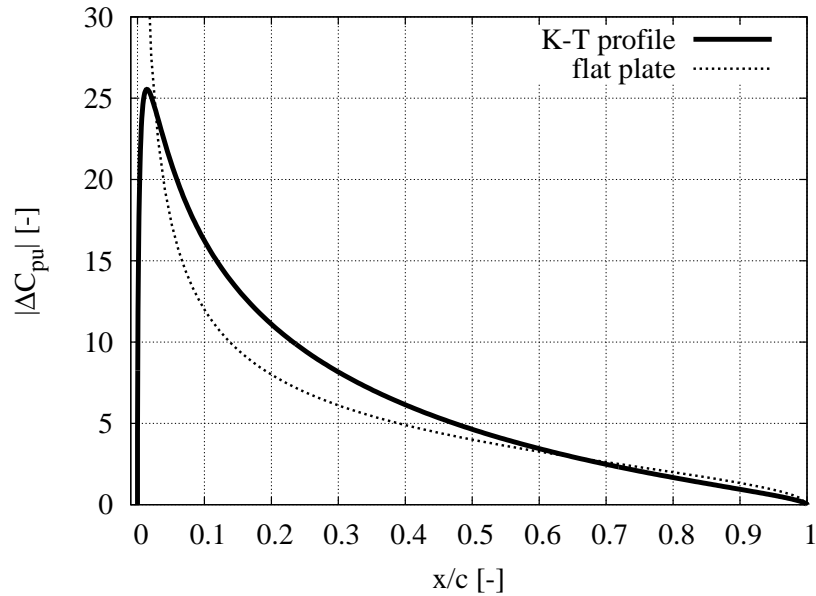


**Figure 2.4** – Chordwise distribution of the non-dimensional pressure difference between the upper and lower surface for a Von Kármán–Trefftz airfoil (solid line) and a flat plate (dashed line).

differences between an airfoil with thickness and a flat plate depends on the chordwise position. Clearly the singularity present in the pressure at the leading edge of the plate is unphysical and comparison of results near the leading edge will lead to large deviations. From the figure we conclude

that at 13.3% of the chord length, the quasi-steady value of  $\Delta C_{pu}$  is 38% higher than that of a corresponding flat plate.

We can also use the Von Kármán–Trefftz airfoil to calculate the added mass of the airfoil and the local pressure difference due to the added mass. For the K-T airfoil ( $\varepsilon = 0.12$ ,  $n = 1.93$ ) this yields that the pressure difference at 13.3% of the chord length, due to the added mass effect, for an airfoil with thickness is 6% lower than that of a flat plate with the same chord length.

Based on the estimates of  $\Delta C_{pu}$  we correct Theodorsen’s theory for a flat plate to take the effects of finite thickness into account. The results obtained with these corrections are plotted in figures 2.5(a) and 2.5(b). From figure 2.5(a) it can be seen that due to the increased quasi-steady

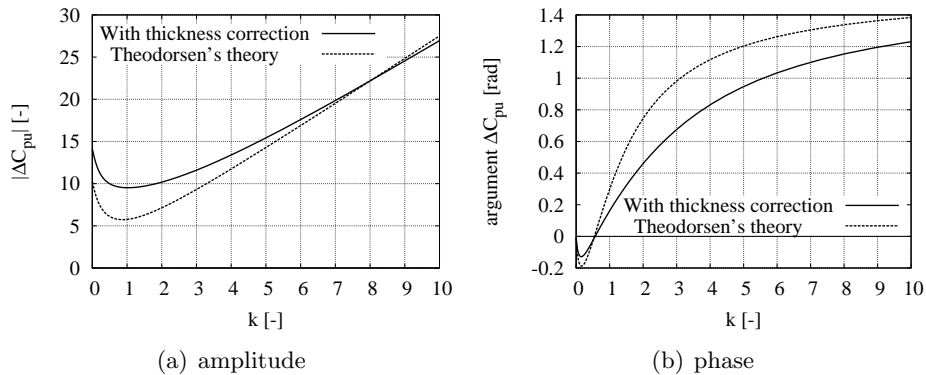


**Figure 2.5** – Non-dimensional pressure difference over flat plate at 13.3% of the chord length from the leading edge as a function of the reduced frequency  $k$ . Solid line shows Theodorsen’s theory for a flat plate, the dashed line shows result of Theodorsen’s theory with corrected added mass and quasi-steady contributions.

contribution the curve is shifted upwards for low  $k$  values. However, at higher  $k$  values the corrected curve crosses the uncorrected curve due to a decrease in added mass of the airfoil with finite thickness. Figure 2.5(b) shows that for  $k > 0.5$  the effect of finite thickness is to lower the phase and the curve approaches the asymptote at a lower rate.

We should emphasise here that the assumptions made in the derivation of thin airfoil theory may fail for thick airfoils, like the one we consider in our experiments (and the Kármán–Trefftz airfoil used in this section). Also we have assumed that the wake behind an oscillating airfoil with finite thickness is the same as that of an oscillating flat plate. The corrections obtained in this section must therefore be seen as an estimate rather than

an exact result.

## 2.4 Apparent mass

In section 2.2 the problem of an oscillating flat plate in a uniform flow was solved by a linear theory with application of the Kutta condition. It is however, also useful for a physical understanding to consider the solution of an unsteady potential flow around a flat plate when the Kutta condition is not applied. In this case there is no circulation around the plate and there is no wake. The only force acting on the plate is due to the apparent mass of the plate. We again make use of the Joukowski transformation to solve this problem. The easiest way to solve this problem is to consider a flat plate in an oscillating flow. Since the plate has no thickness there is no need to take the contribution of the time-dependent uniform pressure gradient driving the flow (section 2.1), into account.

Since there is no wake the velocity potential is easily found. The complex velocity potential in the transformed  $\zeta$ -plane ( $\zeta = \xi + j\eta$ ) consists of a uniform velocity in the positive  $\xi$ -direction  $U_\infty$  and an oscillating velocity in the  $\eta$ -direction with velocity amplitude  $\tilde{v}$  and frequency  $\omega$  given by a superposition of two dipoles:

$$\Phi = U_\infty \left( \zeta + \frac{R^2}{\zeta} \right) - \tilde{v} \cos \omega t \left( j\zeta - \frac{jR^2}{\zeta} \right). \quad (2.37)$$

The Joukowski mapping used here is given by

$$z = \zeta + \frac{R^2}{\zeta}, \quad \frac{dz}{d\zeta} = \frac{\zeta^2}{\zeta^2 - R^2}. \quad (2.38)$$

The factor of  $\frac{1}{2}$ , which was present in the Joukowski mapping in section 2.2, is omitted here for convenience. From the complex velocity potential  $\Phi = \phi + j\psi$  we can compute the velocity, the velocity potential and the time derivative of the velocity potential. Note that here  $\phi$  is the velocity potential and  $\psi$  is the stream function, these should not be confused with the acceleration potential and acceleration stream function used in section 2.2. These quantities are needed to calculate the pressure from the Bernoulli equation for unsteady potential flow

$$\rho \frac{\partial \phi}{\partial t} + \frac{1}{2} \rho |\vec{u}|^2 + p = C(t), \quad (2.39)$$

where  $C(t)$  is a function of time only. The details of the derivation of the pressure difference are given in appendix D.

The pressure difference over the plate has two contributions. The first is a contribution of the added mass effect, the second is the pressure difference due to the instantaneous potential flow around the plate. This second pressure difference yields zero force when it is integrated over the chord length (d'Alembert paradox). The non-dimensional pressure difference can be written in complex form as

$$\frac{2\Delta p}{\rho U_\infty \widehat{v}} = 4i \frac{\omega b}{U_\infty} \sin \theta - \frac{4}{\tan \theta} \quad (2.40)$$

The pressure difference can be integrated to find the force on the plate:

$$F_y = \int_0^\pi -\Delta p \sin \theta R d\theta = \pi R^2 \rho \widehat{u} \omega \sin \omega t. \quad (2.41)$$

The non-dimensional pressure differences are plotted in figure 2.6(a) and figure 2.6(b). It is clear that above  $k = 2.5$  the influence on the amplitude of

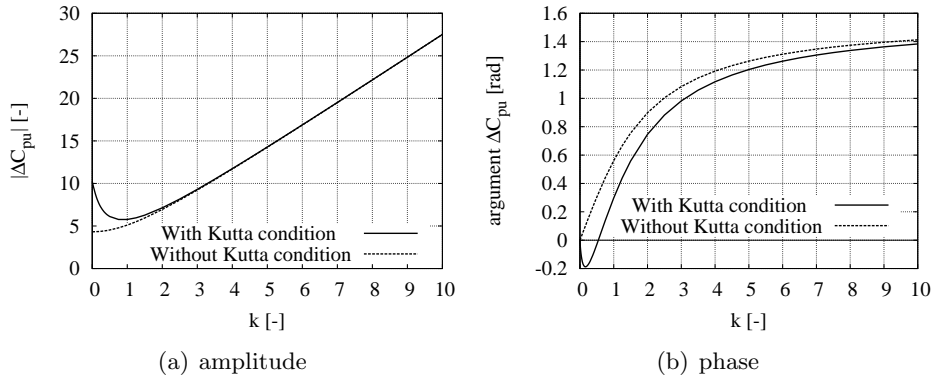


**Figure 2.6** – Non-dimensional pressure difference over flat plate at 13.3% of the chord length from the leading edge as a function of the reduced frequency  $k$ . Solid lines correspond to the full linearised potential theory with Kutta condition; the dashed lines correspond to the potential theory without Kutta condition.

the Kutta condition is negligible. The amplitude is fully determined by the apparent mass effect and the pressure difference due to the instantaneous potential flow around the plate. The phase shows more information and is consistently larger than the phase obtained in section 2.2 in which case a Kutta condition is applied. The shape of the phase and amplitude only differ below a reduced frequency of 2.5.



## 2.5 Wall interference effects

The results obtained in section 2.2 assume that the flat plate is in the free field. In practice, however, airfoils are usually tested within the closed test section of a wind tunnel. The presence of wind tunnel walls has two main effects. Due to the “blockage” effect (local constriction) of the test section the flow around the airfoil reaches higher velocities than would occur in free field conditions for the same oncoming stream velocity. A second effect of the walls occurs when there is circulation around the airfoil. The presence of the walls can then be modelled by an infinite row of mirror vortices. In the case of unsteady flow the airfoil sheds infinite rows of vortices rather than single vortices. In the case of a steady flow around an airfoil with walls above and below the airfoil, the flow is equivalent to the flow through a cascade of airfoils. The effect of walls can be taken into account (by mirror vortices) in unsteady linearised potential theory, see Timman (1951); Jones (1957, 1958).

Figures 2.7(a) and 2.7(b) display the effect of wind tunnel walls on  $\Delta C_{pu}$  compared to the linearised potential theory in free field conditions. The results shown are obtained from Jones (1958) for a wind tunnel width  $H$  to plate chord length  $c$  ratio of  $H/c = 3.03$ , which corresponds to the ratio in our wind tunnel experiments.

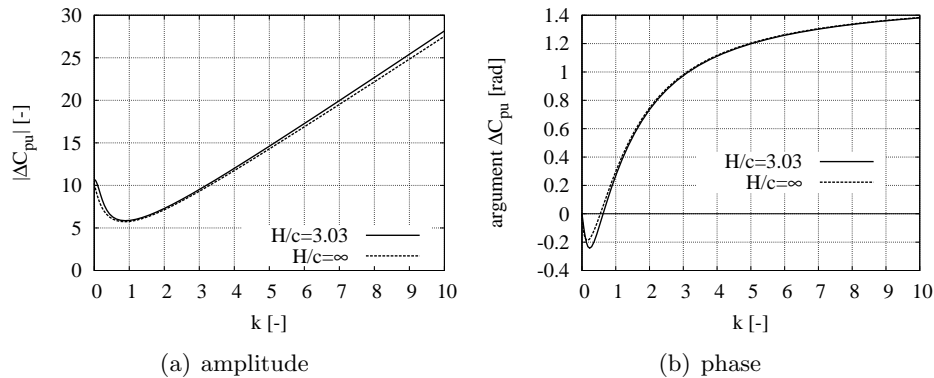


**Figure 2.7** – Non-dimensional pressure difference over flat plate at 13.3% of the chord length from the leading edge as a function of the reduced frequency  $k$ . The solid line indicates linearised potential theory with wall interference taken into account for  $H/c = 3.03$ , the dashed line corresponds to the result of Theodorsen’s theory in free field conditions ( $H/c = \infty$ ).

From the figures we conclude that, based on the linearised potential theory, no significant wall interference effects are to be expected for  $k > 2$ . The effect of the wind tunnel walls, for  $H/c = 3.03$ , is to slightly increase the amplitude compared to  $H/c = \infty$ . The deviations of the phase are only significant for reduced frequencies below 1.0.

## 2.6 Numerical methods

In this thesis several numerical methods have been used. In this section a brief description of the numerical methods will be given, along with a motivation for the use of the specific method.

Note that as the complexity of the employed method increases also the interpretation of the results becomes more involved. The best solution method is therefore one which is simple, but still able to capture the essential flow physics involved in a particular application.

Most of the numerical method used in this thesis yield solutions in the time domain. In order to translate these signals in the time domain to an amplitude and corresponding phase in the frequency domain a lock-in method is applied. This lock-in method is described in appendix E.

### 2.6.1 Discrete vortex method

The discrete vortex method is a method to numerically solve the two-dimensional vorticity equation. The vorticity equation can be derived from the Navier–Stokes equations, its derivation can be found in several text books, for example Saffman (1992).

The idea is to model the continuous vorticity field by a finite number of point vortices. In a point vortex the vorticity is concentrated in a point and therefore the velocity at this point is singular. If point vortices come too close to each other the singular velocities fields can cause the vortices to displace over a large distance within a small amount of time, which is unphysical, and leads to chaotic behaviour. The usual solution to this problem is to describe the vorticity field by vortices with the vorticity distributed over a finite core (a desingularised core also known as a blob) which is the basis of the so-called vortex blob method.

The vorticity field is advanced in time by computing the velocity at the location of all the vortices omitting the (singular) contribution of that specific vortex itself. The discrete-vortex method avoids the use of a computational mesh, which is an advantage of these methods. The calculation

of the velocities of all vortices at all vortices has a computational complexity of  $O(N^2)$ , where  $N$  is the number of vortices. This means that for large numbers of vortices the computation becomes very time-consuming. This computational complexity can be reduced by approximation techniques, such as the Fast Multipole Method, resulting in a computation complexity of  $O(N \ln N)$ . The benefit of the discrete vortex methods is the relatively low computational cost (for not too many vortices) and simple implementation.

In discrete vortex methods, a boundary is usually represented by a singularity distribution (panels), such as a dipole/source or vortex distribution. In the inviscid flow case the discrete vortices are released at prescribed points on the body, where a Kutta condition is applied to determine the strength of the discrete vortex. The vortices are convected with the local fluid velocity. It was found that such a numerical method can fail to satisfy Kelvin's circulation theorem as time evolves. A solution to this problem is proposed by Lewis (1991).

It is also possible to compute viscous flows with the discrete vortex method, this implies the use of a boundary layer model in order to couple the vorticity distribution in the boundary layer to discrete vortices outside the boundary layer. In most numerical methods the diffusion of vorticity is modelled by core spreading or by redistribution of vorticity. Core spreading means that the core size of the discrete blobs grows over time, such that the vorticity is spread over a larger surface area. Core spreading can make the vortex method more stable, but in the limit of infinitely many vortices the core spreading model does not converge to the solution of the Navier–Stokes equations, see Greengard (1985). The vorticity redistribution method does converge to the solution of the Navier–Stokes equations. In this method the vorticity is redistributed amongst the individual vortices. For details about the vortex redistribution method the reader is referred to Subramaniam (1996).

In this thesis a commercial vortex blob method has been used: Virtual Oscillation - 2D (2006). This method combines a potential flow panel method with point vortices with a finite core (also known as blobs) and vorticity diffusion is modelled by core spreading. This code has the capability to physically move an object with respect to the flow. We only used the code to compute inviscid flows, with prescribed separation points. The code always employs core spreading of the vortices. This means that boundary layers are ignored while diffusion of the vortices is represented.

Results obtained for a NACA0018 airfoil with the discrete vortex code Virtual Oscillation - 2D (2006) are presented in figures 2.8(a) and 2.8(b). Here the NACA0018 airfoil is discretised by 249 panels. The panel distribution has been refined near the leading and trailing edges. The oscillating velocity plunging amplitude is  $\tilde{v}/U_\infty = 5 \cdot 10^{-2}$ . This code allows the physical displacement of the airfoil with respect to the flow, so in this case there is no time-dependent uniform pressure gradient due to an oscillating flow. In figures 2.8(a) and 2.8(b) the differences in the results are close to effects

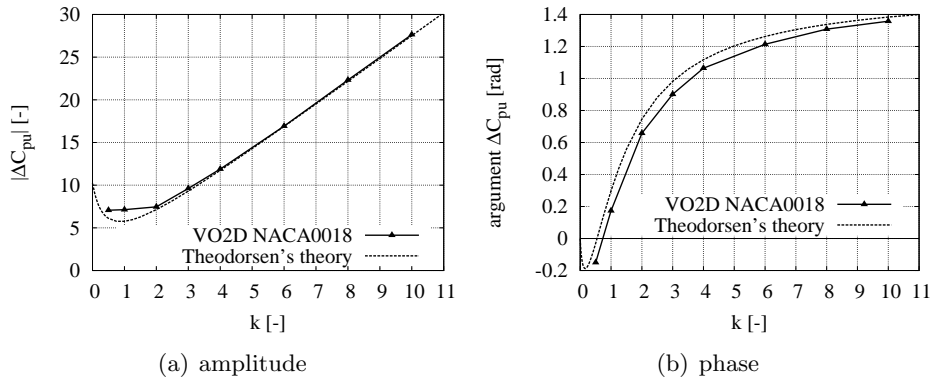


**Figure 2.8** – Non-dimensional pressure difference over a NACA0018 airfoil at 13.3% of the chord length from the leading edge as a function of the reduced frequency  $k$ . Solid line with triangular markers shows numerical results obtained with discrete vortex method for a plunging NACA0018 airfoil  $\tilde{v}/U_\infty = 5 \cdot 10^{-2}$ . The dashed lines show the results of Theodorsen's theory for a flat plate.

of the finite thickness of the airfoil. However, the effects are not so important as we expected based on the results from section 2.3. We should keep in mind, however, that in the analytical method the wake behind the plate is described by a continuous vortex sheet, whereas in the discrete vortex method the wake is described by discrete vortices. We conclude from the results of the calculations that the theory proposed in section 2.3 exaggerates the effect of finite-airfoil thickness.

### 2.6.2 Solutions of Euler equations

The Euler code which will be used in this thesis is an “Euler code for Internal Aeroacoustics” (EIA) developed by Hulshoff (2000). This code solves the Euler equations in conservation form numerically. The benefit of solving the equations in conservation form is that flow discontinuities such as

shocks, contact surfaces and vortex sheets can be accommodated.

The numerical method is based on a second-order accurate finite-volume spatial discretisation in the interior and an one sided finite-difference discretisation of the compatibility relations on the boundary. The Euler equations are integrated in time using either a multistage Runge–Kutta explicit time stepping scheme or an implicit pseudo-time integration scheme. For the unsteady flow cases we will employ the implicit pseudo-time integration. Numerical dissipation in the code ensures that the Kutta condition is fulfilled at sharp edges.

Use of the Euler equations has several benefits over using an incompressible potential flow method, such as the discrete vortex method described in the previous section. Since compressibility is included in EIA, Mach and Helmholtz number effects and wave propagation of acoustic waves are captured by the method. This means that we can compute the acoustic field around the airfoil. However, specifying the correct acoustic boundary conditions may be difficult in practice.

Because the effects of viscosity are neglected in the Euler equations, boundary layers and the resulting separation from a smooth surface cannot be predicted. However, in order to ensure a stable solution procedure for the solution of the Euler equations EIA employs numerical dissipation, which mimics some of the effects of physical viscosity, such as flow separation from a sharp corner (corresponding to the Kutta condition) and the diffusion of vorticity. This numerical dissipation decreases with grid refinement.

EIA uses a second-order accurate finite volume discretisation in the interior of the domain and a second-order accurate finite difference discretisation of the compatibility relations along the boundary of the domain. The equations are integrated in time with an explicit Runge–Kutta time stepping scheme or an implicit pseudo-time integration method.

In our wind tunnel setup, which will be described in detail in Chapter 3, the flow is oscillating rather than the airfoil. This movement of the flow is driven by an acoustic field which is generated by loudspeakers. In order to model this experimental method we will need a computational method that is able to model the propagation of acoustic waves accurately. Therefore we will use a numerical model based on the Euler equations. In this model the solution is dependent on two non-dimensional numbers, the Mach number  $M = \frac{U_\infty}{c_0}$  and the reduced frequency  $k = \frac{\omega b}{U_\infty}$ , with  $c_0$  the free stream speed of sound and  $b$  the semi-chord of the airfoil. Another non-dimensional number in compressible flows is the Helmholtz number  $He = \frac{2\pi b}{\lambda}$ , with  $\lambda$

the acoustic wave length. Note that the product of the Mach number and reduced frequency is in this case equal to the Helmholtz number  $He = Mk$ .

In our experiments  $M < 0.2$  and therefore we do not expect significant compressibility effects due to the Mach number. Because of our specific experimental procedure  $He$  is constant and has a value of 0.5. The Helmholtz number is the ratio of the size of an object over the acoustic wave length. When  $He^2 \ll 1$  the acoustic field around the airfoil is called “compact” and can be locally approximated as an incompressible potential flow. The Helmholtz number also indicates how efficiently an object will radiate acoustic waves in free field conditions, where  $He \ll 1$  indicates very inefficient radiation (this is the reason why small speakers produce very poor low-frequency sound).

Figures 2.9(a) and 2.9(b) show the values of  $\Delta C_{pu}$  as a function of  $k$  for the NACA0018 airfoil plunging in free field conditions. The computations have been performed for a constant value of  $He$ . The computational domain extends to about 50 chord lengths from the airfoil. The mesh is a structured C-grid around the airfoil with 128 cells on the airfoil, 64 cells in the wake and 32 cells in the direction normal to the airfoil. The mesh has been refined near the airfoil. The plunging velocity of the airfoil is implemented as prescribed velocity fluxes at the airfoil surface (grid velocities). In this case there is no oscillating flow, so there is no need to take the effect of the time dependent uniform pressure gradient into account. The reader should keep in mind that for  $He$  to be constant, a low reduced frequency value means a high Mach number and a high reduced frequency implies a low Mach number. The figures 2.9(a) and 2.9(b) clearly show a dependency of  $\Delta C_{pu}$  at  $x/c = 0.133$  on the Helmholtz number. The effect of a finite Helmholtz number is to increase the amplitude and to lower the phase, compared to Theodorsen’s theory. The influence of the Helmholtz number scales with  $He^2$ . Theodorsen’s theory is approached as one takes the limit  $He \rightarrow 0$ . Physically the results can qualitatively be interpreted as follows. If one plunges the airfoil so quickly that the fluid has no time to escape by flowing around the airfoil, the fluid will be compressed leading to an increase in the amplitude of the pressure.

In order to confirm that the results are grid independent two calculations are performed with a grid of twice the resolution as used to obtain the results indicated in figures 2.9(a) 2.9(b). The high resolution calculations are performed for  $He = 0.5$  and for  $k = 1$  and  $k = 10$ . In the lock-in procedure 18 periods were considered. The results obtained with the high

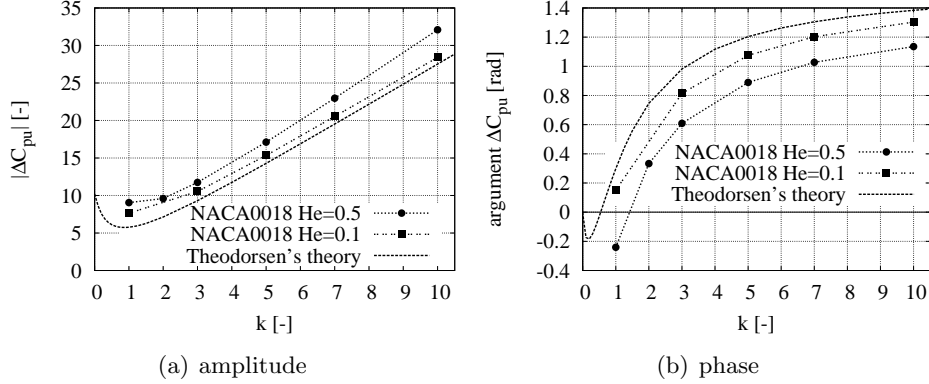


**Figure 2.9** – Non-dimensional pressure difference at 13.3% of the chord length from the leading edge as a function of the reduced frequency  $k$ . Solid line with circular markers corresponds to numerical results of the Euler equations obtained for  $He = 0.5$  for a plunging NACA0018 airfoil,  $\tilde{v}/U_\infty = 1 \cdot 10^{-2}$ . The dashed line with square markers represents the Euler method results for  $He = 0.1$  and  $\tilde{v}/U_\infty = 1 \cdot 10^{-2}$ . The dotted line corresponds to Theodorsen's theory,  $He = 0$ .

resolution grid agree within 1.8% to the lower resolution results.

For a flat plate oscillating in a compressible flow analytical solutions are available from Balakrishnan (1999); Lin & Iliff (2000). Figure 2.10 shows the same plot as figure 2.2, but here the results obtained from Lin & Iliff (2000) are plotted and compared to Theodorsen's theory ( $He = 0$ ). The symbols indicate the values of the reduced frequency  $k$ . From bottom to top these values are  $k = 1, 3, 6, 9$ . From figure 2.10 we observe the expected dependency on  $He^2$ . It is also no surprise that the Helmholtz number has qualitatively the same effect on the pressure difference  $\Delta C_{pu}$  as on the lift. This effect is to increase the amplitude and to lower the phase.

### 2.6.3 Navier–Stokes solutions

It will be demonstrated in Chapter 4 that for the computation of the flow around an airfoil with a cavity only a method which resolves the boundary layer can yield physical relevant results. Therefore we will employ a numerical method based on a discretisation of the vorticity transport equation in 2D. This method requires the highest computational effort of all the applied numerical methods because it resolves the boundary layer near the surface of the airfoil. In this method the 2D Navier–Stokes (2D NS) equations are solved without any turbulence model.

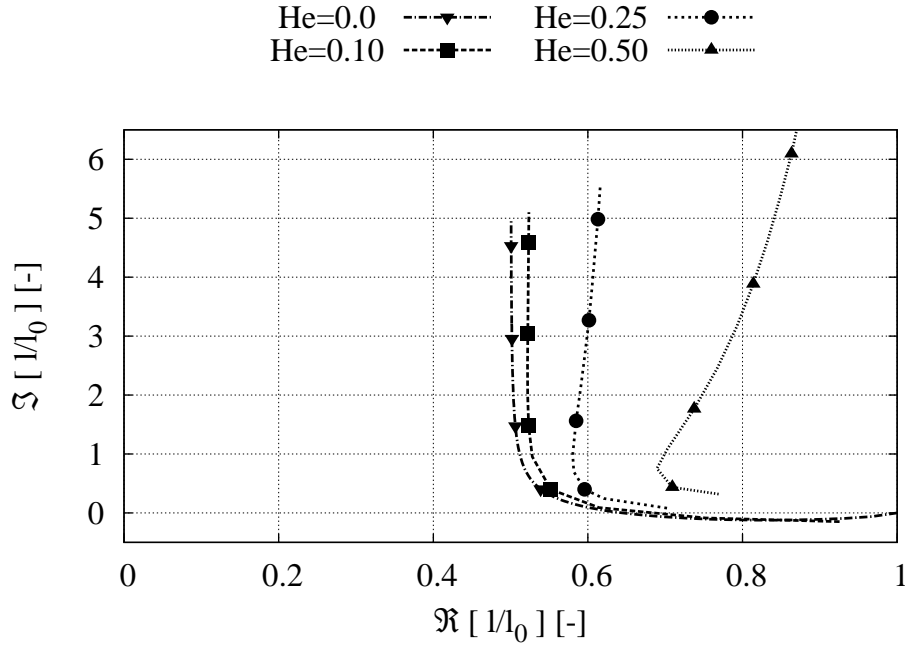


**Figure 2.10** – Flat plate in compressible flow, analytical results of the non-dimensional lift force for different values of the reduced frequency  $k$  and different values of the Helmholtz number  $He$ . Note that the  $x$  and  $y$ -axis have different scales in this figure.

The numerical method we will use in this thesis is obtained from Prof. T. Colonius from The California Institute of Technology. The numerical method is based on the Immersed Boundary Method (IBM), in which the surface of the airfoil is represented by points at which the no-slip boundary condition is enforced by an externally applied forcing term in the vorticity transport equation for incompressible flow. The forcing is not physical and will cause an inaccurate solution close to the surface where the no-slip boundary condition is enforced. At the outer boundary of the computational domain the boundary condition is free-slip. For more information about the numerical method the reader is referred to Taira & Colonius (2007); Colonius & Taira (2008).

The velocity field is computed from the streamfunction  $s$  (defined as  $\vec{u} = (\frac{\partial s}{\partial y}, -\frac{\partial s}{\partial x})^T$ ), which in turn is computed by solving the Poisson equation  $\nabla^2 s = -\omega$ . The Poisson equation is solved by application of the technique of Fast Fourier Transform (FFT).

The advantage of using 2D NS is that it resolves the effects of vis-



cosity, which is important in the case of an airfoil with cavity. The main disadvantage of 2D NS is the high computational cost. This means that we can only compute low Reynolds number flows. Nevertheless, these low Reynolds number flow computations can provide us with useful insight into the flow physics involved. Also we should note that this method solves the 2D incompressible Navier–Stokes equations. This means that compressibility of the flow, such as the effects of finite Mach and Helmholtz number are not represented and that the acoustic field around the airfoil cannot be simulated. Also turbulence cannot be computed since turbulence is an essentially three-dimensional phenomenon. In a real three-dimensional flow turbulence will cause a dramatic increase in the dissipation, due to the energy cascade from large to small vortical scale. In contrast, enforced two-dimensionality will cause small scale structures to merge into larger structures (self-organisation of the flow) by the mechanism of the inverse energy cascade, see McWilliams (1984).

Figures 2.11(a) and 2.11(b) show the values of  $\Delta C_{pu}$  obtained with the 2D NS code at Reynolds numbers based on the chord length,  $Re_c = \frac{U_\infty c}{\nu} = 2.01 \cdot 10^4$ , where  $\nu$  is the dynamic viscosity of the fluid. Figures 2.11(a) and

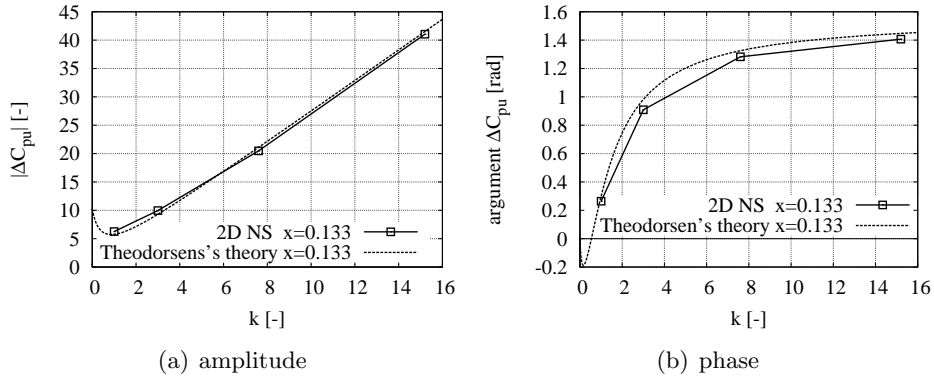


**Figure 2.11** – Non-dimensional pressure difference over a flat plate at 13.3% of the chord length from the leading edge as a function of the reduced frequency  $k$ . The solid line with square markers indicates 2D NS results for a plunging NACA0018 airfoil  $\tilde{v}/U_\infty = 5 \cdot 10^{-2}$ ,  $Re_c = 2.01 \cdot 10^4$ . The dotted line corresponds to Theodorsen's theory.

2.11(b) are very similar to figures 2.8(a) and 2.8(b). However, the flow fields are different. The discrete vortex method is an inviscid flow method such that the flow over the airfoil only separates at the prescribed separation points, whereas the 2D NS code is a method that resolves the boundary

layer. In the 2D NS results for the NACA0018 airfoil, which is a relatively thick airfoil, we observe a separation of the laminar boundary layer around 50% of the chord downstream of the leading edge.

At higher  $Re_c$  values we expect the boundary layer to become turbulent. In a turbulent boundary layer high momentum fluid is transported from the main flow to the wall by eddies, whereas in a laminar boundary layer this transport is driven by diffusion. The transport of momentum by eddies is much more efficient than transport by diffusion. For this reason the turbulent boundary layer can engage a larger adverse pressure gradient than a laminar boundary layer. We expect the separation point to move downstream when the boundary layer becomes turbulent.



## Chapter 3

# Experimental method\*

In order to study the flow around a plunging airfoil a new experimental method is presented in this chapter. In this new method the airfoil is fixed to the wind tunnel walls and the flow is displaced by an acoustic standing wave generated by loudspeakers. This is in contrast to the conventional method where the airfoil is physically displaced with respect to the flow. Because we use the transversal acoustic resonance of the test section of the wind tunnel this acoustical behaviour of the test section is investigated in detail. The experimental setup is verified by measurements on a standard NACA0018 airfoil and comparison with numerical simulations of the Euler equations, which includes the acoustic field.

First a short introduction is given in section 3.1. Then the experimental setup is described in section 3.2. In section 3.3, the acoustic field in the test section, decoupled from the wind tunnel, is investigated in an anechoic room and experimental results are compared to results of a commercial numerical Indirect Boundary Element Method (IBEM). Also the influence of the wing on the acoustic field inside the test section is investigated. Then the acoustic field inside the test section placed in the wind tunnel is discussed. The numerical method is introduced in section 3.4. The results of measurements on a standard NACA0018 airfoil will be presented and compared with the results of two-dimensional numerical simulations using the Euler method and the linearised potential flow theory in section 3.5. Here also the relation between acoustically forcing the airfoil and the plunging motion of the airfoil is explained. Lastly in section 3.6 a conclusion is given.

---

\*Part of this chapter has been adopted from W.F.J. Olsman et al. "Acoustic Forcing to Simulate the Plunging Motion of an Airfoil", J. Sound and Vib. 2010.

### 3.1 Introduction

The work presented in this chapter was carried out within the framework of the European project VortexCell2050 (2005). As was already mentioned in the introduction of this thesis, the scope of this project is to design a relatively thick wing without massive vortex shedding. In order to prevent downstream vortex shedding, the vortex is trapped in a cavity in the vicinity of the wing.

Our long term goal is to gain insight into the dynamical behaviour of such a wing with a cavity. We will argue that significant effects of a cavity may be expected at reduced frequencies much higher than commonly encountered in the study of classical wing bending-torsion flutter. This calls for the development of an alternative experimental method. In the present chapter we explore the potential of a new method to perform unsteady measurements on an airfoil, using acoustic forcing.

It is known that a cavity in a plane wall can display a shear layer instability mode when the Strouhal number<sup>†</sup>,  $k_W = \omega W/U_\infty \approx 3$ , where  $W$  is the opening of the cavity,  $\omega$  is the angular frequency in rad/s and  $U_\infty$  is the main stream velocity. If one wants to achieve a Strouhal number  $k_W \approx 3$  and the opening of the cavity is  $W = 2b/5$ , with  $b$  the semi-chord of the airfoil, this means that the reduced frequency  $k = \omega b/U_\infty$  must be approximately 8, which is for an airfoil a high value of the reduced frequency.

The conventional method for dynamic measurements on an airfoil is to mount the airfoil on a rig, which is displaced with respect to the main flow by a mechanical system, see Halfman (1952) and Schewe *et al.* (2003). The challenge with such an approach is to design a light and stiff setup to prevent the mechanical eigenfrequencies of the setup interfering with the measurements. It is difficult to reach high values of the reduced frequency due to the inertia of the moving parts of the setup. With the proposed alternative method, in which the airfoil is fixed to the wind tunnel walls and the flow is modulated by loudspeakers, these problems are avoided and

---

<sup>†</sup>Note that in the literature concerning cavities the Strouhal number is usually defined as  $fW/U_\infty$ , with  $W$  the opening of the cavity,  $U_\infty$  the free stream velocity and  $f$  the frequency in Hz. In the literature about dynamical behaviour of airfoils the Strouhal number is defined as  $k = \omega b/U_\infty$ , with  $b$  the half chord of the airfoil and  $\omega$  the angular frequency in rad/s. This last definition of the Strouhal number corresponds to the definition of the reduced frequency in the literature about flutter; in this chapter we will use this definition of the Strouhal number.

there is no need for a complex mechanical system to displace the airfoil. By exciting the system at the first acoustical transversal resonance we aim to reach high fluctuating velocity amplitudes and a reasonably uniform excitation. This experimental setup will make it possible to conduct high reduced frequency dynamical measurements on an airfoil. It also allows for easy variation of the excitation amplitude. Acoustic excitation has been considered as a means to study the stalled flow over an airfoil at low speed by Zaman (1992). The effect of acoustic excitation of the laminar boundary layer was investigated by Archibald (1975). However, to our knowledge, acoustic excitation has not been used in order to obtain information on the dynamical response of airfoils at high Reynolds numbers. Furthermore, there was no quantitative description of the acoustic field around the airfoil.

Quantitative implementation of the measurement method involves an analysis of the acoustic response of the wind tunnel to acoustic excitation. The acoustic field in an infinite duct with uniform subsonic flow was studied numerically by Mosher (1986). Prediction of acoustic resonant frequencies in wind tunnel test sections with plenum chambers, assuming infinite length in streamwise direction and uniform flow is provided by Lee (1988).

In the wind tunnel considered here, the test section is connected on the upstream side to the settling chamber by a contraction and on the downstream side to the diffuser. Between the end of the test section and the inlet of the diffuser there is a slit. The purpose of this slit is to prevent a very low pressure in the test section. Since seen from the test section both the contraction and the slit/diffuser are area expansions, this implies that they will partially reflect acoustic waves. A duct segment with two open ends shows therefore qualitatively the same acoustic behaviour as the test section placed in the wind tunnel.

## 3.2 Experimental method

The test facility is a low-speed wind tunnel with a test section with square cross section  $500 \text{ mm} \times 500 \text{ mm}$ , and a length of  $1000 \text{ mm}$ . The walls of the test section are manufactured from plywood with a wall thickness of  $24 \text{ mm}$ . They are reinforced with wooden ribs of  $100 \text{ mm}$  height and  $36 \text{ mm}$  width, to reduce the effects of wall vibrations. Ribs meeting at junctions of walls are connected by means of L-shaped steel plates ( $150 \text{ mm}$  side length,  $40 \text{ mm}$  width and  $4 \text{ mm}$  thickness). The maximum velocity in the test section is about  $67 \text{ m/s}$ , which corresponds to a free stream Mach

number of  $M_\infty = 0.19$  at room temperature. The velocity is determined by measuring the pressure difference between the settling chamber and the test section with a water manometer, neglecting the velocity in the settling chamber. The contraction ratio of settling chamber to test section is 16. The velocity is determined with an accuracy of 0.2%. The turbulence intensity in the empty test section is less than 0.2%, in a frequency range of 0.1 Hz to 5 kHz.

In each of the two opposite side walls of the test section a circular hole with a diameter of 200 mm, covered with fabric, has been made. On the outside of the test section two speakers (JBL 2206H) are mounted over these holes, one on each side of the test section. The loudspeakers are not fixed to the test section but mounted on an independent rigid aluminium frame. The slit between the test section wall and the rim of the loudspeaker is filled with a 5 mm thick rim of closed-cell foam. This provides an acoustical seal with a minimum of mechanical contact. The speakers are connected in series and opposite phase, such that both membranes have displacements in the same direction with respect to each other. The speakers are driven by an amplifier (QSC RMX2450) which in turn is driven by a function generator (Yokogawa FG120). In both side walls and the top wall of the test section piezoelectric pressure transducers (PCB 116A and Kistler 7031) are mounted. The transducers are positioned in order to measure the acoustic field. The microphones are acceleration compensated in the axial direction but display significant errors when fixed directly to a vibrating wall. The transducers are therefore mounted on a 1 cm thick layer of closed-cell foam, which is glued to the wall of the test section. They have been mounted such that there is no direct mechanical contact with the wall. The eigenfrequency of the microphone with foam suspension is tuned to be significantly below the frequency at which the speakers are driven. This isolates the microphones from wall vibrations. A top view of the test section is given in figure 3.1, some of the stiffeners are also shown in this view. The origin of the coordinate system used is in the lower left inside of the test section in figure 3.1. The locations of the microphones are shown in figure 3.1, by the labels M1-M5. The type of microphone and its exact mounting location are given in table I.

In the middle of the test section an airfoil can be mounted vertically. The airfoil used here is manufactured out of extruded aluminium and approximates the NACA0018 profile definition within a maximum deviation of 0.2 mm. The chord  $2b$  of the airfoil is 165 mm and the width is 495 mm

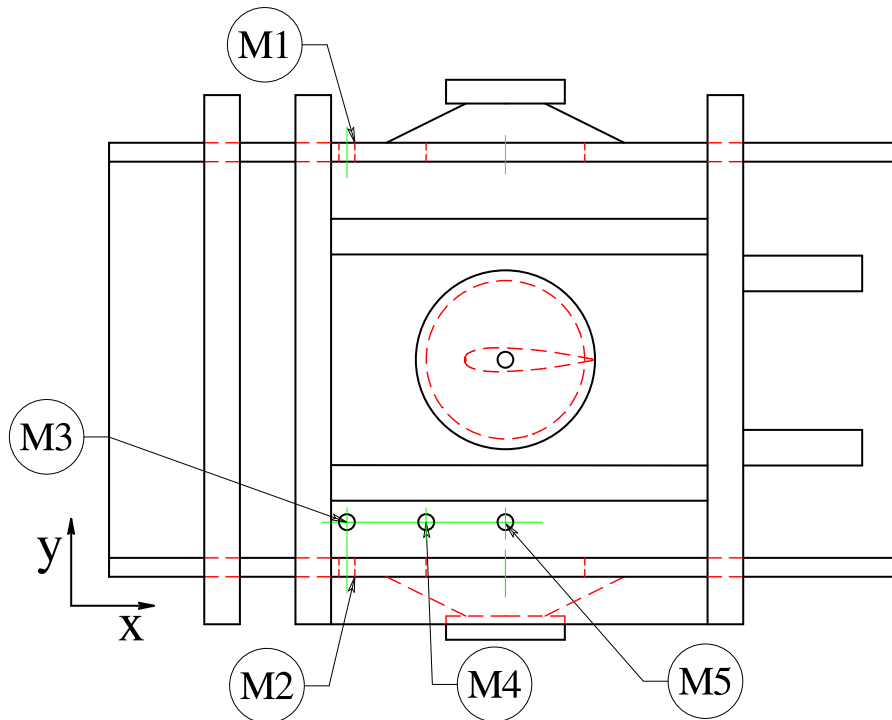


**Figure 3.1** – Top view of the test section of the wind tunnel with speakers mounted and the airfoil placed in the middle. The pressure transducers mounted in the side and top walls are indicated with M1 to M5. The flow through the test section is from left to right.

such that it spans the entire test section from top to bottom, closing tightly at the ends. The vertical positioning of the airfoil provides practical advantages related to the placement of experimental equipment. The bottom of the airfoil is fixed by a pin-in-hole connection. The top is connected by a tube to a flange which is bolted to the test section. This allows for modification of the angle of attack of the airfoil, which can be set with an accuracy of 0.5 deg. At an angle of attack of zero degrees the blockage in the test section is 2%.

In the airfoil two miniature dynamic pressure transducers (Kulite XCS-093-140mBarD) are placed flush to the surface, on either side of the airfoil at a position of 13.3% of the chord measured from the leading edge. The geometry of the NACA0018 profile with the location of the pressure transducers is shown in figure 3.2. This location has been chosen because the pressure fluctuations are expected to be highest there. The part of the air-



Microphone	Position $(x, y, z)$ (mm)	type
M1	(300, 500.0, 250)	Kistler 7031
M2	(300, 0.0, 250)	PCB 116A
M3	(300, 45.0, 500)	Kistler 7031
M4	(400, 45.0, 500)	Kistler 7031
M5	(500, 45.0, 500)	PCB 116A

**Table I** – Position and type of microphones placed in the walls of the test section.

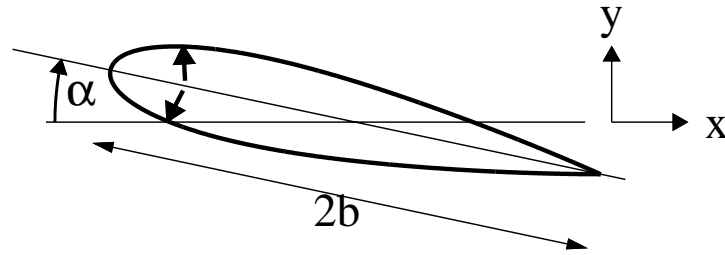


**Figure 3.2** – Standard NACA0018 profile with chord  $2b = 165$  mm. The location of the pressure transducers is indicated by the arrows inside the profile. The angle of attack is defined positive as indicated in the figure.

foil containing the pressure transducers has been sealed air tight, except for the circular tube which extends out of the wind tunnel. The cavities inside the airfoil are filled at the spanwise ends with sound absorbing foam to prevent acoustic standing waves inside these cavities.

All signals from the pressure transducers and the signal from the function generator are recorded with a National Instruments data acquisition system (NI SCXI-1000). The unsteady data is post-processed using a lock-in method, which allows the extraction of the component of the pressure signal at the excitation frequency and determine its phase. The phase of all the signals is determined with respect to the signal generated by the function generator which is driving the amplifier of the speakers. A Hilbert transform is used to obtain a complex harmonic function from the reference signal.

The function generator is tuned to the first transversal eigenfrequency ( $f = 331$  Hz) of the wind tunnel with the wing installed, creating a transversal standing wave. The non-dimensional number which indicates the size of the airfoil compared to the acoustic wave length is the Helmholtz number  $He = \frac{2\pi b}{\lambda}$ , with  $b$  the semi-chord of the wing and  $\lambda$  the acoustic wave length. If  $He^2$  is small compared to unity the acoustic field around the airfoil is called compact and can be locally approximated as an incom-

pressible potential flow, see Dowling & Ffowcs Williams (1983); Landau & Lifshitz (1959). For the case considered here  $He^2 \approx 0.25$ , which indicates that the effects of the Helmholtz number might not be negligible. Because  $He^2 \ll 1$  the airfoil in an acoustically forced flow is expected to be similar to moving the airfoil normal to the main flow in a steady uniform flow. The relation between an oscillating airfoil in a steady uniform flow and a fixed airfoil in an oscillating flow will be discussed in detail in section 3.5.4. Typically the non-dimensional amplitude of the velocity oscillation at the centre of the wind tunnel, with wing installed, can reach an amplitude  $v'/U_\infty = O(10^{-1})$ . Here  $v'$  denotes the amplitude of the velocity fluctuation in  $y$ -direction in the centre of the test section, where the prime indicates an acoustic velocity, and  $U_\infty$  is the uniform free stream velocity.

The value of the reduced frequency  $k$  can be varied by adjusting the free stream velocity  $U_\infty$ . For the current setup reduced frequencies in the range of  $2.5 < k < 10$  can be obtained. In the experiments the Reynolds number,  $Re_c$ , based on the chord length  $c = 2b$ , varies from  $2 \cdot 10^5$  to  $7 \cdot 10^5$ .

### 3.3 Acoustics without main flow

Since the Mach number in the measurement is about  $M_\infty = 0.19$  or smaller, the convective effect of the flow on the acoustic field is expected to be small. Therefore an analysis of the acoustics without main flow is reasonable. The measurements are carried out in a wind tunnel for which the transversal velocity fluctuations are associated with a transversal acoustic standing wave. Due to the complex geometry of the wind tunnel determining the acoustic behaviour is not trivial. A very simple (and crude) model to describe the acoustical properties of the test section in a wind tunnel is to consider the test section as a square duct of infinite length, see Mosher (1986). However, the test section in the wind tunnel is not infinitely long. The test section has a constant cross-section and on the upstream side it is connected air tight to the settling chamber by the contraction. The contraction has an area ratio of settling chamber to test section of about 16 and this area contraction takes place within 1.8 m. This is a rapid area expansion on the length scale of an acoustic wave length  $c/f \approx 1$  m, with  $c$  the speed of sound and  $f$  the frequency in Hz. For plane waves using the Webster approximations, see Dowling & Ffowcs Williams (1983), one would expect the configuration to behave like a horn, reflecting waves below 40 Hz, while transmitting waves at higher frequencies. We consider here, however, a transversal acoustic

wave which from our numerical simulations appears to partially reflect. At the other end of the test section, on the downstream side, there is a slit between the end of the test section and the diffuser. This slit will also reflect acoustic waves. A slightly more sophisticated model than an infinite duct is that of a square duct of finite length, i.e. a duct segment with two open ends. Firstly the acoustics of an infinite duct is briefly discussed, after that the behaviour of a duct of finite length is explained and the influence of the placement of the airfoil in the test section is discussed. Results of numerical simulations of the acoustic field in the test section will be compared with measurements. Lastly deviations from this simple model are discussed and measurements in the wind tunnel will be presented. We focus on the acoustic behaviour at the first transversal resonance frequency of the test section, which we will use in our further experiments.

### 3.3.1 Infinite duct

The square duct with the used coordinate system is shown in figure 3.3. The theory of infinite ducts can be found in many text books, such as Dowling & Ffowcs Williams (1983). Below the cut-off frequency only plane waves travel down the duct away from the sound source (the loudspeakers). The first transversal resonance frequency occurs when half a wave length fits in the duct. This resonance frequency coincides with the cut-off frequency of the duct  $f_c = c/2L$ , which for the duct considered here is approximately 340 Hz. At this resonance frequency the acoustic field is one-dimensional. The acoustic variables pressure  $p'$ , density  $\rho'$  and velocity  $v'$  depend only on the  $y$ -coordinate. The pressure distribution in  $y$ -direction has the shape of a half cosine,  $A \cos \frac{\pi y}{L}$ , where  $A$  is the amplitude. Above the cut-off frequency also non-planar waves can travel down the duct, i.e. in the  $x$ -direction.

### 3.3.2 Acoustical validation setup

In order to gain insight into the acoustic field distribution within the test section, the section is taken out of the wind tunnel and placed in a semi-anechoic chamber (the floor is reflecting). This allows the investigation of the acoustic field by means of a traversable microphone (PCB 116A) and imposes well defined radiation boundary conditions. The volume of the room is about 80 m<sup>3</sup> and the room is non-rectangular in cross section. The test section is placed in the middle of the chamber and orientated such that it is not parallel to any of the side walls. The bottom of the sec-

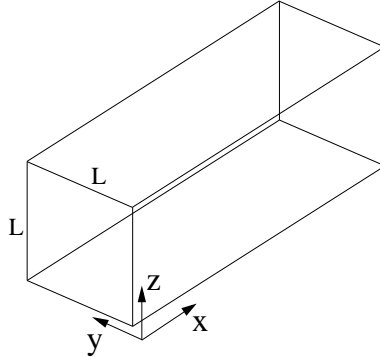


**Figure 3.3** – Sketch of a duct with the definition of the coordinate system.

tion is approximately 1 m above the floor. The traversable microphone is positioned by hand with an accuracy of a few millimeters. The results of the measurements in the anechoic chamber are presented in sections 3.3.3 and 3.3.4, and compared to results of numerical simulations. These measurements allowed to verify the response of the wall-mounted microphones by comparison with the traversable microphone. These agreed within 5%, confirming the effectiveness of the isolation of the transducers from wall vibrations.

### 3.3.3 Finite duct

The acoustics of a duct segment with open ends is discussed in this section. Acoustic waves that travel down the duct will partially reflect at the open ends. The radiation to free space from a rectangular duct close to the transversal resonance frequency is not trivial. We investigate the acoustic field by numerically solving the Helmholtz equation with the commercial software package SYSNOISE (2005). The IBEM option of SYSNOISE was used. This corresponds to the solution of the Helmholtz equation, ignoring the effects of friction and heat transfer at the walls. For the simulations of the test section an equidistant mesh with 4608 quadrilateral boundary elements was used. The numerical model consists of a three-dimensional model of the duct. At the open ends of the duct the condition of continuity of pressure between the inside and outside of the duct is applied.

In the numerical method the speakers are modelled flush to the wall and in a circular area covering the speakers a hard velocity profile is prescribed. The profile of the amplitude of the acoustic velocity that is prescribed is

an axisymmetric half cosine,  $\frac{1+\cos\frac{\pi r}{R}}{2}$  for  $0 \leq r \leq R$  where  $r$  is the radius measured from the center of the speaker and  $R$  is the radius of the speaker, such that the velocity at the boundary of the speakers is zero. The walls are modelled as rigid walls. Note that by prescribing a hard velocity profile at the speakers the surface of the speakers will fully reflect acoustic waves, just as a rigid wall. The results of both experiment and numerical simulation are plotted in figures 3.4(a) and 3.4(b).

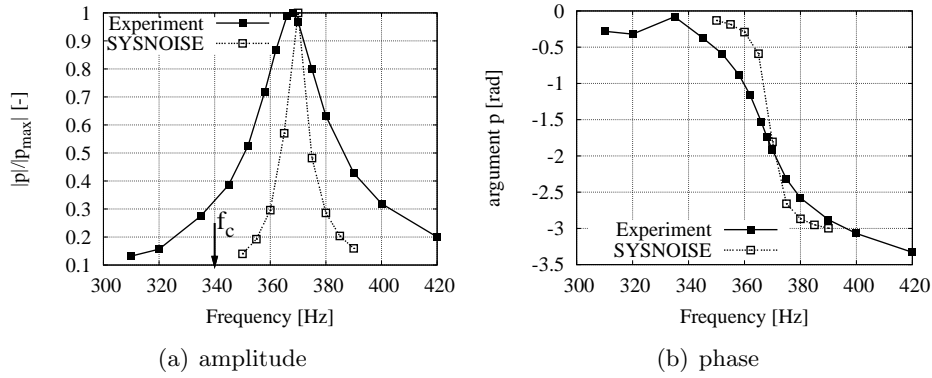


**Figure 3.4** – Amplitude of the pressure (a) and corresponding phase (b) in a finite duct as a function of frequency, measured with microphone M2. The phase is determined with respect to the signal from the function generator. Experimental data are indicated by the solid line with solid squares, the results of numerical simulations are plotted as a dashed line with open squares. The cut-off frequency, for non-planar waves, is indicated by  $f_c$  and the arrow. The amplitude maxima are normalised to unity and there is an arbitrary shift in phase of the numerical data, to allow easy comparison.

In figure 3.4(a) the pressures are normalised using their maximum value and the phase is determined with respect to the signal from the function generator. From figure 3.4(a) it is clear that the numerical method predicts the resonance frequency within 2 Hz. However, the peak of the experiment is much wider than the peak in the results of the numerical method. A measure of the amount of damping in a system is the quality factor,  $Q = f_0/\Delta f_{3\text{dB}}$ . Here  $f_0$  is the resonance frequency and  $\Delta f_{3\text{dB}}$  is the width of the resonance peak 3 dB below the resonance peak. The quality factor from the numerical method is about 60, while it is 20 in the experiment. This indicates that there are significant energy losses other than radiation losses. Possible explanations for the deviations between results of experiment and numerical method are wall vibrations, small geometric deviations between

the actual setup and the mesh used, and the simplified model to represent the loudspeakers. Visco-thermal losses are not expected to be significant.

Since our aim is to understand more about the acoustic behaviour and the quantitative influence of certain parameters rather than the correct modelling of the acoustic losses we will not further investigate the deviation between the results of the numerical simulations and those of the experiments. From figure 3.4(a) it can be seen that the resonance frequency of the duct with open ends is 368 Hz, which is significantly higher than the cut-off frequency  $f_c = 340$  Hz. The observed resonance frequency agrees well with the results of the formula

$$f = \frac{c}{2} \sqrt{\left(\frac{1}{2L + 2\delta}\right)^2 + \left(\frac{1}{L}\right)^2} \quad (3.1)$$

given by Blevins (1979). For end corrections  $\delta = 0.6 \frac{L}{\sqrt{\pi}}$  at the open ends, this formula predicts a resonance frequency of 367 Hz.

Figures 3.5(a) to 3.6(b) show the results of measurements of the acoustic pressure inside the test section and results of a numerical simulation with SYSNOISE. The acoustic field is plotted at the resonance frequency of 368 Hz for the experiments and at 370 Hz for the numerical simulations. The overall agreement is good, even though the energy losses are not accurately modelled/predicted. The numerical method predicts a two-dimensional acoustic field. In the experiment small three-dimensional effects (variations in  $z$ -direction) of the order of 5% are observed. Figures 3.5(a) and 3.5(b) show the acoustic pressure as a function of the  $x$ -coordinate, along a line with  $y = 0.045$  m and  $z = 0.48$  m. Note that the open end of the duct is at  $x = 0$  m and the middle is at  $x = 0.50$  m. It can be seen in figure 3.5(a) that the acoustic pressure is not zero at  $x = 0$ . This is due to the inertia of the acoustic flow outside the duct and corresponds to the so-called “end-corrections” for reflection of plane waves at an open pipe termination. Figures 3.6(a) and 3.6(b) show the acoustic pressure as a function of the  $y$ -coordinate, along a line with  $x = 0.30$  m and  $z = 0.25$  m. The distribution in the experiment agrees with a half cosine profile, within 5%.

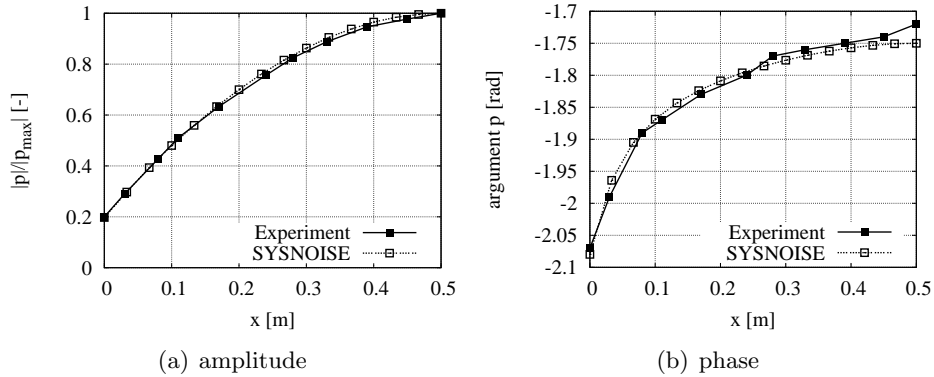


**Figure 3.5** – Amplitude (a) and corresponding phase (b) in a finite duct as a function of  $x$  for  $y = 0.045$  m and  $z = 0.48$  m. Experimental data, obtained with a traversing microphone, are indicated by the solid line with solid squares, the results of numerical simulations are plotted as a dashed line with open squares. The phase is determined with respect to the signal from the function generator. An arbitrary shift in phase is added to the numerical data to allow easy comparison.

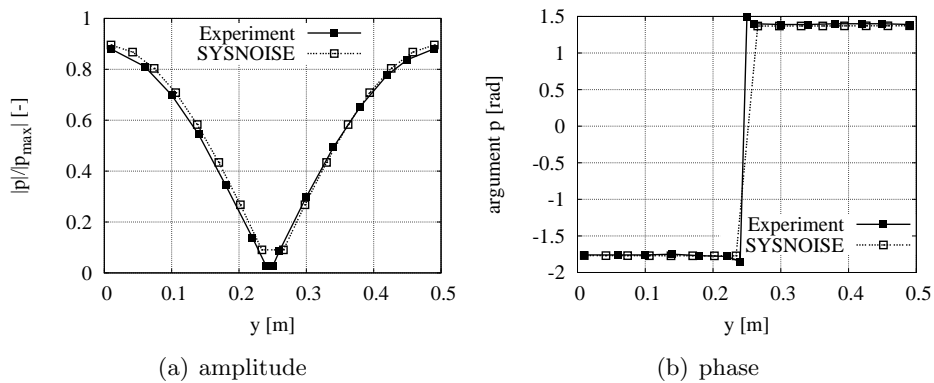


**Figure 3.6** – Amplitude (a) and corresponding phase (b) in a finite duct as a function of  $y$  for  $x = 0.30$  m and  $z = 0.25$  m. Experimental data, obtained with a traversing microphone, are indicated by the solid line with solid squares, the results of numerical simulations are plotted as a dashed line with open squares. The phase is determined with respect to the signal from the function generator. An arbitrary shift in phase is added to the numerical data to allow easy comparison.

### 3.3.4 Test section with wing installed

In the preceding section the acoustic field inside the test section without wing was investigated. In this section the same measurements are carried out as those in the preceding section, however, now the wing is inserted in the test section. In the numerical method the wing is modelled as a rigid flat plate without thickness, with 192 boundary elements. Calculations with a NACA0018 profile have also been carried out. These yield essentially results identical to the ones obtained for the flat plate.

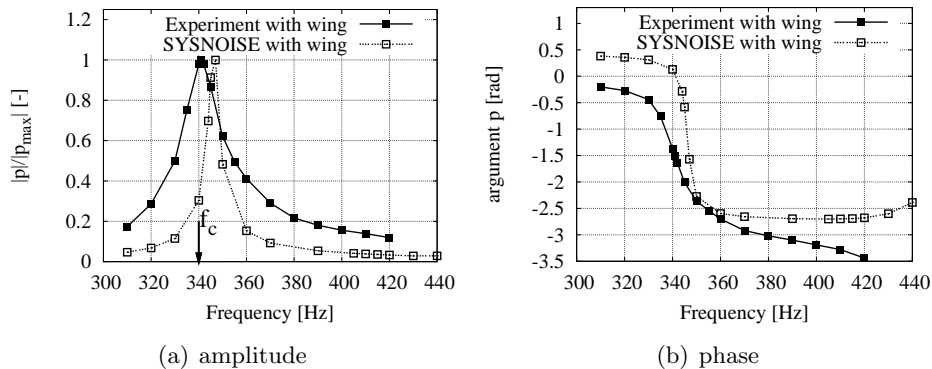


**Figure 3.7** – Amplitude of the pressure (a) and corresponding phase (b) in a finite duct with wing installed, as a function of the frequency, measured with microphone M2. Experimental data are indicated by the solid line with solid squares, the results of numerical simulations are plotted as a dashed line with open squares. The phase is determined with respect to the signal from the function generator. An arbitrary shift in phase is added to the numerical data to allow easy comparison.

Figure 3.7(a) shows that the resonance frequency is now 341 Hz in the experiment and 346 Hz in the numerical method. The drop in the resonance frequency by about 20 Hz, due to the presence of the airfoil, is caused by the increased distance the acoustic waves have to travel to get around the airfoil. The phase is shown in figure 3.7(b). The quality factor of the results from the numerical method is  $10^2$ , while it is 26 in the experiment.

Figures 3.8(a) to 3.9(b) show the results of traverse measurements and the corresponding numerical results. Again the measurements are taken at the resonance frequency of 341 Hz, and the numerical results are shown at 346 Hz. The results in  $x$ -direction are shown along a line  $y = 0.045$  m and  $z = 0.48$  m. The results in  $y$ -direction are shown along a line  $x = 0.30$  m and  $z = 0.25$  m. In figures 3.8(a) and 3.8(b) also the experimental results without wing are shown for comparison.



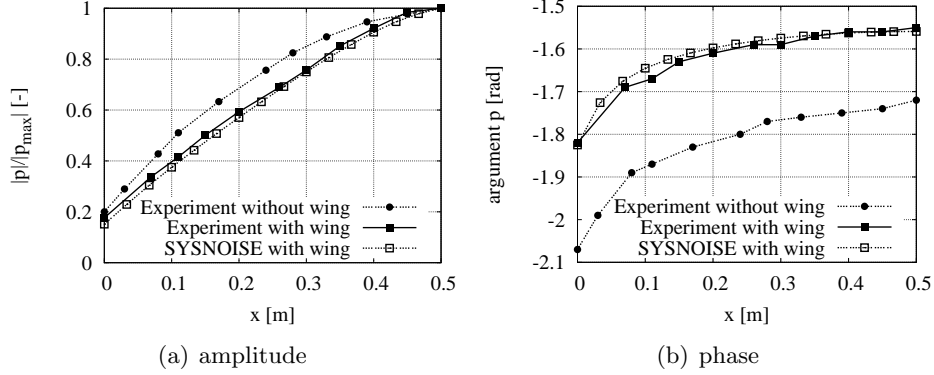


**Figure 3.8** – Amplitude (a) and corresponding phase (b) of the pressure in a finite duct with wing, as a function of  $x$  for  $y = 0.045$  m and  $z = 0.48$  m. Experimental data are indicated by the solid line with solid squares, the results of numerical simulations are shown as a dashed line with open squares. The results of measurements in the duct without wing are plotted by the dotted line with solid circular markers. The phase is determined with respect to the signal from the function generator. An arbitrary shift in phase is added to the numerical data to allow easy comparison.

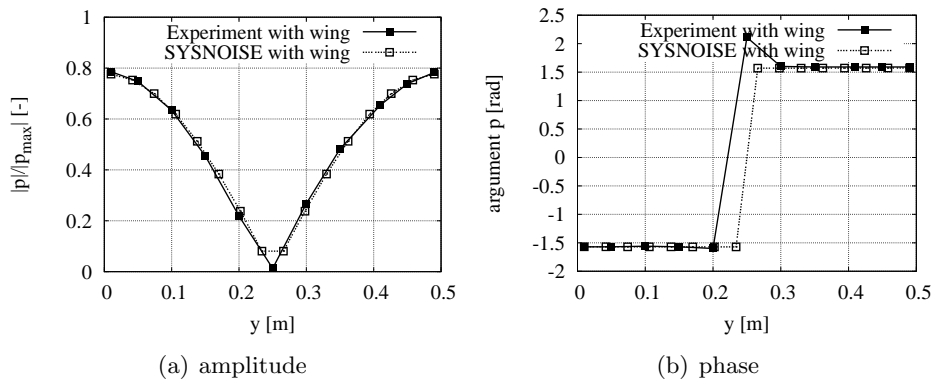


**Figure 3.9** – Amplitude of the pressure (a) and corresponding phase (b) in a finite duct with wing installed, as a function of  $y$  for  $x = 0.30$  m and  $z = 0.25$  m. Experimental data are indicated by the solid line with solid squares, the results of numerical simulations are plotted as a dashed line with open squares.

Comparing figures 3.8(a)–3.9(b) to 3.5(a)–3.6(b) we see that the acoustic field is qualitatively the same. However, when we look in more detail at figure 3.8(a) we note that the acoustic field with wing diminishes faster in the  $x$ -direction towards  $x = 0$ , than for the case without wing. This implies that the resonant mode is more localised, which agrees with the fact that the quality factor is higher with the wing installed. If the wing chord ( $2b$ ) were comparable to the wind tunnel width ( $L$ ) a pure Parker- $\beta$  mode would appear, resulting in a localisation of the acoustic field around the wing, see Parker (1967). Even though the chord of the wing is much smaller than the width of the test section ( $c \approx L/3$ ) we still observe some localisation.

### 3.3.5 Test section in wind tunnel without wing

Now that we have a fair understanding of the acoustic field in the test section with open ends, the test section is placed back in the wind tunnel. The presence of a contraction and settling chamber upstream of the test section and the slit/diffusor downstream will make the acoustic field more complex than for the case of the isolated test section. The influence of the gap, between the test section and the diffusor, is expected to depend mainly on the width of the gap. In the current case the width of the gap is about 20 mm, which is small compared to the wave length (1 m).

Due to the three-dimensional geometry of the contraction the acoustic field inside the contraction will also be three-dimensional. Therefore a numerical method for three-dimensional fields is needed. In the numerical domain the wind tunnel extends from the middle of the settling chamber up to 4 m downstream of the slit. At both ends of the numerical domain anechoic boundary conditions are imposed. This boundary condition is actually only anechoic for waves at normal incidence. This choice appears to yield a reasonable fit of experimental data. The mesh is refined near the location of the slit. A total number of about 17500 quadrilateral boundary elements is used for this computational domain.

The acoustic pressure measured by microphone M2 as a function of the frequency, without wing installed, is shown in figure 3.10(a), the corresponding phase is plotted in figure 3.10(b).

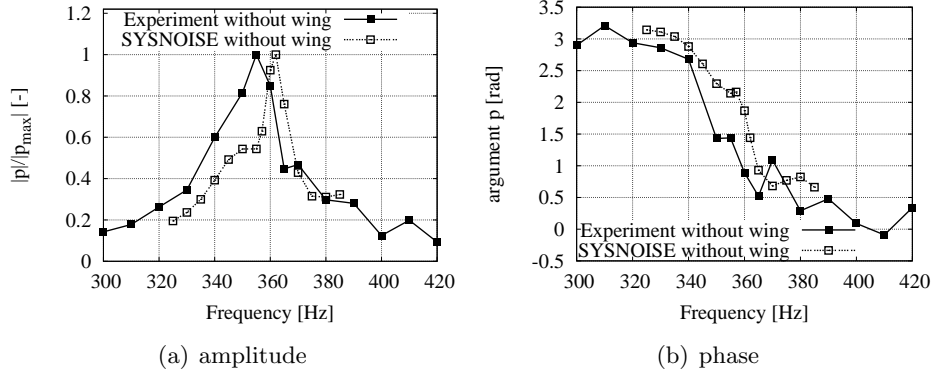


**Figure 3.10** – Amplitude of the pressure (a) and corresponding phase (b) in the test section while placed in the wind tunnel, as a function of the frequency, without wing installed. Measured by microphone M2. Experimental data are indicated by the solid line with solid squares. The phase is determined with respect to the signal from the function generator. An arbitrary shift in phase is added to the numerical data to allow easy comparison.

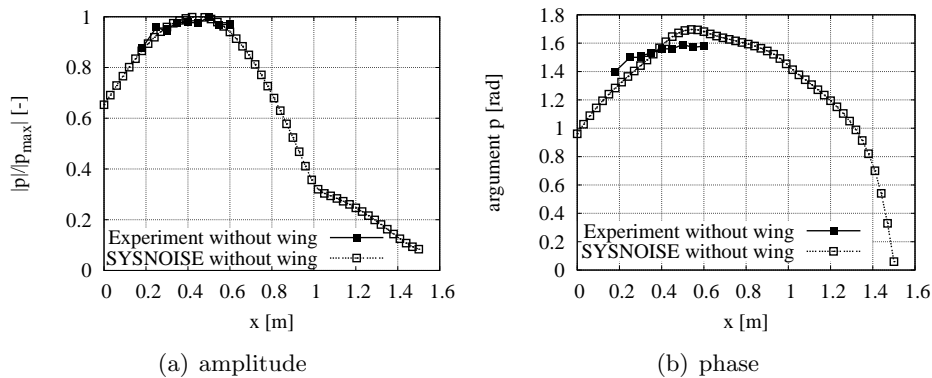


**Figure 3.11** – Amplitude of the pressure (a) and corresponding phase (b) in the test section while placed in the wind tunnel without wing installed, as a function of  $x$  for  $y = 0.045$  m and  $z = 0.45$  m. Experimental data are indicated by the solid line with solid squares. The phase is determined with respect the signal from the function generator. An arbitrary shift in phase is added to the numerical data to allow easy comparison.

It is seen that the resonance frequency is 355 Hz, in figure 3.10(a), which is lower than the 368 Hz found for the test section placed in the anechoic room, see figure 3.4(a). Measurements of the acoustic pressure distribution in the  $x$ -direction, at 355 Hz, are shown in figures 3.11(a) and 3.11(b), for  $y = 0.045$  m and  $z = 0.45$  m. The measurements are taken with a microphone which is inserted in the wind tunnel through the slit downstream of the test section. Care is taken to prevent direct contact between the microphone and the wind tunnel walls, in order to avoid transfer of vibrations. The measured pressure distribution along the  $x$ -axis agrees reasonably well with the prediction of the acoustic field by SYSNOISE at 360 Hz. Variations in the  $z$ -direction at  $x = 0.30$  m were observed in the experimental measurements in the order of 10%, while the numerical model predicts very little three-dimensional effects in the test section.

### 3.3.6 Test section in wind tunnel with wing installed

Now the wing is installed into the test section and the amplitude and phase are measured at the side wall with microphone M2, the results are shown in figures 3.12(a) and 3.12(b). The resonance frequency has shifted down to 331 Hz. The numerical model is the same as that used in the previous section, with the exception of the placement of a rigid plate to model the wing, which is modelled by 240 boundary elements. Figures 3.13(a) and

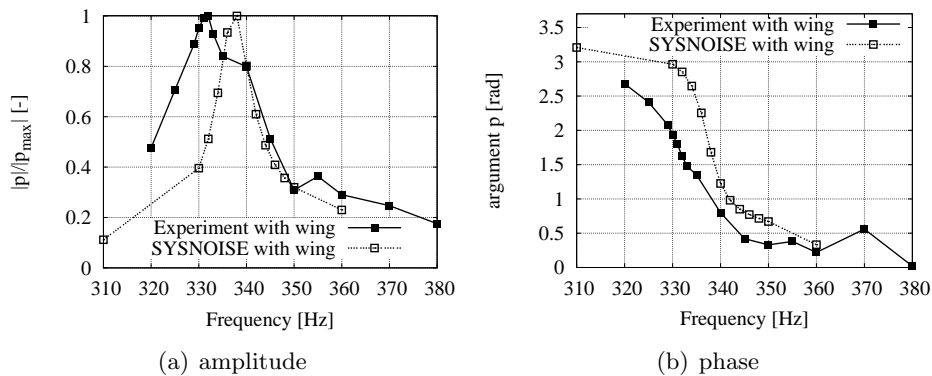


**Figure 3.12** – Amplitude of the pressure (a) and corresponding phase (b) in the test section while placed in the wind tunnel with wing installed, as a function of the frequency. Experimental data are indicated by the solid line with solid squares. The phase is determined with respect to the signal from the function generator. An arbitrary shift in phase is added to the numerical data to allow easy comparison.

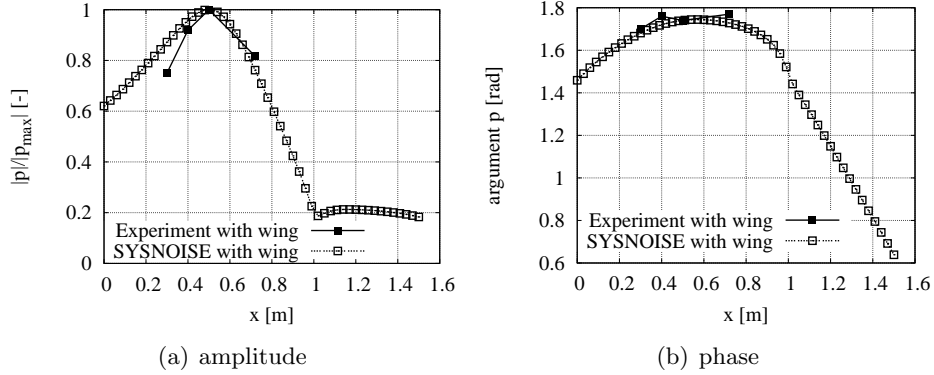


**Figure 3.13** – Amplitude of the pressure (a) and corresponding phase (b) in the test section while placed in the wind tunnel with wing installed, as a function of  $x$  for  $y = 0.045$  m and  $z = 0.45$  m. Experimental data are indicated by the solid line with solid squares. The phase is determined with respect to the signal from the function generator. An arbitrary shift in phase is added to the numerical data to allow easy comparison.

3.13(b) give the results of field measurements of the acoustic field inside the test section placed in the wind tunnel with the wing installed, along the  $x$ -direction, with  $y = 0.045$  m and  $z = 0.45$  m. We again observe some localisation of the acoustic field around the wing when we compare figure 3.13(a) to figure 3.11(a). In the experimental data a variation in  $z$ -direction of about 5% was observed at  $x = 0.30$  m. Note that even though the acoustic field inside the contraction and in the diffuser is three-dimensional the acoustic field inside the test section is still almost purely two-dimensional.

### 3.3.7 Determination of the transversal velocity

In the previous sections the acoustic pressure distribution was investigated. We are interested, however, specifically in the acoustic velocity fluctuations that the airfoil experiences. This means that we need an acoustic model to translate the measured acoustic pressures at the wall into an acoustic velocity at the centre of the wind tunnel at the location of the wing.

Complex notation will be used to define the amplitude of the acoustic pressure measured with the microphones,  $p = \hat{p}e^{i\phi}$ , with  $\hat{p}$  the amplitude and  $\phi$  the phase with respect to the reference signal. The complex  $e^{i\omega t}$  convention is used for the complex notation. The acoustic field is assumed to have a half cosine spatial distribution in  $y$ -direction, i.e.  $p'(y) = A \cos \frac{\pi y}{L}$ ,  $0 \leq y \leq L$ . The amplitude  $A$  is determined by the average amplitude of

microphones M1 and M2,  $A = \frac{p_1 - p_2}{2}$ . From this the acoustic velocity at  $x = 0.3$  m is calculated using the linearised Euler equation

$$\rho \frac{\partial v'}{\partial t} = - \frac{\partial p'}{\partial y}. \quad (3.2)$$

It follows that  $v'(y) = \frac{-i\pi A}{\rho\omega L} \sin(\frac{\pi y}{L})$ .

### 3.4 Numerical method for flow field

So far we have considered the acoustics without main flow. In order to compute the acoustics in the presence of a main flow, a numerical method based on the Euler equations is used. This numerical method for the Euler equations is the same as that used in Chapter 2.

A structured grid is generated with the built-in multi-block algebraic grid generator of EIA. A structured grid of 16 blocks is constructed, with an embedded C-grid around the profile. The total number of cells for this grid is 4032, with about 64 points per wavelength corresponding to the excitation frequency. Since it is impossible to represent the three-dimensional contraction and diffuser correctly in two-dimensional space it is chosen to leave out the contraction and the diffuser. Furthermore the placement of the wing is expected to localise the acoustic resonant mode. Therefore inflow/outflow boundary conditions will be less important in numerical simulations with an airfoil. In the numerical simulations the test section of the wind tunnel is modelled as a duct segment of 2.5 m. The inlet is located 0.838 m upstream of the leading edge of the airfoil. The position of the inlet was chosen such that the acoustic field in  $x$ -direction matches the acoustic field in the experiment. At the inlet and outlet of the duct anechoic boundary conditions are applied. Like in the case of the IBEM solution this boundary condition is only anechoic for waves at incidence normal to the boundary. It appears that these one-dimensional anechoic conditions perform reasonably well for the cases considered here. At the downstream side a vortex dissipation zone is added to dissipate vorticity before it reaches the end of the computational domain. This prevents the generation of spurious acoustic noise. The speakers are modelled by prescribed velocity fluxes (which corresponds to the physical situation of flush mounted moving pistons) at both at the upper and lower wall. Figure 3.14 shows a coarse version of the mesh. Due to the specific block decomposition of this structured grid, two “singular” points are necessary. These points are located outwards and

upstream of the airfoil at a distance of approximately  $c/2$  from the leading edge. At these singular points the corners of 5 (or 3) blocks meet. At these singular points the solution will be inaccurate if this point is in a region where the flow solution has large gradients, such as near the leading edge of the airfoil. Usually such errors show up in the solution as wiggles and spurious entropy production. The location of these points is away from regions of high gradients.

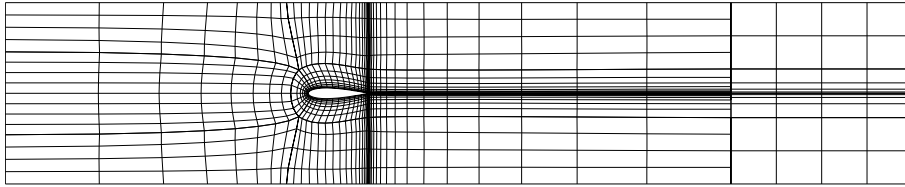


**Figure 3.14** – A coarse version of the grid used in the Euler calculations. The vortex dissipation zone is shown on the right end of the channel. The two “singular” points in the mesh are located upstream of the airfoil, approximately  $c/2$  from the leading edge.

## 3.5 Measurements on a NACA0018 airfoil

In this section measurements carried out on the NACA0018 airfoil will be presented. First the results in a steady flow will be presented and compared with results of numerical simulations. Then the results in an unsteady flow with acoustic forcing will be presented and these results will also be compared with results of numerical simulations.

### 3.5.1 Steady flow

As a test case we first consider the case without acoustic forcing, so there is only a main flow in the test section with velocity  $U_\infty$ . The pressure difference at 13.3% chord length from the leading edge is measured for several angles of attack  $\alpha$  and is plotted in figure 3.15. The results are presented as a difference in the pressure coefficient,  $\Delta C_p$ , between the lower and upper side of the airfoil  $\Delta C_p = \frac{2(p_{\text{lower}} - p_{\text{upper}})}{\rho_\infty U_\infty^2}$ , with  $\rho_\infty$  the free stream density. The angle of attack  $\alpha$  is defined positive nose-up, as indicated in figure 3.2. Figure 3.15 shows that the measurements of the non-dimensional pressure difference at 13.3% chord length from the leading edge agree well with the results of the Euler simulations up to  $\alpha = 8^\circ$ . For reference we also give results obtained for an airfoil in free field by means of a potential

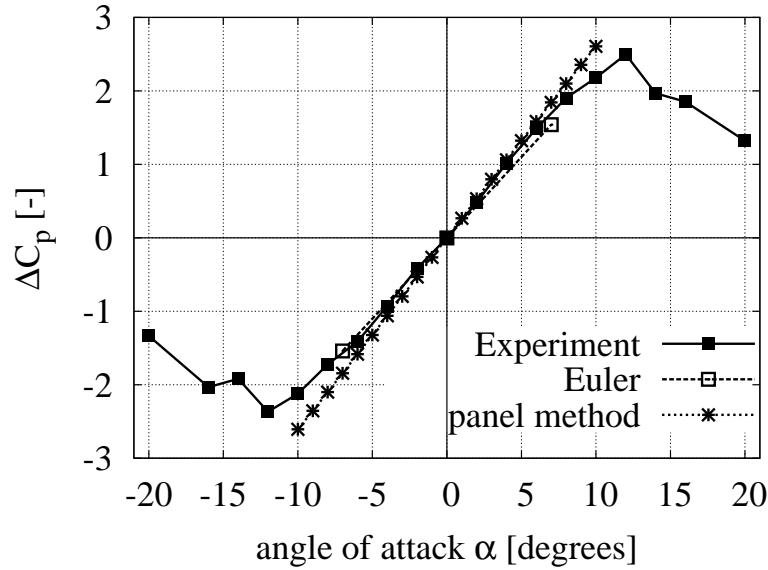


**Figure 3.15** – Non-dimensional pressure difference  $\Delta C_p$  over the airfoil at 13.3% chord from the leading edge as a function of the angle of attack for a standard NACA0018 airfoil (solid line with solid square markers). Also shown are the results of a potential flow panel method (dashed line with asterisks markers) and the results of numerical simulations using the Euler equations (dashed line with open square markers). Reynolds number in the experiments is  $Re_c = 4.5 \cdot 10^5$ .

flow panel method, for a description see Jacobs *et al.* (2008). The results of the panel method show a slightly higher difference in pressure coefficient, due to the absence of wind tunnel walls in this numerical method. Around  $\alpha = 10^\circ$  the measured data start to deviate from a straight line, which is an indication that the flow separates from the airfoil. The numerical Euler results have been verified to be grid independent by calculations on a coarser and a finer grid, this yielded the expected second-order convergence.

### 3.5.2 Unsteady flow

For the unsteady flow case, the speakers are tuned to the first transversal resonance frequency ( $f = 331$  Hz) of the wind tunnel with the wing installed. The angle of attack of the standard NACA0018 profile is set to zero degrees. The measurements have been performed for several values of the reduced frequency  $k$  by varying the free stream velocity  $U_\infty$ . Because the acoustic field has a dependency on the  $x$ -coordinate, also some velocity fluctuations in the  $x$ -direction will be generated. The wing, however, is



much more sensitive to velocity fluctuations in the normal direction than those in the direction of the flow.

The results are presented in terms of non-dimensional pressure differences, but now the unsteadiness of the flow is also taken into account. This is done by defining an unsteady non-dimensional difference in pressure coefficient,

$$\Delta C_{pu} = \frac{\Delta p_u}{\frac{1}{2}\rho_\infty U_\infty v'}, \quad (3.3)$$

where  $v'$  is the acoustic velocity at the centre of the wind tunnel, which is calculated from the measurements of the acoustic pressure at the walls (section 3.3.7). The subscript  $u$  is added to emphasise that this is an unsteady difference in non-dimensional pressure coefficient.

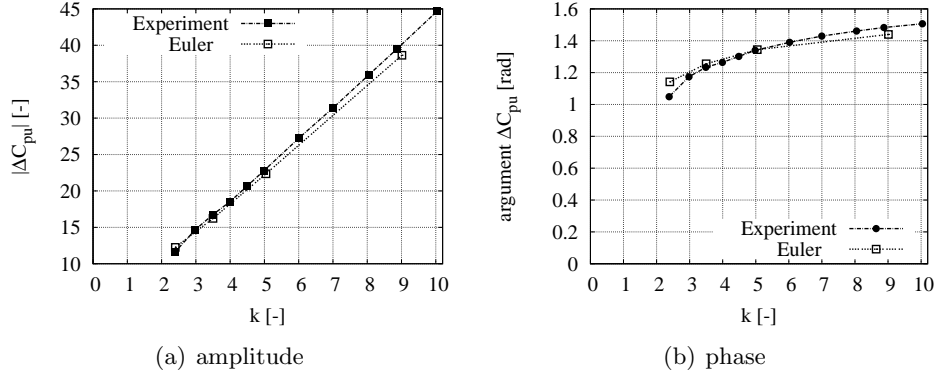


**Figure 3.16** – Amplitude of non-dimensional dynamical pressure difference (a) over a NACA0018 airfoil and corresponding phase (b) (solid line with solid square markers), for an amplitude  $\frac{v'}{U_\infty}$  varying from 1.4% at  $k = 2.4$  up to 9.7% at  $k = 10$  and  $1.9 \cdot 10^5 < Re_c < 7.9 \cdot 10^5$ . Also shown, the results of Euler method (dotted line with open square markers), with an amplitude varying from 2.6% at  $k = 3$  up to 11.4% at  $k = 9$ . The phase is determined with respect to the velocity fluctuation  $v'$ , at  $x = 0.3$  m.

The results are presented in the frequency domain, i.e., as an amplitude and a phase. The phase is determined with respect to the transversal acoustic velocity fluctuation at the centre of the wind tunnel. This transversal velocity is determined at  $x = 0.3$  m, from the amplitude of the acoustic pressure measured at the wall of the wind tunnel (see figure 3.1). Note that this location is  $1.81b = 149$  mm upstream of the airfoil's leading edge. The amplitude of the non-dimensional pressure difference is plotted in figure

3.16(a) as a function of the reduced frequency  $k$  and the corresponding phase is shown in figure 3.16(b). Also shown in the figure are results of numerical simulations using the Euler method. In the numerical method the velocity fluctuation is determined in the same way as in the experiments.

The agreement between the results of the Euler method and measured data is fair. To verify grid convergence, computations have been performed on a fine grid with 16128 cells for  $k = 2.5$  and  $k = 9$ . Also the time step size was reduced by a factor of two. The results on this fine grid differ from the coarse grid (4032 cells) results by less than 1.6%.

### 3.5.3 Estimation of plunging velocity

In the preceding section data was presented for which the acoustic velocity was calculated at  $x = 0.3$  m. However, the airfoil experiences a different velocity than that calculated at  $x = 0.3$  m. The preceding sections have shown that the acoustic field is not one-dimensional and has a dependency on the  $x$ -coordinate. The acoustic velocity measured at  $x = 0.3$  m by means of microphones M1 and M2 can be corrected for this  $x$ -dependency using the measurements of the acoustic pressures in the top wall with microphones M3 and M5. The acoustic velocity previously calculated is multiplied by the ratio of the complex-valued pressures of the microphones M5 and M3,

$$v'_{\text{corrected}} = v'_{\text{uncorrected}} \frac{p_5}{p_3}, \quad (3.4)$$

where  $v'_{\text{uncorrected}}$  is the acoustic velocity determined at  $x = 0.3$  m. The results of the measurements are shown in figures 3.17(a) and 3.17(b), for the uncorrected data, with the amplitude of the velocity fluctuation estimated at  $x = 0.3$  m. Also shown are the corrected data, for which the  $x$ -dependency of the acoustic field is taken into account. Also shown in the figure are results of Euler simulations. The velocity fluctuations in the numerical simulation are calculated from the pressure in the same way as in the measurements and corrected for the  $x$ -dependence of the acoustic field by the same procedure as for the experimental data.

The agreement between the results of the Euler method and measured data is fair, considering the application of artificial boundary conditions at the in and outflow, the neglect of physical viscosity and the fact that we used a two-dimensional flow method. The fact that computations and experiments agree, both for the uncorrected case and for the corrected case, is an indication that the acoustic field is well resolved in the results of the Euler method.

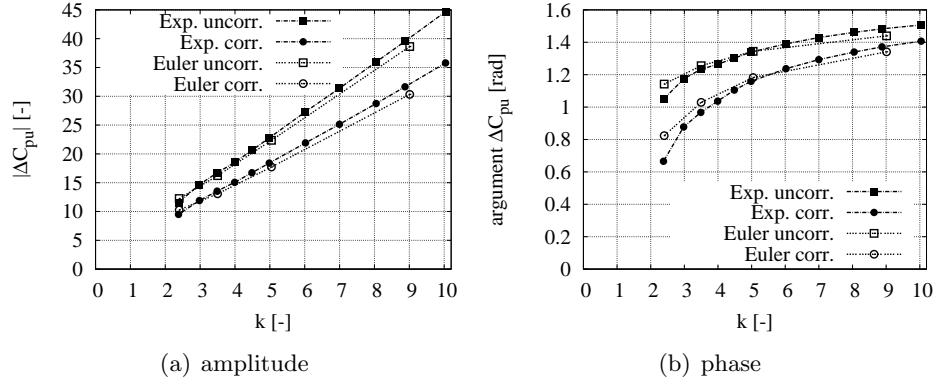


**Figure 3.17** – Amplitude of non-dimensional dynamical pressure difference (a) over a NACA0018 airfoil without any correction and corresponding phase (b) (solid line with solid square markers), results of NACA0018 measurements with acoustic correction taken into account (solid line with solid circular markers), for an amplitude  $\frac{v'}{U_\infty}$  varying from 1.4% at  $k = 2.4$  up to 9.7% at  $k = 10$  and  $1.9 \cdot 10^5 < Re_c < 7.9 \cdot 10^5$ . Also shown, the results of Euler method without correction (dashed line with open square markers) and with correction (open circular markers), with an amplitude varying from 0.85% at  $k = 2.4$  up to 7.5% at  $k = 9.0$ . The phase is determined with respect to the velocity fluctuation  $v'$ .

### 3.5.4 Relation to plunging motion

In the preceding subsections the experimental and numerical results of the acoustically forced airfoil have been presented. We will now discuss how these results relate to the plunging of the airfoil, for which the airfoil is physically displaced with respect to the flow. The fundamental difference between the case of a fixed airfoil in an oscillating flow and the case of an oscillating airfoil in a steady uniform flow is that in the case of an oscillating flow a time-dependent pressure gradient is present. This pressure gradient is necessary to accelerate the fluid particles of the oscillating main flow. This pressure gradient appears as an extra contribution to the pressure difference over the airfoil analogous to the hydrostatic pressure due to the acceleration of gravity, see Batchelor (1967); Streeter (1961).

This contribution to the non-dimensional unsteady pressure difference scales linearly with the reduced frequency and also linearly with the distance between the two pressure transducers measured in the direction perpendicular to the main flow.

For the case of a uniform oscillating flow the contribution to  $\Delta C_{pu}$  is given by

$$\Delta C_{pu} = \frac{2id \cos(\alpha)k}{b}, \quad (3.5)$$

where  $d$  is the local thickness of the airfoil. There is also a subtle difference between the acoustic oscillation and the plunging motion, namely the difference in the influence of the wind tunnel walls. Here we ignore these wall effects.

For the case of a flat plate without thickness, the problem of a plunging airfoil in a uniform steady flow can be solved by classical linearised potential flow theory. The local non-dimensional pressure difference is then given by

$$\Delta C_{pu} = 4 \left( C(k) \tan \frac{\theta}{2} + ik \sin \theta \right), \quad (3.6)$$

where  $C(k)$  is known as Theodorsen's function, which is the ratio of modified Bessel functions of the second kind of order zero and order one, and  $\theta$  is the polar angle in the transformed circle plane obtained using the Joukowski transformation, see Fung (1955) (section 2.2). In figures 3.18(a) and 3.18(b) the results of the classical linearised potential flow theory of Theodorsen are shown by the dotted line and the experimental results for the NACA0018 airfoil are shown by the solid line with solid circular markers. The experiments are corrected for the streamwise dependence of the acoustic field (af.) and the contribution of the pressure gradient (pg.) due to the oscillating flow has been subtracted. The correction for the time dependent pressure gradient has been modelled as if the acoustic field were uniform in streamwise direction, using the value of  $v'$  estimated at  $x = 0.5$  m.

### 3.5.5 Dependency of $\Delta C_{pu}$ on excitation amplitude

One of the advantages of the new measurement technique is that the amplitude can be controlled very accurately within a large dynamical range. The results for different forcing amplitudes ( $v'/U_\infty$ ) are shown in figures 3.19(a) and 3.19(b) for the range  $10^{-4} \leq v'/U_\infty \leq 10^{-1}$ . The data shown is corrected for the  $x$ -dependency of the acoustic field, as described in section 3.5.3 and is also corrected for the pressure gradient which is present due to the oscillating transversal flow. Figure 3.19(a) shows that there is

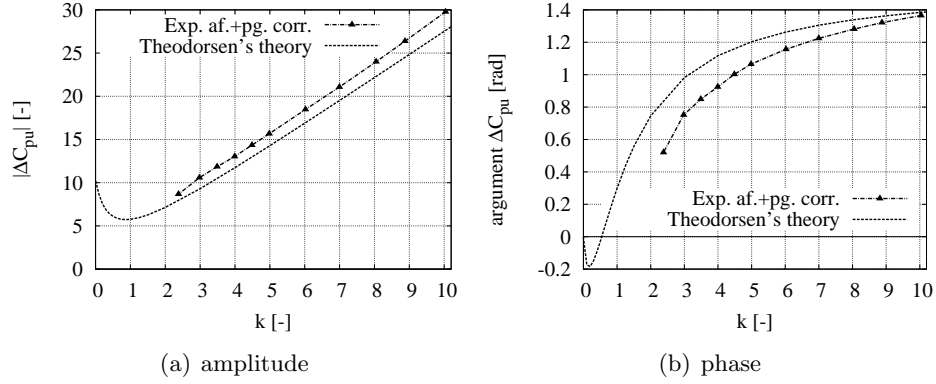


**Figure 3.18** – Amplitude (a) and phase (b) of non-dimensional dynamical pressure difference over a NACA0018 airfoil corrected for the streamwise dependence of the acoustic field (af.) and corrected for the presence of a time dependent pressure gradient (pg.), for excitation amplitudes in the range  $1.4 \cdot 10^{-2} < v'/U_\infty < 9.7 \cdot 10^{-2}$  and  $1.9 \cdot 10^5 < Re_c < 7.9 \cdot 10^5$ . Also shown by the dotted line is the result of classical linearised potential theory for a plunging flat plate. The phase is determined with respect to the velocity fluctuation  $v'$ , which is corrected for the  $x$ -dependency of the acoustic field.

very little dependence of the amplitude of  $\Delta C_{pu}$  on the forcing amplitude  $v'/U_\infty$ . There is, however, an influence of the forcing amplitude on the phase. At higher forcing amplitudes the phase shifts upwards, while the shape of the phase dependence remains the same. It also appears that all the curves collapse below  $k = 3$ . This amplitude dependence of the phase cannot be understood by potential flow theory and its origin remains an open question.

### 3.6 Conclusion

In this chapter the acoustic properties of a test section in an anechoic chamber and detached or attached to the wind tunnel were investigated at the resonance frequency. As an application, acoustic excitation of the first transversal eigenfrequency of the test section as part of the wind tunnel was used to simulate the plunging motion of a NACA0018 airfoil. This method can also be applied to other objects besides airfoils, as long as the size of the object is small compared to the acoustic wave length corresponding to the resonance frequency. We have only presented local pressure measurements, it is possible, however, to use this forcing method in combination with

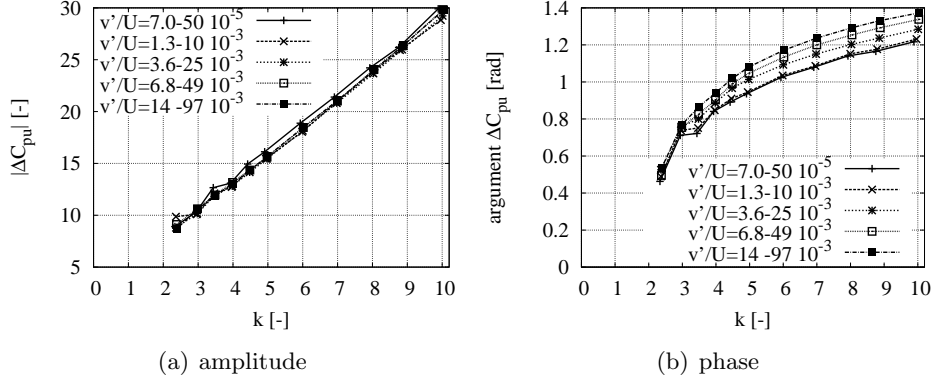


**Figure 3.19** – Amplitude (a) and phase (b) of non-dimensional dynamical pressure difference over NACA0018 airfoil and corresponding phase for different excitation amplitudes  $v'/U_\infty$  and  $1.9 \cdot 10^5 < Re_c < 7.9 \cdot 10^5$ . The phase is determined with respect to the velocity fluctuations  $v'$ , which is corrected for the  $x$ -dependency of the acoustic field.

other experimental measurement techniques like PIV, LDA, hotwire or force balance measurement. In our current setup optical access was blocked by the loudspeakers, but these speakers could also be placed in a different configuration to allow optical access. One could for example replace the large loudspeakers by a set of smaller ones.

The IBEM method was capable of reasonably well predicting the resonance frequencies of the different geometries. Even though the energy losses were not predicted/modelled correctly, the spatial distribution of the acoustic pressure inside the test section was predicted well, all at the resonance frequency. The wing inside the test section can, for the acoustic field, be modelled by a flat plate. This predicts the drop in resonance frequency due to the placement of the wing. However, the numerical method of the test section with the wing installed predicts a resonance frequency which is about 5 Hz higher than the measured resonance frequency.

Numerical simulations and experimental measurements show that the spatial distribution of the acoustic field normal to the flow (in  $y$ -direction) can be modelled by half a cosine with an accuracy better than 5%. This model of a half cosine dependence of the acoustic pressure in  $y$ -direction can be used to estimate the acoustic velocity in the centre of the test section.

Even though the chord of the wing is small compared to both the width of the test section and to the acoustic wave length, there is a significant drop in resonance frequency when the wing is installed. The acoustic field

has a more local distribution with wing present than without wing.

Acoustically seen the test section behaves as a finite duct with open ends rather than an infinite duct. The acoustic field is essentially two-dimensional. The reasonable agreement of the observed resonance frequency, of the test section with wing, with the cut-off frequency  $f_c = c/2L$  of the duct, is a coincidence due to a lowering of the resonance frequency by the presence of the wing, which compensates the effect of the finite duct length.

As an application an alternative experimental method for performing unsteady flow measurements on an airfoil in a wind tunnel has been presented. The results of these measurements agree well with numerical simulations based on Euler's equations both in a steady and an unsteady flow. The range of reduced frequencies this experimental method is capable of, is determined by three parameters, namely the size of the airfoil, the geometry and dimensions of the wind tunnel, and the maximum velocity of the wind tunnel.

The weak point of the proposed method is that due to the strong localisation of the acoustic field it is not possible to translate exactly the acoustical excitation into a pure plunging motion of the wing. A procedure has been proposed to obtain an estimate for the equivalent plunging velocity amplitude. In spite of this limitation, the method certainly provides an efficient mean of exploration of the relative influence of a cavity (or other devices) on the dynamical response of a wing or other object. We can reach high values of the reduced frequency that are difficult to obtain otherwise. Furthermore, a strong point of the method is that the excitation amplitude can easily be varied from extremely low amplitudes ( $v'/U_\infty = O(10^{-4})$ ) up to  $v'/U_\infty = O(10^{-1})$ .

## Chapter 4

# Numerical simulation of flow without forcing\*

Numerical results for a standard airfoil without cavity have been presented in the previous chapters. In this chapter we will focus on numerical simulations of the flow around an airfoil with a cavity, but without external forcing. In Chapter 6 of this thesis the results with external forcing will be discussed.

First a brief introduction is given in section 4.1. In section 4.2 solutions of the Euler equations are discussed. Then in section 4.3 a description of a numerical method based on the Navier–Stokes equations is presented. Section 4.5 presents numerical and experimental results obtained for a standard airfoil without cavity which are compared to results available in the literature. In the last part of section 4.5 the numerical results for the airfoil with cavity are discussed and compared to experimental results. Conclusions are drawn in section 4.6.

### 4.1 Introduction

Theoretical studies have shown that airfoils with trapped vortices can have favourable properties, such as a high lift to drag ratio, or prevention of periodic vortex shedding at high angles of attack. It was recently shown that in a potential flow with two trapped vortices a non-zero-volume body with lift exists, with a favourable pressure gradient along the entire contour

---

\*The contents of this chapter has been submitted to a scientific journal for publication.



of the body, see Chernyshenko *et al.* (2003). A favourable pressure gradient is beneficial because it prevents flow separation.

Construction of a solution of the flow past an airfoil with cavity containing a trapped vortex is provided by Bunyakin *et al.* (1996, 1998). In both papers the flow is a Batchelor-model type of flow. This means that the flow is steady, two-dimensional and that vorticity is uniform inside the regions of closed streamlines and zero outside, corresponding to the limiting case of flow at high Reynolds number.

Previous studies on cavity flows report about a shear layer instability mode and a cavity wake mode. In the literature, cavities can be classified as either deep or shallow, depending on the ratio of cavity depth  $D$  to cavity opening  $W$ . Furthermore one distinguishes between very shallow cavities that are open and closed, depending on whether reattachment of the flow takes place on the bottom wall within the cavity (open cavity) or not (closed cavity). For the cavity considered in this chapter  $D/W = O(1)$  which corresponds to an open, shallow cavity.

Because of the approximations made in the theory for designing a wing with cavity some of the features of a cavity are omitted, such as the oscillations of the shear layer. The oscillations of the shear layer above the cavity might have a considerable effect on the aerodynamic characteristics of the airfoil in steady as well as in unsteady flow. In the case for which the opening of the cavity is a significant portion of the chord length of the airfoil, the oscillations of the shear layer might interfere with the shedding of vorticity at the trailing edge. In the current chapter we will focus on the aerodynamics of the airfoil in a steady uniform free stream.

The available theoretical studies mainly focus on approximate theory (inviscid or Batchelor-model type of flow) in order to simplify the analysis. In this chapter we attempt to gain more insight into the flow physics by means of numerical simulations for two-dimensional flow. It will be shown that solutions of the Euler equations yield unphysical results and we therefore choose to perform numerical simulation of the incompressible Navier–Stokes equations for two-dimensional viscous flow (2D NS). Because of the separated flow and instabilities, Reynolds Averaged Navier–Stokes computations are not expected to correctly predict the flow. A LES simulation for three-dimensional flow is expected to capture the flow physics but would be very time-consuming. Therefore we decided to carry out a preliminary, more feasible, numerical study using a method for 2D NS simulation.

In this chapter we will study the flow around a geometry that was

designed for quick manufacture at low cost. We compare wind tunnel data with numerical results. This geometry is therefore similar but different from the one shown in the introduction of this thesis, which would be more time-consuming and expensive to manufacture.

## 4.2 Numerical method based on Euler equations

In the preceding chapter we have used an Euler method, which yields good results. We therefore apply this method here for the case of an airfoil with cavity. The numerical method for the Euler equations used here is the same as that used in Chapter 2 and Chapter 3 and this is also the code that was used by Dequand (2000).

For cavity flows several successful applications of solutions of the Euler equations have been reported in the literature, see Dequand (2000); Lafon *et al.* (2003). There are also many studies on cavity flows based on Navier–Stokes solutions. In Brès & Colonius (2008) the results of compressible direct numerical simulation of flows over open cavities are presented. Large-eddy simulations of cavity flows can be found in Larchevêque *et al.* (2007).

The benefit of using a method based on the Euler equations is the significantly lower computational power required compared to methods that solve the Navier–Stokes equations. Although inviscid flow method, like the ones based on the Euler equations cannot predict flow separation from a smooth surface, the numerical dissipation of the solution method will usually results in flow separation at sharp corners.

In general the dynamics of the shear layer in an Euler solution will be determined by the artificial dissipation of the numerical method. In reality the shear layer dynamics is controlled by the viscosity of the fluid. For this reason one cannot expect a priori that the shear layer dynamics computed by solving the Euler equations, to be physically accurate. As explained by Lafon *et al.* (2003) a more physical behaviour can be achieved when the boundary layer velocity profile is imposed just upstream of the separation point. In our case this is not possible. In case of our airfoil with cavity and with acoustic forcing (as presented in Chapter 3), the acoustic forcing might force the shear layer dynamics. When the shear layer responds to the acoustic forcing and synchronizes to the frequency of this forcing, application of the Euler equations is expected to be justified.

The benefit of application of the Euler equations is that we can model part of the wind tunnel and speakers and let the acoustic field develop. For

an airfoil without cavity this approach was successful, as was demonstrated in Chapter 3. We therefore also used this Euler method to compute the flow around the airfoil with a cavity. The geometry of this airfoil is shown in figure 4.5 and details can be found in appendix A. The computational mesh consists of a structured grid of 25 blocks. In figure 4.1 a coarse version of the grid is shown. The grid is very similar to the grid that was used for the airfoil without cavity in Chapter 3. The present grid has also two singular points upstream of the airfoil. In addition there are two more singular points inside the cavity, due to the embedded C-grid necessary to mesh the interior of the cavity. In this specific case we used the explicit time stepping scheme. The total number of cells in the grid that is used in the computation is

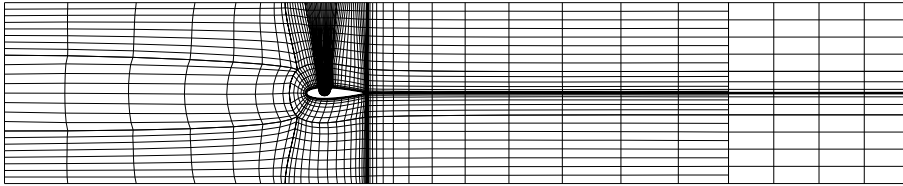


**Figure 4.1** – NACA0018 airfoil with cavity *A* at  $0^\circ$  angle of attack. Coarse version of the computational mesh with two singular points upstream of the airfoil and two singular points inside the cavity.

39200, with 200 cells inside the cavity opening. The grid is extra refined in the region of the shear layer and inside the cavity. A close-up of this region of the grid is given in figure 4.2.

In these Euler computations we found that initially a shear layer develops, which is unstable and rolls up into concentrated vortices, this is indicated in figure 4.3(a). However, as the computation progresses the flow inside the cavity is accelerated by the shear layer (and injected vorticity) and the velocity gradient over the shear layer vanishes, resulting in a stable shear layer, as shown in figure 4.3(b). Note that the cavity geometry we use here is different from the geometry considered in the Vortexcell2050 project. For the specific case shown in figures 4.3(a) and 4.3(a),  $\alpha = 12^\circ$  and  $M = 0.2$ . The boundary conditions are anechoic at the in and outflow and no acoustic forcing is applied.

For different values of the angle of attack and for the cases with and without acoustic forcing, all solutions tend to this stable flow solution in which the flow separates at the forward sharp edge of the cavity and reattaches at the rear sharp corner of the cavity, and there is a single large clockwise rotating vortex inside the cavity. The solution that is obtained

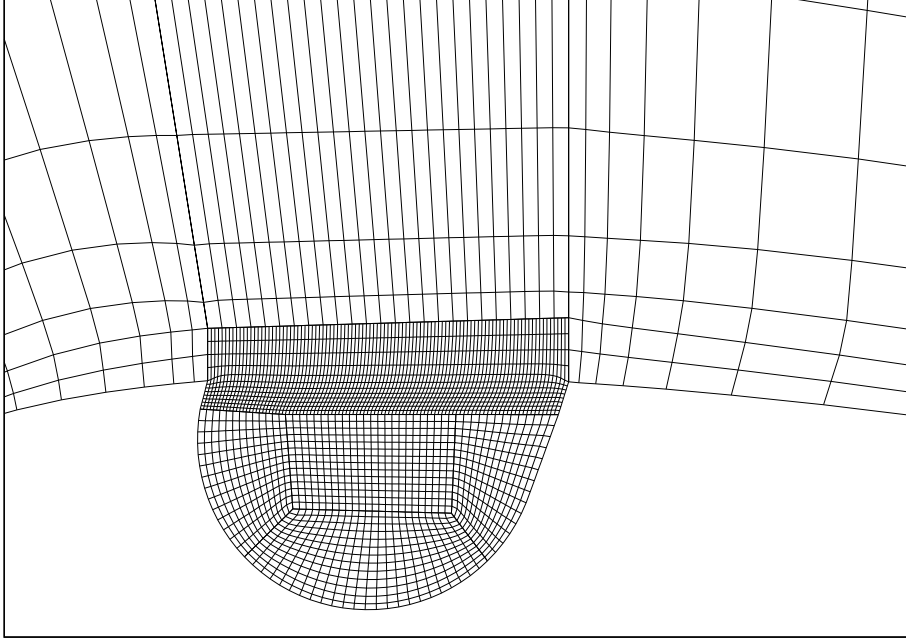


**Figure 4.2** – Close-up of the coarse computational grid inside and in the vicinity of the cavity. The two singular points inside the cavity are visible near the center of the cavity.

appears to have similarities with Batchelor flow. A Batchelor flow is a two-dimensional, steady and incompressible flow, in the limit of infinite time and infinite Reynolds number, in which the vorticity is uniform inside the region of closed streamlines. In the present case the vorticity inside this closed region (in this case inside the cavity) is determined by numerical dissipation (Prandtl–Batchelor theorem). For more information about Batchelor flow and the Prandtl–Batchelor theorem the reader is referred to Batchelor (1956*a, b*). The trapped vortex inside the cavity causes a low pressure along the cavity wall, even lower than the pressure just upstream of the cavity. This is in disagreement with the experimental observation that the pressure in the cavity is higher than the pressure just upstream of the cavity at high positive angles of attack (this is shown in section 4.5.2). A plot of the pressure coefficient  $C_p = \frac{2(p-p_\infty)}{\rho U_\infty^2}$  is shown in figure 4.4 for the stable solution. Also measurements of the local flow velocity, presented in Chapter 6, indicate that the flow in the cavity is unsteady and far from Batchelor flow. This is further confirmed by the flow visualisations discussed in Chapter 5.

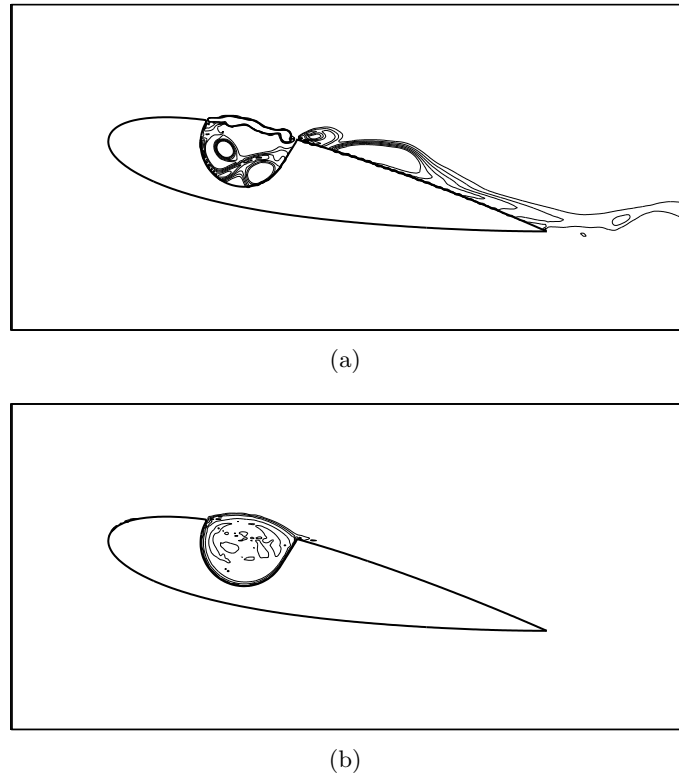


**Figure 4.3** – Results of a computation using the Euler equations for the airfoil with a cavity at  $12^\circ$  angle of attack,  $M_\infty = 0.2$ . Vorticity contours indicating an unstable shear layer initially (a) and a stable vortex inside the cavity with a stable shear layer after some time (b). The contour level are in the range  $-8.3 < \frac{\omega c}{c_0} < -1.7$ .

The numerical solution is therefore unphysical and from this we conclude that for this specific case the Euler equations are not suitable and influence of the no-slip boundary condition is essential inside the cavity. We also computed the solution with the cavity placed in a plane wall, and this yielded the same stable solution with one large vortex inside the cavity. The problem is therefore not due to the fact that we consider a cavity in an airfoil. We also verified that the results are grid independent. If the grid is further refined the initial shear layer is more unstable and it takes longer to reach the state with uniform vorticity in the cavity.

In reality the flow inside the cavity is determined by a balance between the shear layer driving the flow at the upper part of the cavity and the

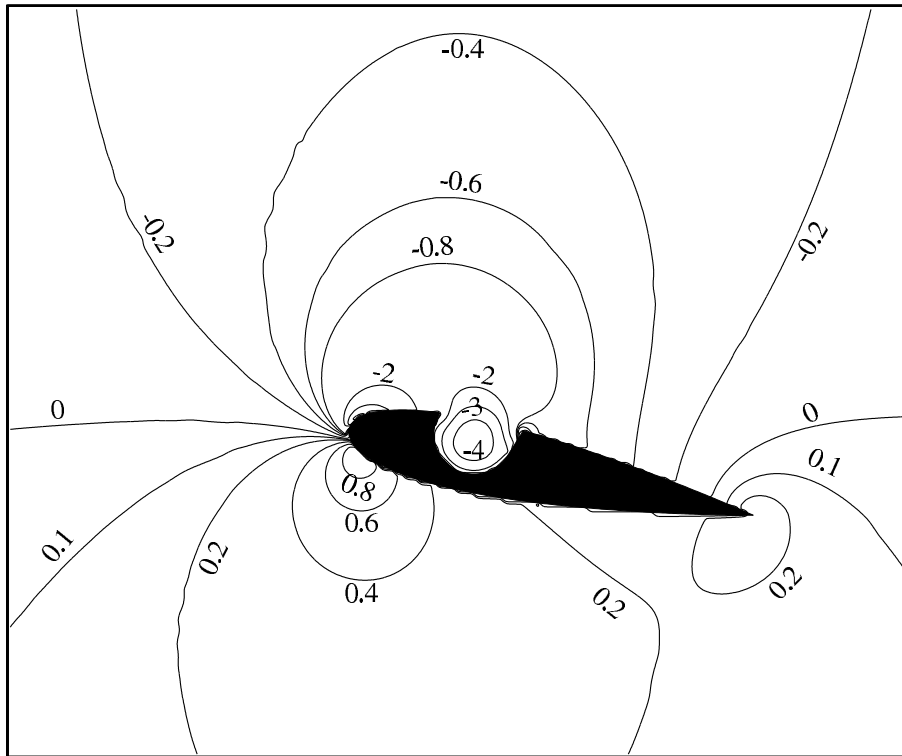


**Figure 4.4** – Contour plot of the pressure coefficient  $C_p$  for  $\alpha = 12^\circ$  and  $M_\infty = 0.2$ .

dissipation inside the cavity due to viscosity at the side and bottom walls. In the numerical simulations presented in this chapter we will see that at low Reynolds number the boundary layer inside the cavity separates and that there are in general two vortices of opposite sign in the cavity, rather than one large vortex, as predicted by the Euler solutions.

We also made an attempt to obtain a solution using the vortex-blob method. Inviscid vortex blob methods suffer from the same shortcomings as Euler solutions. Here the blobs are collected inside the cavity with two possibilities: the solution is stable and similar to the Euler solution or all blobs are ejected from the cavity suddenly after which the buildup of vorticity in the cavity starts again, as in a cavity wake mode (figure 1.4(c)). Again this flow solution does not agree with experimental observations.

### 4.3 Numerical method based on Navier–Stokes

In the preceding section we have seen that for the present cavity flow the Euler equations yield unphysical results. Effects of viscosity are important to obtain a realistic flow inside the cavity. We therefore solve the Navier–Stokes equations. The Navier–Stokes equations for two-dimensional incompressible flow are solved using an immersed boundary (IB) projection method described by Taira & Colonius (2007); Colonius & Taira (2008). The solid body of the airfoil is represented, on a regular Cartesian grid, by a set of discrete forces that are in turn regularised (smeared) on the grid. At these discrete body points, the no-slip condition is exactly enforced. The equations are discretised with a second-order finite-volume method and a streamfunction-vorticity formulation is used in a staggered grid arrangement. Due to the streamfunction formulation the divergence-free constraint of the velocity field is exactly satisfied (to machine precision). The immersed boundary treatment gives rise to a first-order error in the momentum equations near the surface of the body; empirical convergence studies presented in Taira & Colonius (2007) show better than first-order accuracy in the L2 norm. Further details regarding the numerical method can be found in the aforementioned references.

Numerical simulation have been performed for several angles of attack  $\alpha$ , in degrees. The angle of attack is defined positive as indicated in figure 4.5. The NACA0018 airfoil is described by 2779 points at which the no-slip condition is enforced. For the airfoil with cavity this is 2995 points. The parameters of the calculations for positive angles of attack are listed in table II. For the airfoil with cavity, the same cases as listed in table II are also run at the same negative angles of attack, with the same set of parameters as used for the corresponding positive angles. The computational domain typically extends to a distance of twelve chord lengths in the upstream and downstream directions and three chord lengths in the upper and lower normal directions.

Furthermore we use free-slip boundary conditions at the boundary of the computational domain. For the airfoil without cavity, for an angle of attack of  $0^\circ$  this yields a magnitude of the velocity at the boundary of the computational domain above and below the airfoil which is about 1.5% higher than the free stream velocity. For an angle of attack of  $4^\circ$  the magnitude of the velocity on the boundary of the computation domain above the airfoil is about 3.5% higher than the free stream velocity.

This IB method uses a series of overlapping, consecutively larger and

angle of attack (degrees)	smallest box size	largest box size	grid levels	total number of cells
0.0	$1.49 \times 0.328$	$23.9 \times 5.25$	5	$4.4 \cdot 10^6$
1.0	$1.49 \times 0.328$	$23.9 \times 5.25$	5	$4.4 \cdot 10^6$
2.0	$1.49 \times 0.328$	$23.9 \times 5.25$	5	$4.4 \cdot 10^6$
3.0	$1.49 \times 0.358$	$23.9 \times 5.73$	5	$4.8 \cdot 10^6$
4.0	$1.49 \times 0.358$	$23.9 \times 5.73$	5	$4.8 \cdot 10^6$
6.0	$1.49 \times 0.358$	$23.9 \times 5.73$	5	$4.8 \cdot 10^6$
10.0	$1.49 \times 0.358$	$23.9 \times 5.73$	5	$4.8 \cdot 10^6$
15.0	$1.49 \times 0.433$	$47.8 \times 13.9$	6	$6.96 \cdot 10^6$

**Table II** – Setting for NACA0018 cases with and without cavity. Box sizes are indicated in terms of chord lengths.

coarser grids; the number of grids is listed in table II as grid levels. The smallest domain with finest resolution extends to 1.5 chord lengths in the streamwise and 0.35 chord lengths in the normal directions. The non-dimensional grid spacing,  $\frac{\Delta}{c}$ , on this finest grid is  $7.4 \cdot 10^{-4}$  for the majority of cases studied. Selected cases are run on a coarser grid with  $\frac{\Delta}{c} = 1.1 \cdot 10^{-3}$  to test grid convergence. The flow around NACA0018 airfoil is computed for four angles of attack:  $0^\circ$ ,  $4^\circ$ ,  $10^\circ$  and  $15^\circ$ . The computational settings are the same as those listed for the airfoil with cavity.

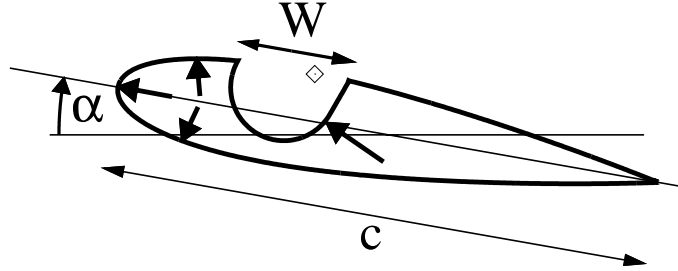


**Figure 4.5** – NACA0018 airfoil with cavity, with chord length  $c = 165$  mm and cavity opening  $W = 34$  mm. Pressure transducers are mounted at the locations indicated by the arrows. A probe location in the shear layer, used in the numerical simulations, is shown by the diamond.

In the IB method, the discrete points at which the no-slip condition is enforced cannot be too close to each other. Typically the distance between those points needs to be equal to or slightly greater than the grid spacing. Note that if the distance between the points is too large then the surface is porous. At the sharp trailing edge, points of the upper surface may be too



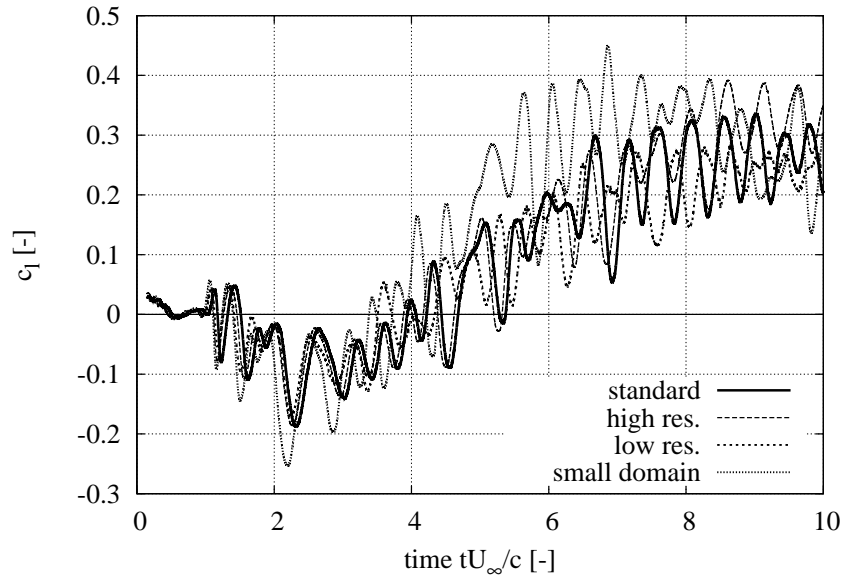


**Figure 4.6** – Lift coefficient as a function of non-dimensional time for different resolutions and domain sizes.

close to points on the lower surface. This issue is dealt with by omitting a few points on either the upper or lower surface. The NACA0018 airfoil without cavity at zero angle of attack is also computed with a rounded trailing edge without omitting points. The trailing edge radius is 0.3% of the chord length, which is the same as that of the airfoil used in the experiment. The rounded trailing edge is described by approximately 10 points.

For the case of  $\alpha = 0^\circ$  the grid resolution and domain size were varied in order to assess convergence of the flow solution and influence of the far-field boundary on the solution. For  $\alpha = 0^\circ$  the lift coefficient is shown in figure 4.6 for runs with different settings. The case “standard” indicates the run with the settings as given in table II. The results of a runs with the same size of the computational domain as the standard run, but with a resolution 1.5 times higher than the standard run are shown as “high res.”. The case “low res.” also has the same size of the computational domain as the standard run, but now the resolution is 1.5 times lower compared to the standard run. Lastly, “small domain” indicates a run with the same resolution as the standard run, but with a computational domain which contain 3 levels, with the largest box size equal to  $6 \times 1.3$  chord lengths. From the results shown in figure 4.6 one can conclude that the results presented, with the resolutions and domain sizes listed in table II are essentially grid inde-

pendent. It should be noted that the flows considered show signs of chaotic behaviour in vortex shedding. The Reynolds number is sufficiently high such that the formation of large-scale vortices, and the subsequent pairing of these structures gives rise to aperiodic, low-frequency oscillations. This feature is difficult to characterise because the run times were not sufficiently long to observe many periods. Thus two cases at slightly different resolution ultimately become de-correlated from each other, and contain oscillations over sufficiently long times such that it is not possible to distinguish any possible contamination from the far-field boundaries. However, in all cases we observed that the time-averaged quantities and qualitative flow regimes are indeed grid independent.

## 4.4 Experimental facility

The experimental facility is a closed-loop, low-speed wind tunnel (located at Eindhoven University of Technology) with a square test section of 500 mm  $\times$  500 mm and a length of 1000 mm from the end of the contraction to the beginning of the diffuser. The walls of the test section are manufactured from plywood with a wall thickness of 24 mm. Between the test section and the diffuser a slit of about 2 cm causes the pressure inside the test section to be nearly equal to the atmospheric pressure. It has practical advantages to prevent a very low pressure in the test section, which would result without the slit. The maximum velocity in the test section is about 67 m/s, which corresponds to a Mach number of 0.19 at room temperature. The velocity is determined by measuring the pressure difference between the settling chamber and the test section with a manometer, assuming the velocity is zero inside the settling chamber. The turbulence intensity inside the empty test section was measured with a hotwire and was found to be less than 0.2%.

An airfoil can be mounted vertically between the upper and lower wall of the test section. The bottom of the airfoil is fixed to the test section by a pin-in-hole construction, while the upper side of the airfoil is connected by a tube in a flange, which is bolted to the test section. The angle of attack can be varied with an accuracy of about 0.5 degrees.

The airfoils used are NACA0018 profiles. This is a relatively thick profile which is reasonably well known. The profiles are manufactured by aluminium extrusion and approximate the NACA0018 profile definition within 0.2%. Both a clean profile and a profile with cavity are considered. The

chord length  $c$  of the profiles is 165 mm and the span is 495 mm such that the airfoils fit tightly at the tips to the ends at the test section walls. At an angle of attack of zero degrees the blockage in the test section is 2%.

The airfoil with cavity is a NACA0018 airfoil with a cavity milled in the upper surface over 95% of the span of the airfoil, the cross section of this airfoil is shown in figure 4.5. The opening of the cavity  $W$  is 34 mm. Both edges of the cavity are sharp. The forward sharp edge will fix the flow separation point and the rear sharp edge will maximise the feedback loop of the shear layer. This configuration is expected to give the most extreme oscillations of the shear layer.

In the airfoils several miniature dynamic pressure transducers (Kulite XCS-093-140mBarD) are mounted flush to the surface: one at the leading edge, one on either side of the airfoil at 13.3% chord length from the leading edge, and for the airfoil with cavity an additional pressure transducer mounted inside the cavity. The locations are indicated in figure 4.5 by the arrows. The airfoil is constructed such that the reference tubes of the pressure transducers are in connection with the ambient air outside the test section. This will ensure a well defined reference pressure. In the experiments the value of the Reynolds number, based on chord length,  $Re_c = U_\infty c / \nu$ , with  $\nu$  the kinematic viscosity of the air, typically varies between  $2 \cdot 10^5 < Re_c < 8 \cdot 10^5$ .

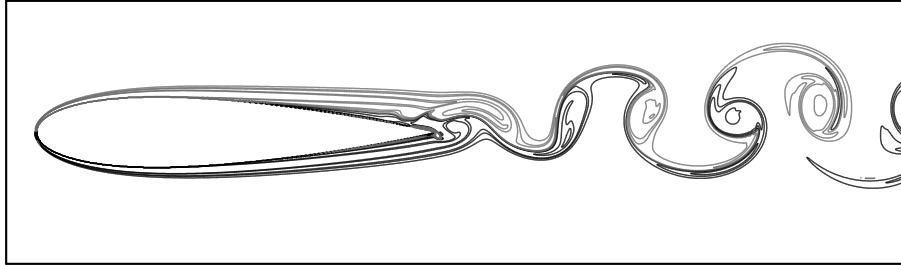
The signals from the pressure transducers are recorded with a National Instruments data acquisition system (NI SCXI-100).

## 4.5 Results

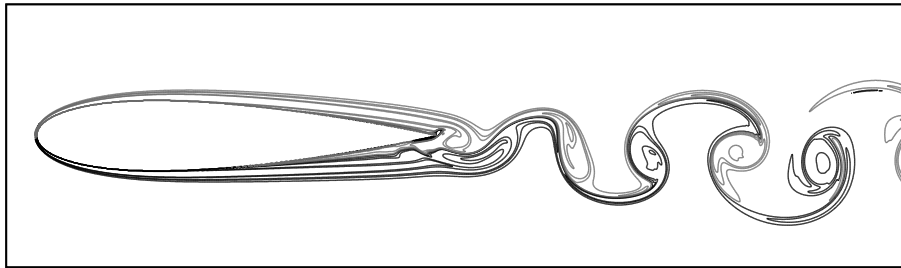
In the following sections the results of the computations will be presented and compared to experimental data. First the results for the NACA0018 airfoil are presented, then the results for the NACA0018 airfoil with cavity are discussed and compared to the NACA0018 airfoil and experimental data. In all the numerical simulations presented  $Re_c = 2.01 \cdot 10^4$ .

### 4.5.1 NACA0018

In this section the results of numerical simulation of a clean airfoil are presented. At  $\alpha = 0^\circ$  the laminar boundary layer separates around 50% of the chord length. Nakano *et al.* (2006) report separation at 51% of the chord length from the leading edge at  $Re_c = 1.6 \cdot 10^5$ . This separation causes a periodic vortex shedding in the wake of the airfoil. The Strouhal



(a) At minimum lift force.



(b) At maximum lift force.

**Figure 4.7** – Vorticity contour plots for the clean airfoil for  $\alpha = 0^\circ$  and  $Re_c = 2.01 \cdot 10^4$  at minimum and maximum lift. Negative vorticity is gray, positive black. The contour levels are in the range  $-35 < \frac{\omega c}{U_\infty} < 35$ .

number based on the projected frontal area of the airfoil  $h$  is defined as  $St_h = fh/U_\infty$ . At  $\alpha = 0^\circ$   $h$  is equal to the thickness of the airfoil and  $St_h = 0.42$ . As the flow develops, the periodic shedding is modulated by a much lower frequency oscillation. The upper and lower surface separation points begin to oscillate upstream and downstream with opposite phase on the upper and lower surfaces. The entire wake is shifted up and down during this low frequency cycle while its structure is unchanged. Snapshots of the vorticity contours are shown at minimum and maximum lift in figures 4.7(a) and 4.7(b), respectively. The Strouhal number  $St_h$  of this low frequency oscillation is about  $1.0 \cdot 10^{-2}$  and the amplitude of the lift force caused by this low frequency oscillation is much larger than the oscillations due to the periodic vortex shedding. Additional calculations have shown that a lower curvature of the trailing edge causes the amplitude of the low frequency oscillation to decrease, but does not eliminate it. At  $\alpha = 0.5^\circ$  the low frequency oscillation is also present. A calculation at  $Re_c = 10^4$  did not display the low frequency oscillation. The low frequency behaviour is most

likely caused by a unique combination of Reynolds number and geometry. It is likely that this low frequency behaviour is very sensitive to three-dimensional effects and turbulence, which could be a reason why it may not be present in wind tunnel experiments. There is however, evidence of similar behaviour in literature provided by Zaman *et al.* (1989), but this was reported for airfoils near stall conditions.

At  $\alpha = 4^\circ$  the separation point on the suction side moves upstream to about 25% chord length from the leading edge and to 75% chord on the pressure side. Literature on the measurement of the location of the separation point on a NACA0018, at a Reynolds number of  $Re_c = 1.6 \cdot 10^5$  shows that at  $\alpha = 3^\circ$  the point of separation on the suction and pressure side is at 37% and 61% chord length from the leading edge, respectively, see Nakano *et al.* (2006). The separated boundary layer on the suction side rolls up into large scale vortices which are periodically shed downstream. The Strouhal number  $St_h$  of this periodic vortex shedding is 0.22.

At  $\alpha = 10^\circ$  and  $\alpha = 15^\circ$  the flow is similar to the flow at  $\alpha = 4^\circ$ . Only the separation bubble and the vortex structures shed downstream are larger and the separation point on the suction side moves upstream with increasing angle of attack. Also the vortices formed from the separating boundary layer tend to merge into larger structures before being shed into the wake. At  $\alpha = 10^\circ$  the Strouhal number  $St_h$  of the wake is approximately 0.2.

In figures 4.8 and 4.9 the time averaged lift and drag coefficient from the numerical simulation of the clean airfoil are compared to experimental data from Jacobs & Sherman (1937), at a Reynolds number of  $4.14 \cdot 10^4$  and more recent experimental data by Timmer (2008) at a Reynolds number of  $1.5 \cdot 10^5$ .

The deviation of the predicted lift coefficient from the experimental data at  $\alpha = 15^\circ$  is caused by the low Reynolds number and enforced two-dimensionality. The massively separated flow will be three-dimensional and turbulent in reality.

The predicted drag coefficient is consistently above the experimental data from literature, although the trend is correct. A probable cause for the high values of the drag coefficient is the low Reynolds number in the numerical simulations. It should also be noted that laminar separation is in general very sensitive, even to small disturbances, such as acoustics or free stream turbulence in wind tunnel measurements.

There is also experimental data available of the local values of the

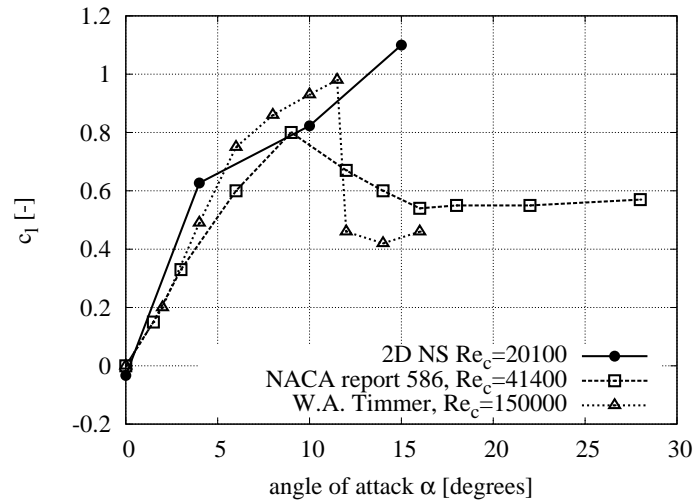


**Figure 4.8** – Time averaged lift coefficient for NACA0018 airfoil as a function of  $\alpha$ . The numerical results at  $Re_c = 2.01 \cdot 10^4$  shown as the solid line with solid circular markers, experimental results from Jacobs & Sherman (1937) at  $Re_c = 4.14 \cdot 10^4$  indicated by the dashed line with open squares and experimental results from Timmer (2008) at  $Re_c = 1.5 \cdot 10^5$  shown by the dashed line with open triangles.

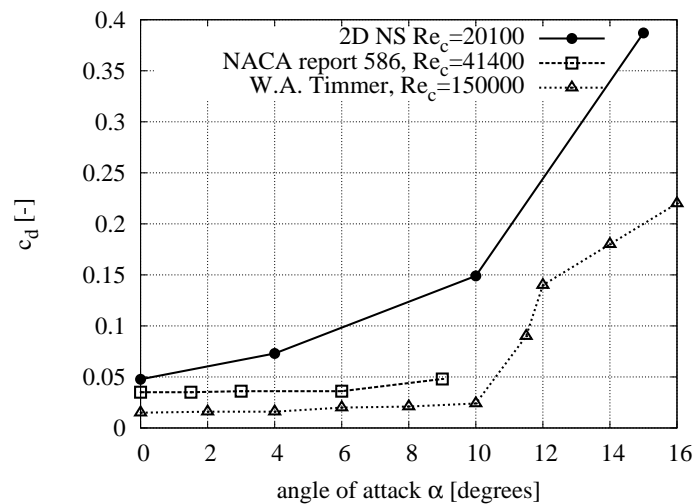


**Figure 4.9** – Time averaged drag coefficient for NACA0018 airfoil as a function of  $\alpha$ . The numerical results at  $Re_c = 2.01 \cdot 10^4$  shown as the solid line with solid circular markers, experimental results from Jacobs & Sherman (1937) at  $Re_c = 4.14 \cdot 10^4$  indicated by the dashed line with open squares and experimental results from Timmer (2008) at  $Re_c = 1.5 \cdot 10^5$  shown by the dashed line with open triangles.

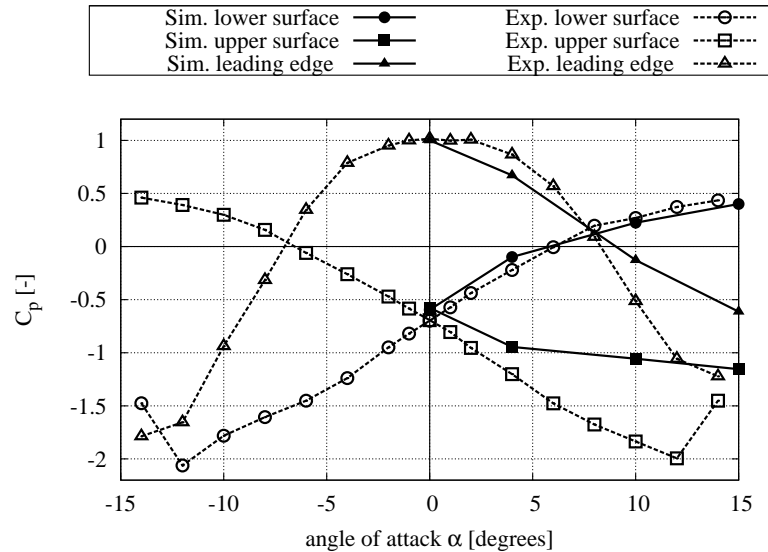


**Figure 4.10** – Time averaged values of the pressure coefficient at different locations, for NACA0018 airfoil as a function of angle of attack. The numerical results, at  $Re_c = 2.01 \cdot 10^4$  are shown as the solid line with solid markers, experimental results  $Re_c = 4.4 \cdot 10^5$  indicated by the dashed lines with open markers.

pressure coefficient  $C_p = \frac{2(p-p_\infty)}{\rho_\infty U_\infty^2}$ , at three locations on the airfoil, these locations are indicated in figure 4.5 by the arrows. Here  $\rho_\infty$  is the free stream density, and  $p$  is the pressure. These experimental data have been obtained in the wind tunnel described in section 4.4 at  $Re_c = 4.4 \cdot 10^5$ . In the immersed boundary method the solution very close to the surface is contaminated by the regularised body forces. Therefore the pressure in the numerical simulations has been probed at a distance of approximately 1.5 cell spacing from the surface. This will still yield accurate values of the pressure at the surface since the pressure across the boundary layer is, in the boundary layer approximation, constant. In figure 4.10 the time-averaged values of these pressure coefficients are plotted as a function of  $\alpha$ . The experimental data is plotted for both positive and negative values of  $\alpha$  and displays the expected symmetry for this symmetric airfoil. The agreement with the numerical data is reasonable. Note that the largest deviations occur at the suction side of the airfoil (the upper surface for positive angles of attack). It is likely that the boundary layer on the suction side is turbulent in the experiment and separation is delayed (with respect to the low Reynolds number simulation). A turbulent boundary layer will cause the

flow to be attached over a longer distance and yields a lower pressure.

A comparison of the time signals of the predicted pressure difference between two points, on the upper and the lower surface at 13.3% chord from the leading edge and the integrated lift force yields two very similar signals, up to an additive and multiplicative constant. This is also true in the case of the airfoil with cavity. This indicates that the behaviour of the local pressure difference near the leading edge is a good indication of the behaviour of the total integrated lift force, in the absence of forcing.

### 4.5.2 NACA0018 with cavity

In order to have self-sustained oscillations of the shear layer above the cavity, the ratio of momentum thickness  $\theta$  of the boundary layer and cavity opening  $W$  should be small, i.e.  $\frac{\theta}{W} \ll 1$ . The main stream velocity used for the calculation of  $\theta$ , from the numerical solution, is the maximum velocity in the boundary layer, which is about 27% higher than the free stream velocity due to wall curvature. For  $\alpha = 0^\circ$   $\frac{\theta}{W} \approx 1.6 \cdot 10^{-2}$ , which is much smaller than the required value of about 0.08, based on linearised stability theory given by Michalke (1965).

The Strouhal number ( $St_W = \frac{fW}{U_\infty}$ ) of the shear layer across the cavity is plotted in figure 4.11 for different values of the angle of attack. The numerical probe location of the vertical velocity is at the rear part of the cavity and is indicated in figure 4.5 with the tilted square. It must be noted that the probe location is the same with respect to the airfoil for all angles of attack. This means that for high positive angles of attack the probe is not actually in the shear layer but rather inside the separation bubble.

From figure 4.11 it appears that there are two main regimes of the flow inside the cavity. For positive angles of attack there are two vortices, of opposite sign, inside the cavity and the shear layer above the cavity weakly interacts with the sharp rear edge of the cavity. In these cases the Strouhal number  $St_W$  based on the cavity opening is of  $O(1)$ . When compared to Rockwell & Naudasher (1978) we conclude that this is the second shear layer mode.

For  $\alpha = 3^\circ$  and higher, the Strouhal number at the probe location decreases sharply, because the cavity is now fully inside the separation bubble and the shear layer is less intense and therefore interacts more weakly with the rear sharp edge of the cavity. In this case, however, the separation bubble behaviour is forced by the shear layer separating from the upstream edge of the cavity. At  $\alpha = 10^\circ$  and higher, the cavity is within the separa-



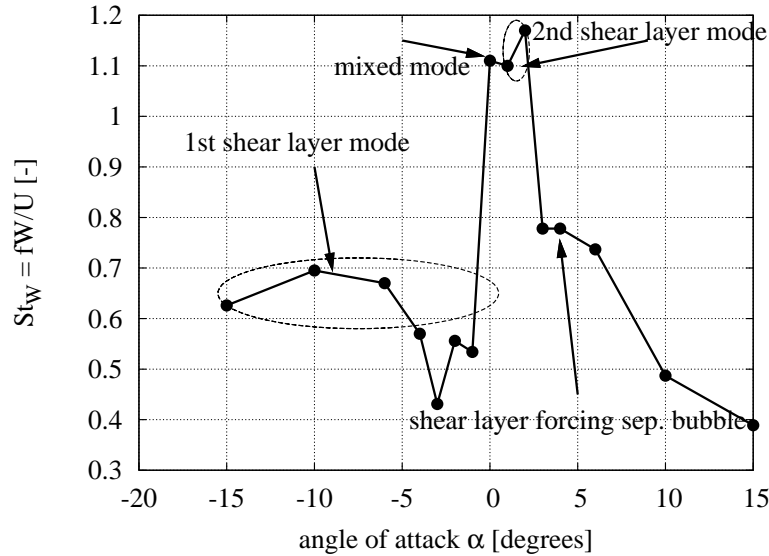


**Figure 4.11** – Predicted values of the Strouhal number  $St_W$  of the shear layer above the cavity for NACA0018 airfoil with cavity as a function of the angle of attack for  $Re_c = 2.01 \cdot 10^4$ .

tion bubble. The cavity has a strong influence on the structure of the flow in the separation bubble. It promotes smaller-scale vortex shedding than would otherwise occur for the airfoil without cavity at the same angle of attack.

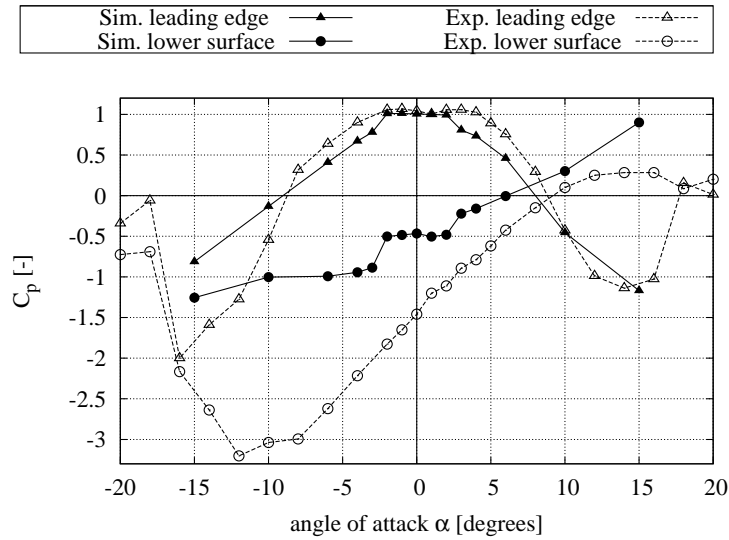
For negative angles of attack the shear layer oscillates violently and vorticity is periodically washed out of the cavity and transported downstream. This appears to be the first shear layer mode. The Strouhal number of the shear layer at these negative angles of attack is approximately 0.5. For more negative angles of attack the Strouhal number increases. This increase can be understood by the flow velocity over the cavity being higher for higher negative angles of attack. The favourable pressure gradient over the cavity at negative angles of attack causes the flow in the cavity to display a first shear layer mode.

The case of  $\alpha = 0^\circ$  displays a mixed behaviour. It starts out as the flow pattern seen for positive angle of attack with a second shear layer mode. Here two main vortices are present inside the cavity and the shear layer oscillates weakly. Gradually the shear layer starts to interact more and more with the sharp rear edge of the cavity and starts to display the more violent first shear layer mode behaviour. After vortex shedding the flow in

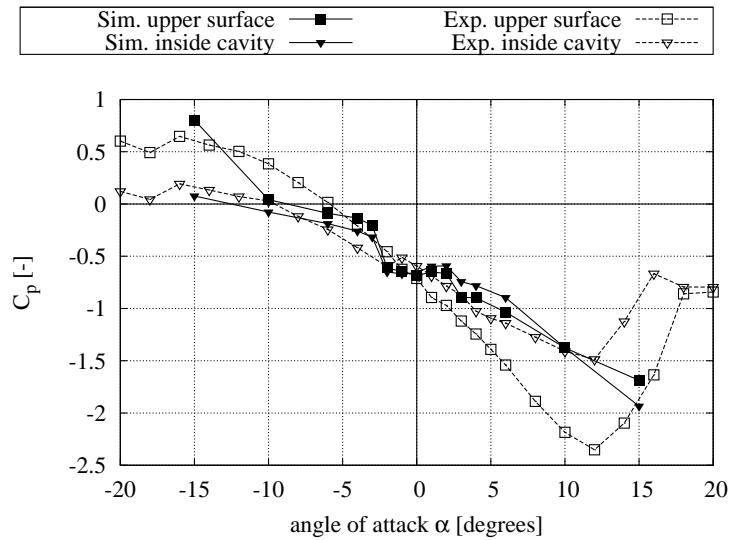
the cavity settles down and displays a flow similar to that observed for the positive angles of attack again. The flow seems to be switching back and forth between a mild second shear layer oscillation to a violent first shear layer oscillation and back again, this switching back and forth appears to continue in time. If one applies freestream flow, which is oscillating in the direction perpendicular to the airfoil (this generates a velocity field around the airfoil which is equivalent to that of a plunging airfoil), with an amplitude of 5% of the main flow and a reduced frequency  $k = \frac{\omega c}{2U_\infty} = 3.0$  the first shear layer mode disappears and only the second shear layer mode is present. For this case the Strouhal number in the shear layer  $St_W$  at the probe location indicated in figure 4.5 is 1.22.

For the airfoil with cavity no data is available from literature. However, there are experimental data on the local pressure coefficient available from the wind tunnel described in section 4.4. The airfoil with cavity is equipped with four pressure transducers, three of which are mounted at the same locations as for the clean NACA0018 airfoil. One additional pressure transducer is mounted inside the cavity. The airfoil and location of the experimental pressure transducers are shown in figure 4.5. In figures 4.12(a) and 4.12(b) the time averaged values of the pressure coefficient are plotted as a function of the angle of attack. The experimental data is shown as the dashed line with open markers and the corresponding numerical data is plotted with solid lines and the same, solid markers. In general the  $C_p$  values predicted by the Navier–Stokes method are higher than the values from the experiment. On the lower surface the higher values of  $C_p$  could be caused by separation that is delayed or eliminated when the boundary layer is turbulent. Also the values predicted on the upper surface for positive angles of attack disagree with the experimental data, which could also be caused by a turbulent (or transitional) boundary layer in the experiment. For positive angles of attack the pressure inside the cavity is higher than the pressure just upstream of the cavity, for negative angles of attack the opposite is true. This is also observed in the numerical data, although the differences in pressure are smaller.

In figure 4.13 the lift coefficient is plotted as a function of the drag coefficient for both the clean airfoil and the airfoil with cavity.



(a) Pressure coefficient at leading edge and lower surface.



(b) Pressure coefficient on upper surface and inside cavity.

**Figure 4.12** – Predicted time averaged values of the pressure coefficient at different locations, compared with measured data for NACA0018 airfoil with cavity as a function of the angle of attack. The numerical results for  $Re_c = 2.01 \cdot 10^4$  are shown as the solid line with solid markers, experimental results for  $Re_c = 4.4 \cdot 10^5$  are indicated by the dashed lines with open markers.

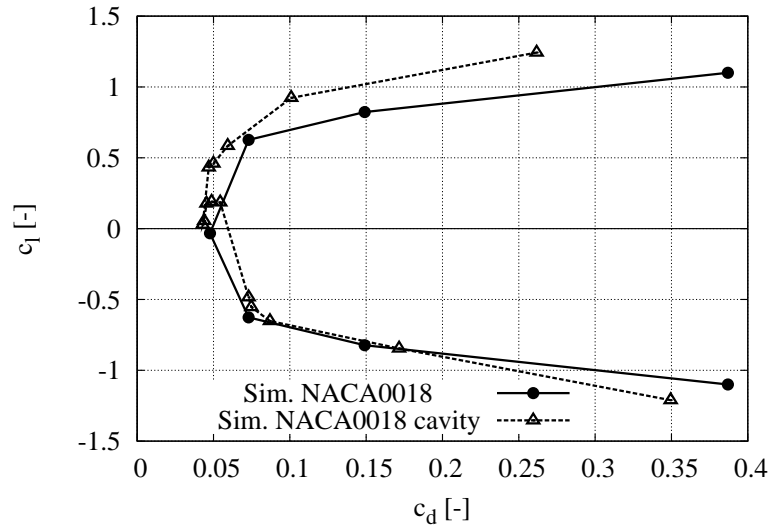


**Figure 4.13** – Lift coefficient as a function of the drag coefficient for the NACA0018 airfoil, solid line with circular marker and for the NACA0018 airfoil with cavity, solid line with triangles. The negative values for the NACA0018 are mirrored points of the positive angles of attack and displayed for easy comparison.

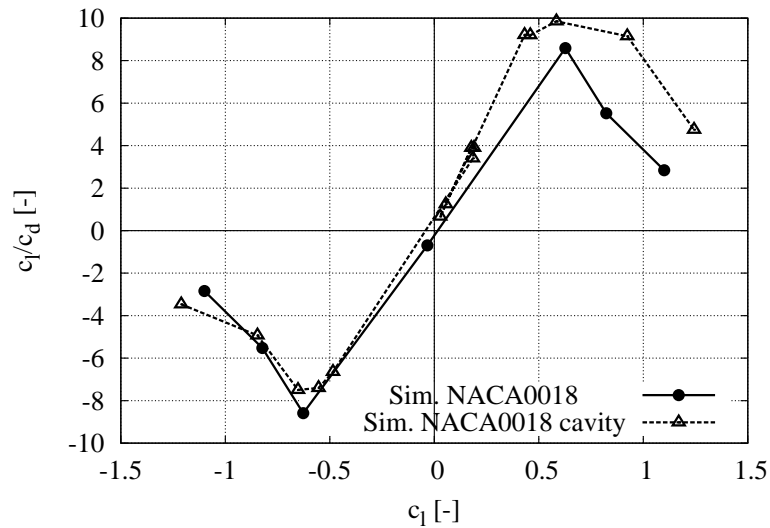
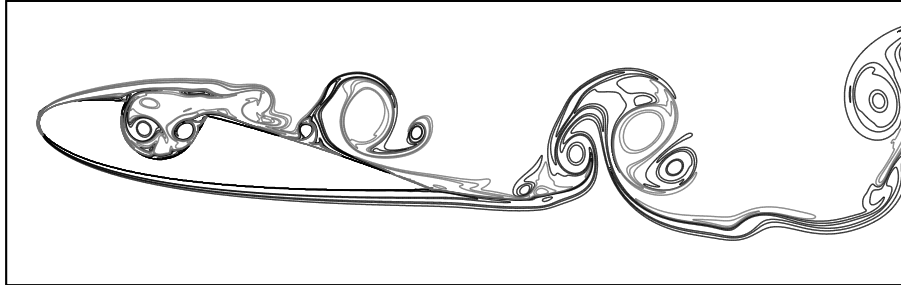
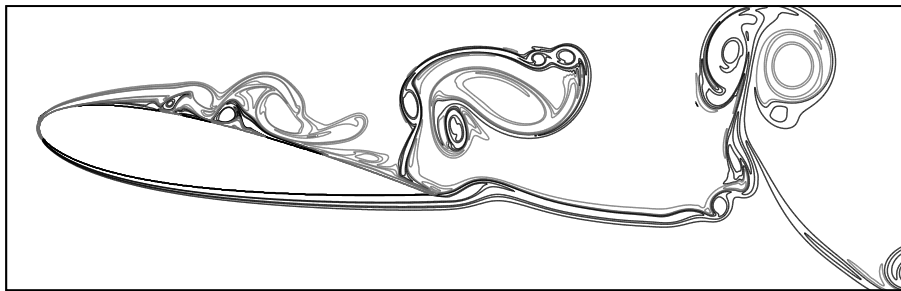


**Figure 4.14** – Lift over drag coefficient ratio as a function of the lift coefficient for NACA0018 airfoil, solid line with solid circular marker and for NACA0018 airfoil with cavity, solid line with triangles. The negative values for NACA0018 are mirrored points of the positive angles of attack and displayed for easy comparison.



(a) Airfoil with cavity.



(b) Airfoil without cavity.

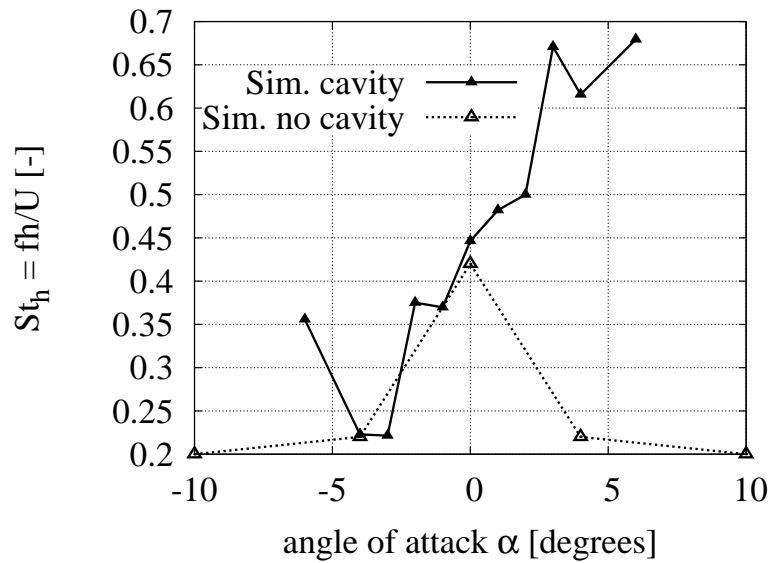
**Figure 4.15** – Vorticity contour plots for the airfoil with and without cavity at  $\alpha = 10^\circ$  and  $Re_c = 2 \cdot 10^4$ . Negative vorticity is gray, positive black. The contour levels are in the range  $-35 < \frac{\omega c}{U_\infty} < 35$ .

Figure 4.13 indicates that at positive angles of attack the airfoil with cavity has a higher lift-to-drag ratio compared to the airfoil without cavity. From the figure it appears that the increased aerodynamic efficiency is mainly due to a decrease in drag, since the curve of the airfoil with cavity is shifted to the left. In figure 4.14 a plot of the lift-to-drag ratio is plotted as a function of the lift coefficient. This figure clearly demonstrates that at high positive lift coefficient the airfoil with cavity has a significantly higher lift-to-drag ratio compared to the clean airfoil. Snapshots of vorticity contours at  $\alpha = 10^\circ$  are shown in figures 4.15(a) and 4.15(b). It suggests that the wake of the airfoil with cavity has smaller vortices and is narrower.

For  $\alpha = 4^\circ$  the Strouhal number  $St_h = 0.22$  for the clean airfoil and  $St_h = 0.68$  for the airfoil with cavity. The frequency was calculated (both for the airfoil with and without cavity) from the spectrum of the pressure at a location near the airfoil surface just downstream of the rear cavity edge.

The interaction of the shear layer with the rear sharp edge of the cavity dominates the flow separation behaviour on the upper airfoil surface and causes a much higher frequency shedding of small scale vortices compared to the airfoil without cavity.

In figure 4.16 the Strouhal number  $St_h$  based on frontal projected area  $h$ , is plotted as a function of the angle of attack at a probe location in the wake of the airfoil with and without cavity, approximately half a chord length downstream of the trailing edge. The frequency was computed from the dominant peaks in the power spectrum of the vertical velocity at the probe location. In general the spectra of the airfoil with cavity contain



**Figure 4.16** – Strouhal number  $St_h$  at a probe location in the wake downstream of the airfoil with cavity indicated by the solid line with solid markers and for the clean airfoil indicated by the dotted line with open markers.

more peaks and are broader compared to the cases without cavity. Note that the results are not plotted for all the values of the angle of attack, as it was not possible to distinguish a dominant frequency at these angles of attack. The high Strouhal number at  $\alpha = 0^\circ$  for the clean airfoil is caused by the interaction of the separated boundary layers with each other and the trailing edge. At other angles of attack the Strouhal number is determined by the separation bubble.

## 4.6 Conclusion

Results of a two-dimensional Navier–Stokes method for flow around a clean airfoil and an airfoil with cavity were presented. The main goal of these simulations was to explore the possible flow regimes and to gain more insight into the flow physics. The results of low Reynolds number simulations have been compared to high Reynolds number experimental data obtained in a wind tunnel and data from literature. In general the agreement of predicted and experimental data was reasonable. The comparison between results of simulation and experiment should be seen as an indication that the simulations produce physically relevant results and not as a formal validation of the numerical method. The occurrence of turbulence in the experiment, the rather large difference in Reynolds number between that used in the simulations compared to that of the experiments, and the presence of three-dimensional effects were reasons to expect discrepancies between the two sets of results.

The Euler equations are not suited for the simulation of the flow over an airfoil with a cavity. Due to the absence of dissipation the flow inside the cavity accelerates such that the velocity gradient in the shear layer vanishes. The solutions tend to a in which there is uniform vorticity inside the cavity with a stable shear layer over the cavity opening. From this we concluded that application of the no-slip boundary condition is essential. This necessitates solving the complete Navier–Stokes equations.

From the Navier–Stokes results it follows that the local pressure difference near the leading edge is a good measure of the behaviour of the (integrated) lift force. This was also true for the airfoil with cavity.

The relatively large thickness of the airfoil causes a laminar flow separation, which initially starts approximately half a chord length from the leading edge at  $\alpha = 0^\circ$ . Besides the regular vortex shedding due to the separated boundary layers a very low frequency oscillation is present at  $\alpha = 0^\circ$ . This low frequency oscillation appears to be caused by a unique combination of geometry and Reynolds number.

For the airfoil with cavity, the flow in the cavity displays two regimes. For positive values of  $\alpha$  the flow in the cavity is dominated by the second shear layer mode. For negative values of  $\alpha$  the flow in the cavity displays the first shear layer mode. For  $\alpha = 0^\circ$  the flow in the cavity switches back and forth between the second shear layer mode and a more violent first shear layer mode. However, if one applies a small disturbance the first shear layer mode disappears and only the second shear layer mode remains.

In general the oscillations of the shear layer above the cavity generate small vortices, which suppress separation of the boundary layer downstream of the cavity. For  $\alpha = 0^\circ$  the flow on the lower side of the airfoil separates at about 50% chord from the leading edge while the presence of the cavity causes the flow to be attached on the upper side, this asymmetry generates a positive lift force.

For  $\alpha = 4^\circ$  and  $\alpha = 6^\circ$ , the flow over the airfoil with cavity separates upstream of the cavity. In this case the shear layer does not impinge on the surface of the airfoil. The shear layer does interact weakly with the sharp rear edge of the cavity causing a breakup of the shear layer into small-scale structures. In this case the shear layer is dominating the separation bubble behaviour.

At very high angles of attack the flow over the airfoil with cavity separates well upstream of the forward edge of the cavity and the cavity is in the separation bubble. The separated flow displays a strong interaction with the cavity. At  $\alpha = 10^\circ$  this interaction causes the flow to shed smaller-scale structures than the airfoil without cavity at the same angle of attack. Consequently the wake is narrower and the lift-to-drag ratio of the configuration with cavity is higher compared to the case without cavity.

The simulations have revealed interesting flow physics associated with the interaction of no less than three different types of instabilities. A first and second shear layer mode and separation bubble behaviour which is forced by a shear layer oscillation. More elaborate experiments and Large Eddy Simulations for three-dimensional flow would be a logical next step to obtain more data and increase the physical insight.





## Chapter 5

# Flow visualisation and three-dimensional flow effects

In this chapter the results of flow visualisations are presented. A visualisation of the flow is very useful to investigate the flow qualitatively. Our wind tunnel has no optical access and the Reynolds numbers are high, which makes a flow visualisation difficult. For flow visualisation purposes we have therefore used a water channel, which is much more convenient.

First the experimental setup in the water channel will be described in section 5.1. Then, in section 5.2 dye visualisations of the shear layer above the cavity will be presented and a comparison is made with numerical results obtained in the preceding chapter. Three-dimensional flow effects are discussed in section 5.3 and, finally, in section 5.4 a brief summary and the main conclusions are given.

### 5.1 Water channel setup

The water channel used here has a width of 300 mm and a length of 7 m, in which flows with velocities up to about 25 cm/s can be reached. The same airfoil geometry was used as that in the preceding chapter. The airfoil section has a spanwise width of 150 mm, and is bounded at the ends by transparent Plexiglas end plates of dimensions  $30 \times 20 \text{ cm}^2$  and a thickness of 5 mm, to minimise end effects and create quasi-two-dimensional flow over the airfoil, see figure 5.1. The upstream edges of the end plates are

rounded to prevent flow separation and the airfoil is mounted in the middle of the end plates. The airfoil is placed vertically in the water channel at a distance of 1.1 m downstream of the contraction and the water depth is set to 155 mm. A digital photo camera is mounted above the water surface to capture snapshots of the flow. Figure 5.2 shows a schematic of the setup in the water channel. The flow is illuminated by a horizontal light sheet which is created by light from two slide projectors which passes through a slit of 3 mm in black paper. Visualisations are performed by manual injection of fluorescent dye. Additional measurements have been carried out for which the wing is placed horizontally. We will describe these later in section 5.3.

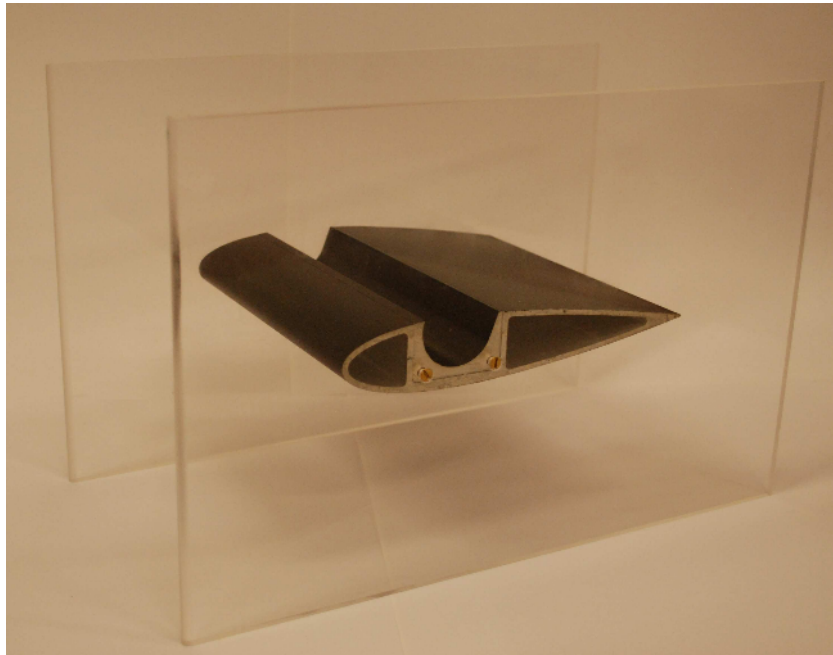


**Figure 5.1** – *NACA0018 airfoil with cavity, mounted in between two closed perspex end plates.*

## 5.2 Cavity modes

In order to observe the shear layer separating the cavity from the main flow, the airfoil is placed vertically in the water channel. The water level is adjusted such that the free surface just touches the upper end plate. This ensures no-slip boundary conditions on both ends of the cavity rather than

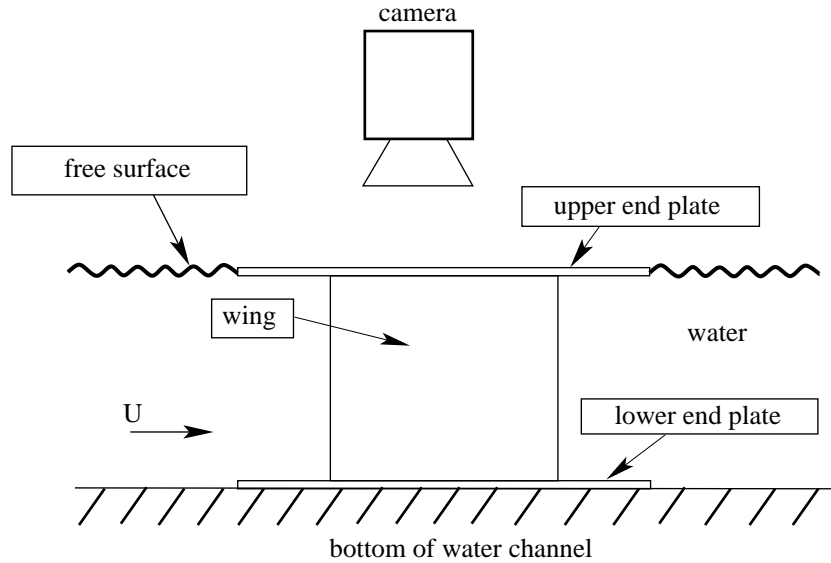


**Figure 5.2** – Side view of the setup in the waterchannel.

no-slip and free-slip when the upper end of the airfoil would extend above the water surface.

In the preceding chapter numerical simulations for two-dimensional flow at a Reynolds numbers of the order of  $Re_c = 10^4$  have been presented. In the water channel we can easily achieve these Reynolds numbers. Figure 5.3 shows the flow visualisations in the water channel as well as plots of the vorticity obtained from the numerical simulations for angles of attack ranging from  $-6^\circ$  to  $+6^\circ$ . Flow visualisations are on the left and the corresponding vorticity plots from the numerical simulations are on the right. In all the figures the direction of the flow is from left to right and  $Re_c = 2 \cdot 10^4$ . Positive vorticity (counter clockwise rotation) is indicated by red and negative vorticity is denoted by blue. To illustrate how the shear layer moves and rolls up, a series of snapshots is shown in figure 5.4. These show the second shear layer mode at  $\alpha = 0^\circ$  and  $Re_c = 10^4$ . The time between the snapshots is  $3.3 \cdot 10^{-2} \frac{c}{U_\infty}$  seconds.

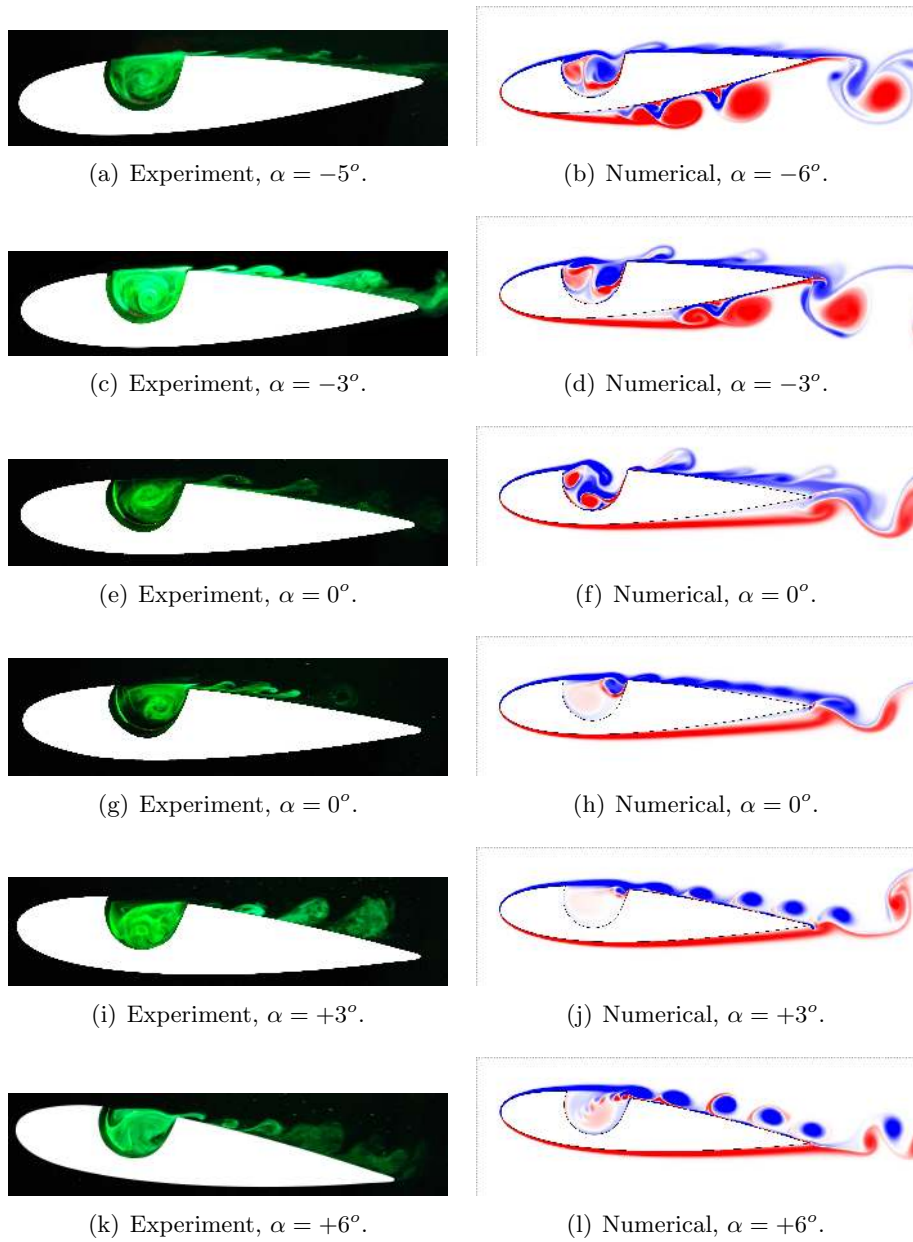


**Figure 5.3** – Oscillations of the shear layer above the cavity as visible in the flow visualisation experiments in the water channel (left panels) and in the vorticity plots obtained from the numerical simulations (right panels), for various values of  $\alpha$  and  $Re_c = 2 \cdot 10^4$ . The levels in the vorticity plots are in the range  $-40 < \frac{\omega c}{U_\infty} < 40$ .

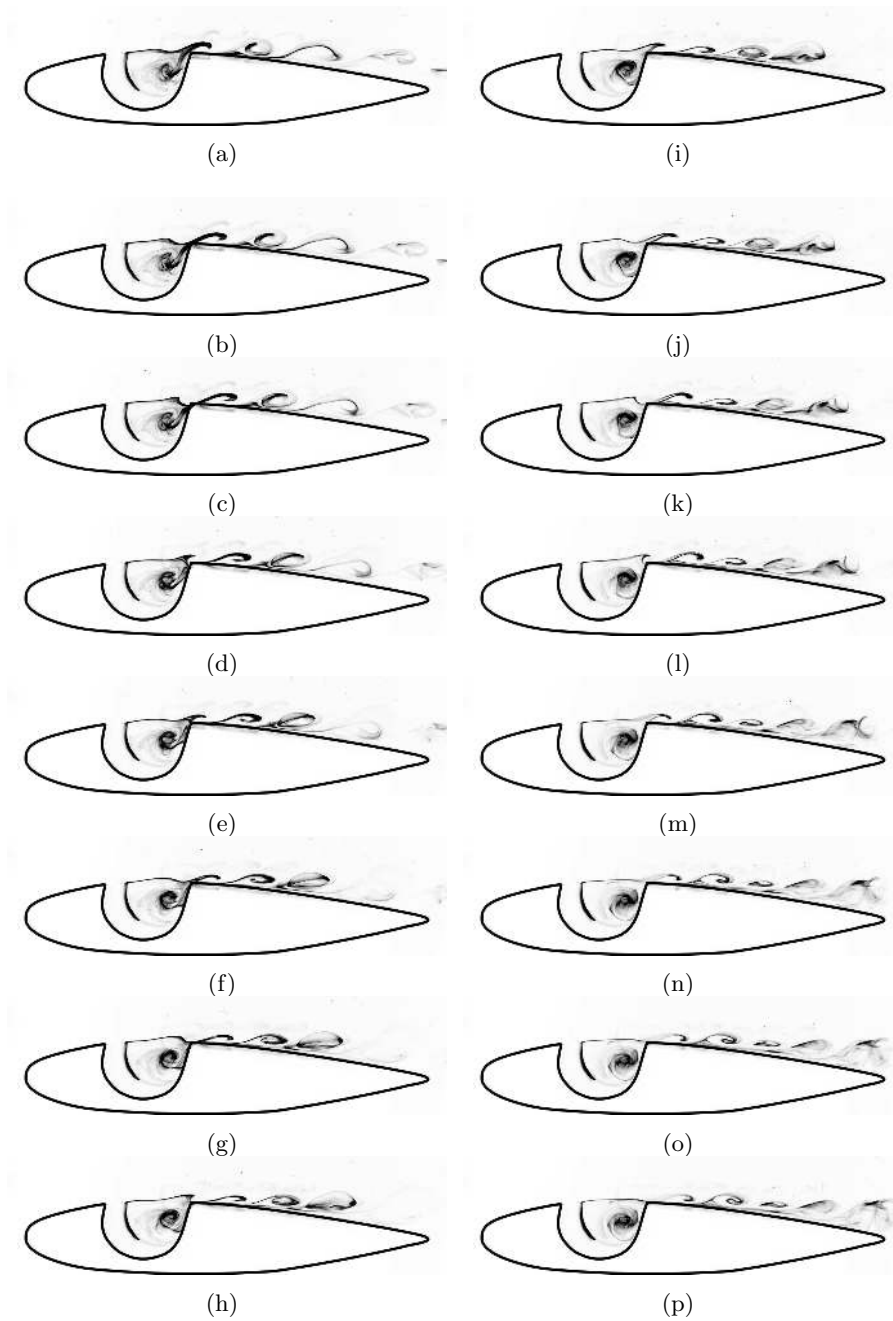


**Figure 5.4** – Flow visualisation snapshots of the second shear layer mode, for  $\alpha = 0^\circ$  and  $Re_c = 10^4$ . The time between the snapshots is  $3.3 \cdot 10^{-2} \frac{c}{U_\infty}$  seconds.

The overall agreement between the experimental flow visualisations and the vorticity fields from the numerical simulations is fair. However, in the experiments we can see the actual roll-up of the shear layers, whereas in the numerical simulations we do not see this much detail, even when the color scale is changed. We must note here that the dye in the experiments is a passive tracer while vorticity is not. For a better comparison between flow visualisations and computations, particle tracking in the computational data could be considered. In the experiments we also observe a transition to turbulence near the trailing edge, especially for high positive angles of attack. This transition to turbulence quickly spreads the dye and diffuses the vortices. Downstream of the trailing edge of the wing the dye has been spread out by turbulence and we do not recognise any vortices. In the two-dimensional flow numerical simulations turbulence does not occur and we observe a laminar well-organised flow field even downstream of the trailing edge. In the numerical results we observe in general two vortices of opposite sign inside the cavity. In the experiments we observe one of these two vortices clearly, the second vortex is probably too weak to be identified.

For zero angle of attack, figures 5.3(e) to 5.3(h), we observe that the shear layer is switching between the first (figures 5.3(e) and 5.3(f)) and second (figures 5.3(g) and 5.3(h)) shear layer mode. We see this for both the experiment and the numerical simulation. However, the first shear layer mode is much more violent in the numerical simulation than in the experiment. In the numerical simulation the vorticity in the cavity is washed out completely (figure 5.3(f)), while in the experiment the flow in the cavity hardly changes (figure 5.3(e)).

From the snapshots, such as the ones shown in figures 5.3(e) to 5.3(l) we can estimate the hydrodynamic wave length,  $\lambda$ , which is the distance between the vortices appearing close to the airfoil surface downstream of the cavity. The hydrodynamic wave length is made non-dimensional with the width of the cavity opening  $W$ . For the first shear layer mode we expect  $\lambda/W = O(1)$  while  $\lambda/W = O(0.5)$  for the second shear layer mode. The estimated values of the ratio  $\lambda/W$  are listed in table III.

The agreement between the estimates from experiments and numerical results of  $\lambda/W$  is good for positive angles of attack. However, for negative angles of attack the numerical solutions display a first shear layer mode, while the experiments show the second shear layer mode.

angle of attack (degrees)	experiment $\lambda/W$	simulation $\lambda/W$
-6.0	0.62	1.1
-2.0	0.53	1.1
0.0	1.0	1.1
0.0	0.54	0.58
1.0	0.58	0.54
3.0	0.71	0.72
6.0	0.54	0.77

**Table III** – Ratios of the hydrodynamic wave length over the width of the cavity opening,  $\lambda/W$ .

### 5.3 Three-dimensional flow effects

In order to investigate three-dimensional flow effects the airfoil is placed horizontally, parallel to the bottom plane of the water channel, such that the top side of the airfoil with the cavity is visible for the camera. The end plates are now vertical and partly extend above the free surface. The light sheet is adjusted such that it is parallel to the surface of the airfoil downstream of the cavity. The water depth is again 155 mm in the free flow.

#### 5.3.1 Two closed end plates

With both perspex end plates attached, as shown in figure 5.1, the flow inside the cavity is observed to be three-dimensional. Initially red dye is injected at one end of the cavity and green dye at the other end, as shown in figure 5.5(a). After some time the dye spreads out to halfway, see figure 5.5(b). The clear interface halfway illustrates the presence of a two cell structure inside the cavity due to three-dimensional flow effects. This confirms experimental observations by Savelsberg & Castro (2008). The secondary flow inside the cavity is most likely due to Bödewadt boundary layers at the ends walls of the cavity, see Bödewadt (1940). The cell structure is also observed at positive and negative angles of attack and the number of cells is always two in our water channel experiments (the number of cells depends probably on the aspect ratio of the cavity, which in our case is  $150/34 = 4.4$ ). Due to the secondary flows inside the cavity it is unlikely that a cavity wake mode type instability will occur. For rectangular cavities in a plane wall, one often observes such a cavity wake



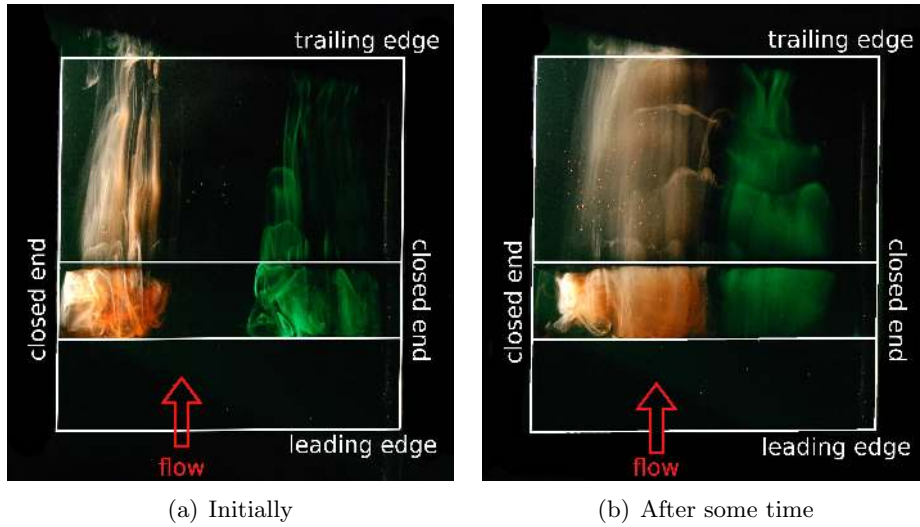


**Figure 5.5** – Top view of the flow over an airfoil with cavity for  $\alpha = 0^\circ$  with two closed end plates. The direction of the flow is from bottom to top,  $Re_c = 10^4$ . Two cell structures are observed in the cavity.

mode in numerical simulations. This corresponds to a build-up of a large vortex in the cavity which is shed periodically. This flow is quite different from the more commonly observed shear layer mode in which vortices are formed periodically in a shear layer separating the main flow from an almost stagnant fluid in the cavity. Numerical simulations by Larchevêque *et al.* (2003) indicate that no-slip boundary conditions, as imposed by our end plates, promote the shear layer mode. Periodic boundary conditions at the side walls promote the cavity wake mode.

For flows along concave walls it is known that Görtler vortices can occur. These manifest themselves as a series of counter-rotating, longitudinal vortices along the wall. More information about Görtler vortices can be found in Görtler (1941); Schlichting (1968); Drazin & Reid (1981). The onset of this instability can be estimated by the Görtler number  $G\ddot{o} = \frac{U_\infty \theta}{\nu} \sqrt{\frac{\theta}{R}}$ , with  $\theta$  the momentum thickness of the boundary layer and  $R$  the radius of curvature of the wall. Experimental observations by Liepmann (1943*a,b*) show the occurrence of the instability at  $G\ddot{o} = 7$ , while linear stability analysis predicts the onset at  $G\ddot{o} = 0.3$ . Assuming that  $\theta$  corresponds to the momentum thickness of a laminar boundary layer along a flat plate of length  $R$  we estimate that in our water channel experiments  $G\ddot{o} \approx 10$ . So

judging on the experimental observations by Liepmann (1943*a,b*) Görtler vortices may appear. However, we did not clearly observe Görtler vortices along the inner wall of the cavity. This is in agreement with the experiments of Savelsberg & Castro (2008).

A flow instability similar to Görtler vortices can occur in cavity flows, however, this instability is generic to the recirculating vortical flow inside the cavity and does not have its origin in instability of the boundary layer. We did observe this type of instability at the upstream wall of the cavity, similar to that shown in figure 18 of Brès & Colonius (2008).

### 5.3.2 One end plate removed

When one of the end plates is removed a strongly turbulent flow is observed, as is shown in figure 5.6. Here the angle of attack is zero and  $Re_c = 10^4$ . Dye injected at either end of the cavity spreads quickly to the center and is convected downstream. By removing one of the end plates the airfoil

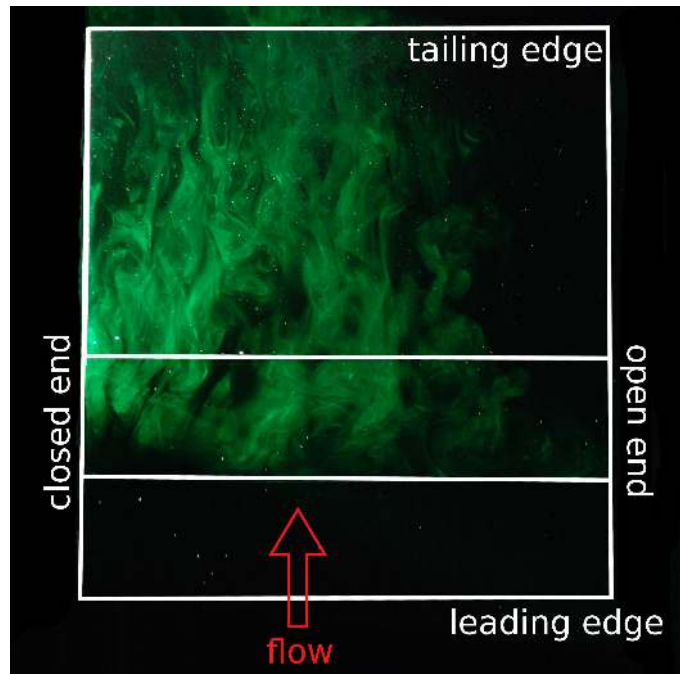


**Figure 5.6** – Visualisation of the flow over an airfoil with cavity for  $\alpha \approx +1^\circ$  and  $Re_c = 10^4$ , with open end condition on the right side. The direction of the flow is from bottom to top.

becomes a finite wing and the flow will become three-dimensional due to the presence of a wing tip vortex. This three-dimensional flow will cause a cross-flow over the cavity. At small angles of attack this tip vortex will be weak. The effect of the tip vortex is expected to be more significant at higher angles of attack. Another fundamental change is the open end cavity termination. A swirling flow at a no-slip boundary will give rise to a Bödewadt boundary layer, which will drive a secondary flow through the vortex core in the direction away from the wall. By removing the end plate the no-slip boundary condition is removed and the associated vortex flow disappears.

We also observe this strongly turbulent flow when we place one or two end plates with a hole at the location of the cavity. Such an end plate with a hole at the location of the cavity is shown in figure 5.7. At zero or positive angles of attack the flow is sucked through the hole and into the cavity, which destabilises the vortex flow in the cavity. This suction is due to the local increase in velocity due to the thickness of the wing.

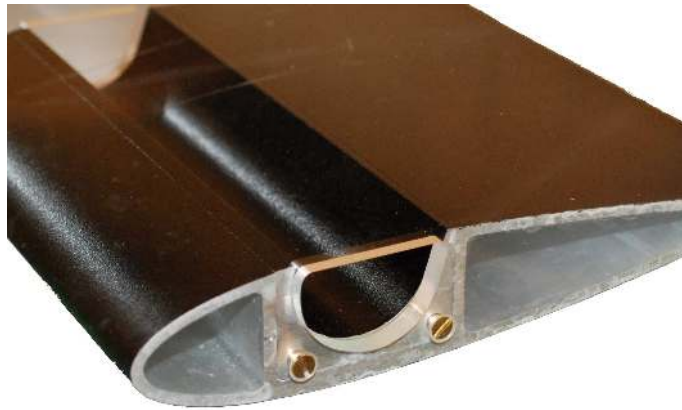


**Figure 5.7** – End plate with a hole at the location of the cavity.

When we terminate the cavity at the end with a small fence, by closing the cavity opening at the wing tip with tape, we again observe a laminar flow in the cavity. At negative and zero angles of attack we recover the two-cell structure as seen in figure 5.5(b). At small positive angles of attack we observe only one cell and the fluid inside the cavity moves quickly along the upstream edge of the cavity from the open end to the closed end, see figure 5.8. At positive angles of attack the flow over the upper surface of the airfoil is expected to be directed inwards, from the tip to the root of the wing.

This causes a cross-flow over the cavity, which may cause the single-cell structure and it may explain the direction of flow inside the cavity. Based on these arguments one would also expect a single-cell structure for negative angles of attack and one would expect the direction of the secondary flow inside the cavity to change sign with respect to the positive angles of attack cases. However, the flow visualisations for negative angles of attack clearly reveal a two-cell structure. For large positive or negative angles of attack dye leaking from the cavity into the tip vortex can be observed (not shown).

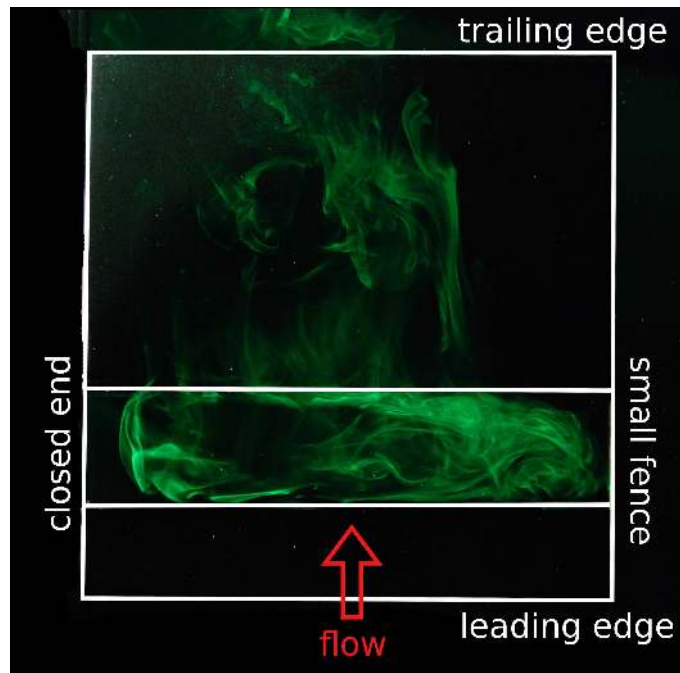


**Figure 5.8** – Visualisation of the flow over an airfoil with cavity for  $\alpha \approx +1^\circ$ ,  $Re_c = 10^4$  and without end plate on the right end of the cavity.

### 5.3.3 External forcing

The effect of forcing can be easily demonstrated. Without external forcing the separation from the downstream edge of the cavity is three-dimensional. However, when a small external forcing is applied, by gentle periodic blowing at the free water surface, the separation at the rear edge of the cavity synchronises over the spanwise direction and large coherent vortices are

shed downstream. The three-dimensional flow separation without forcing is shown in figure 5.9(a) and the quasi-two-dimensional flow separation with external forcing is shown in figure 5.9(b).

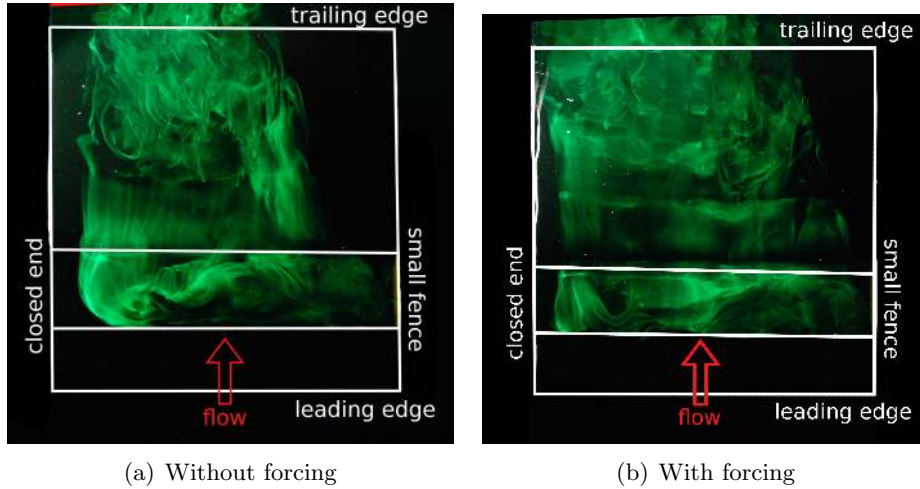


**Figure 5.9** – Top view of the flow over an airfoil with cavity for  $\alpha \approx +1^\circ$  without and with external forcing,  $Re_c = 10^4$ . Forcing is applied by gently blowing periodically at the free surface upstream of the airfoil.

## 5.4 Conclusion

The flow was visualised by the injection of dye in a water channel at Reynolds numbers of the order of  $10^4$ . We observed periodic vortex shedding from the cavity and these oscillations illustrate the presence of a shear layer instability mode. The agreement with results from numerical simulations is reasonable, although the flow visualisations display a transition to turbulence which cannot be resolved in the two-dimensional flow simulations.

Three-dimensional flow effects were investigated experimentally and these investigations indicate that the end conditions of the cavity play a crucial role for the flow regime inside the cavity. When the cavity is open on one or two ends the two-dimensional character of the flow is destroyed completely and a strongly turbulent flow is observed. The placement of a small fence is sufficient to suppress this turbulent flow and a laminar cellular flow structure inside the cavity is established.

It is clear that the flow inside the cavity is a very complex flow in

which effects due to viscosity, three-dimensionality and turbulence are important. We have seen in section 5.2 that when completely ignoring three-dimensional flow effects in the numerical method the agreement with experimental observations is still very reasonable. Since the flow inside the cavity is a relatively low energetic flow and the secondary flows are even less energetic, the exact flow inside the cavity is not expected to significantly contribute to the forces on the airfoil. The main effects on the forces are expected from the oscillating shear layer and shed vorticity. Our visualisation experiments confirm that an acoustical forcing or an oscillation of the wing will promote two-dimensional vortex shedding.



## Chapter 6

# Airfoils with cavities and applied forcing

In this chapter the flow over the airfoil with cavity will be discussed with the external acoustic forcing applied.

An introduction is given in section 6.1. Hereafter in section 6.2 two-dimensional simulations using a method to solve the Navier–Stokes equations are presented with external forcing. The experimental measurements on two NACA0018 airfoils which differ because of slightly different cavity geometries are discussed in section 6.3. The conclusions are presented in section 6.4.

### 6.1 Introduction

In this chapter we will discuss the results obtained for two NACA0018 airfoils each with a different cavity. We will present numerical results as well as experimental data. For the numerical simulations the same two-dimensional Navier–Stokes method is used that was applied in Chapter 4. The experimental results are obtained by application of the experimental method described in Chapter 3, complemented by hot-wire measurements.

One of the cavities has the same geometry as the one used in Chapters 4 and 5; this geometry is shown in figure 6.1(a) and will be referred to in this chapter as the airfoil with cavity *A*. The other cavity shape is similar to cavity *A* and is indicated in figure 6.1(b). This airfoil will be referred to as the airfoil with cavity *B*. Both cavities have the same internal shape, however, cavity *A* has sharp edges on both the upstream and downstream



sides of the cavity, whereas cavity *B* has a short extension plate at the upstream edge while the downstream edge is rounded with a radius of 4 mm. Detailed descriptions of the geometries of the airfoils can be found in Appendix A. The geometry of cavity *B* is designed to approach the

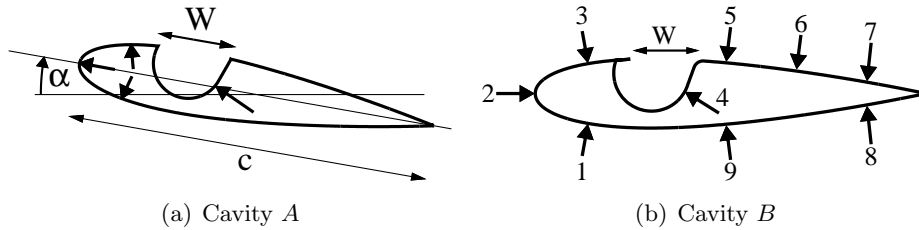


**Figure 6.1** – Geometries of the NACA0018 airfoils with cavity *A* and cavity *B*. The location of pressure transducers is indicated by the arrows. The chord lengths are 165 mm.

generic geometries considered in the VortexCell2050 project, like the cavity shown in figure 1.1 in the introduction of this thesis. The ideas behind this cavity geometry are that the rounded rear edge of the cavity will prevent flow separation and that a cusp is desirable at the upstream edge of the cavity. The idea of a cusp has its roots in inviscid flow theory, in which a finite angle sharp edge, with applied Kutta condition, has a stagnation point at this sharp edge. This stagnation point will cause an increase in pressure as the flow along the wall of the cavity approaches this point. This increase in pressure will promote separation of the boundary layer inside the cavity, which is not desirable. In reality it is impossible to construct such a cusp. In a real flow the design criterion of a cusp is translated into the requirement that the radius of curvature of the sharp edge is small compared to the local boundary layer thickness. The plate applied at the upstream edge of cavity *B* has a thickness of 1 mm and a length of 4 mm. This thickness is comparable to the expected boundary layer thickness just upstream of the edge.

The types of pressure transducers, the mounting location and presence on the airfoil are listed in table IV. For clarity also the specifications of the clean airfoil are presented in this table. Note that the clean airfoil without cavity, used in Chapter 3, is equipped with pressure transducers at locations 1, 2 and 3. The airfoil with cavity *A* is equipped with pressure transducers at locations 1, 2, 3 and 4. The airfoil with cavity *B* is equipped with the nine pressure transducers indicated in figure 6.1(b).

The experimental results presented in this chapter are obtained by ap-

position no.	location $x/c$	Kulite type	clean airfoil	cavity A	cavity B
1	0.133	XCS-093-140mBarD	x	x	x
2	0.000	XCS-093-140mBarD	x	x	x
3	0.133	XCS-093-140mBarD	x	x	x
4	0.376	XCS-093-140mBarD		x	x
5	0.490	LQ-080-0.35BarD			x
6	0.672	LQ-080-0.35BarD			x
7	0.851	LQ-080-0.35BarD			x
8	0.851	LQ-080-0.35BarD			x
9	0.490	LQ-080-0.35BarD			x

**Table IV** – Specification of the pressure transducers and their location for each airfoil.

plication of the acoustic forcing method described in Chapter 3. The results presented are corrected for the streamwise dependence of the acoustic field and the presence of the time dependent pressure gradient due to the oscillating flow (both as described in Chapter 3).

## 6.2 Numerical results of Navier–Stokes method

At the beginning of Chapter 4 we have seen that solutions of the Euler equations yield unphysical results for the case of an airfoil with cavity. Therefore we should solve the Navier–Stokes equations. The results of these numerical simulations in the absence of external forcing were presented in Chapter 4. In this section we will present the results of numerical simulations with external forcing using the same method that was used in Chapter 4. First the results for the clean airfoil are presented and compared to results of Theodorsen’s theory. Then the numerical results obtained for the two different cavities are discussed and compared to results for the clean airfoil.

In the numerical method the plunging motion of the airfoil is simulated as a time dependent oscillatory velocity, by prescribing the velocity fluxes at the cell interfaces in the entire computational domain. Because the method solves the incompressible Navier–Stokes equations, the Helmholtz number is zero and the forcing is uniform. The pressure  $p$  is obtained from a

known velocity field  $\vec{u}$  and vorticity field  $\vec{\omega}$ , by solving the Poisson equation  $\nabla^2(p/\rho + \frac{1}{2}|\vec{u}|^2) = \nabla \cdot (\vec{u} \times \vec{\omega})$ , with  $\rho$  the density and with the condition that the pressure is equal to a reference pressure at the boundary of the domain. By prescribing a constant pressure on the boundary of the domain the time dependent pressure gradient is subtracted from the pressure field. Therefore direct comparison with Theodorsen's theory is possible.

In all the numerical simulations discussed in this chapter,  $Re_c = 2 \cdot 10^4$ ,  $\alpha = 0^\circ$  and the forcing amplitude  $v'/U_\infty = 5 \cdot 10^{-2}$ .

### 6.2.1 Clean airfoil

As a baseline we first present the results of numerical simulations of the flow around the clean airfoil (without cavity). The flow fields observed with external forcing are very similar to those obtained without forcing. The flow separates at about mid chord of the leading edge and the shear layers roll up into concentrated vortices, which form a vortex street downstream of the airfoil. We also observe the very low frequency oscillation, which was encountered for the case without forcing in Chapter 4, section 4.5.1. In figure 6.2 the lift coefficient  $c_l = \frac{2l}{\rho U_\infty^2 c}$  is plotted as a function of the non-dimensional time  $t$ , for two different values of the reduced frequency  $k = \frac{\omega b}{U_\infty}$ , namely  $k = 1$  and  $k = 3$ . Time is made non-dimensional with the

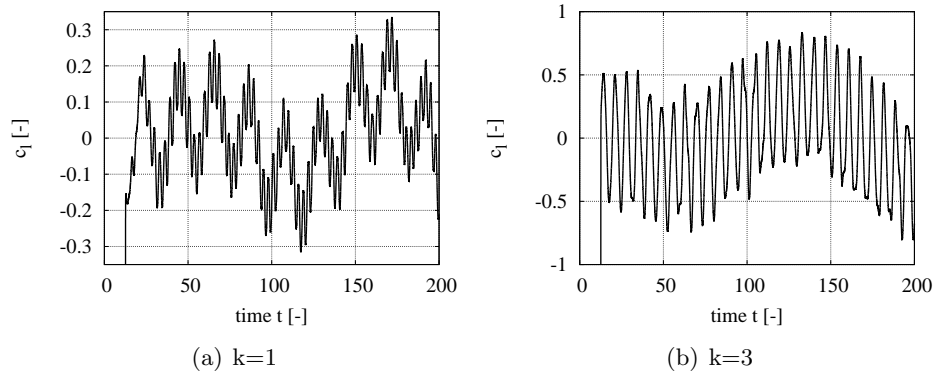


**Figure 6.2** – Lift coefficient as function of non-dimensional time  $t$ , for two different values of the reduced frequency and a forcing amplitude of  $v'/U_\infty = 5 \cdot 10^{-2}$ .

free stream velocity and the reference length, which are both unity. For our simulations this means that the free stream flow travels one chord length every 6.7 non-dimensional time units. The signals do not start at  $t = 0$  because the simulations were started from a precomputed initial condition to

reduce the computational time. For  $k = 1$  (figure 6.2(a)) we clearly observe three different frequencies in the lift coefficient signal. From high frequency to low frequency these are: the vortex shedding due to the laminar boundary layer separation at 50% of the chord, the externally applied forcing and the very low frequency oscillation. As the reduced frequency is increased the component of the force due to the external forcing becomes dominant. At  $k \geq 3$ , the periodic vortex shedding due to the laminar boundary layer separation is no longer observable in the force signal, although it is still visible in the vorticity snapshots of the flow. For  $k = 3$  the very low frequency oscillation is still visible in the force signal. The Strouhal number  $St_h = \frac{fh}{U_\infty}$ , where  $h$  is the thickness of the airfoil, of the natural laminar separation is 0.41 and that of the low frequency oscillation is 0.01. These values correspond to values of the reduced frequency  $k = 7.2$  and  $k = 0.17$ , respectively.

One of the advantages of the numerical simulations, with respect to experiments, is that we can easily compute the total force on the airfoil. The component of the total lift force at the forcing frequency is extracted from the total lift force signal by a lock-in method and made non-dimensional by dividing the lift force by the quasi-steady lift force on a flat plate  $l_0$  (see section 2.2). The amplitude and phase of this non-dimensional unsteady lift force are given in figures 6.3(a) and 6.3(b). The agreement with

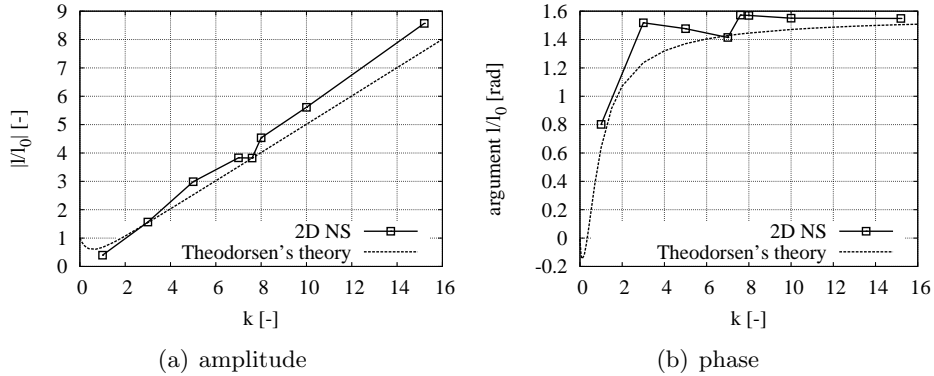


**Figure 6.3** – Unsteady lift  $l/l_0$  from numerical Navier–Stokes simulations. Amplitude and corresponding phase of the non-dimensional force on a NACA0018 airfoil without cavity for  $Re_c = 2 \cdot 10^4$ ,  $\alpha = 0^\circ$ . The forcing amplitude  $v'/U_\infty = 5 \cdot 10^{-2}$ .

Theodorsen's theory is reasonable, considering the laminar boundary layer separation of the boundary layer. The deviations are most evident in the phase plot of the non-dimensional force (figure 6.3(b)) and are expected to

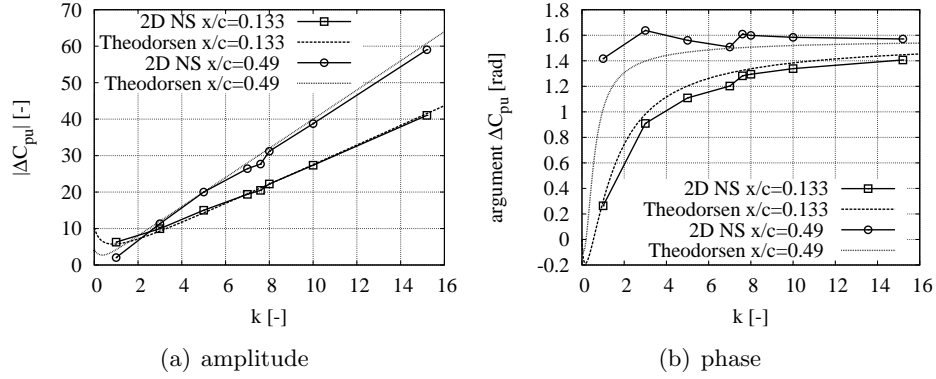


**Figure 6.4** – Unsteady local pressure difference across the airfoil from numerical Navier–Stokes simulations. Amplitude and corresponding phase of  $\Delta C_{pu}$  at two different locations on the airfoil, for the clean airfoil (without cavity) at  $\alpha = 0^\circ$ ,  $Re_c = 2 \cdot 10^4$  and  $v'/U_\infty = 5 \cdot 10^{-2}$ .

be due to the laminar separation of the boundary layer. Indeed the phase displays a clear local minimum at the natural vortex shedding frequency  $k = 7$ .

Figures 6.4(a) and 6.4(b) show the amplitude and phase of non-dimensional difference in pressure coefficient  $\Delta C_{pu} = \frac{2(p_{\text{lower}} - p_{\text{upper}})}{\rho U_\infty v'}$ , respectively. The values of  $\Delta C_{pu}$  are plotted at two different locations, at a position  $x/c = 0.133$  and at  $x/c = 0.49$ . Again the deviations are most obvious in the phase plots. We observe a small dip in the phase around  $k = 7$ . At this reduced frequency the forcing frequency and the natural vortex shedding frequency of the separated boundary layer are close to each other and the forcing might interact with this natural vortex shedding.

It is remarkable that the amplitude of the non-dimensional force (figure 6.3(a)) at high values of  $k$  is significantly above the amplitude predicted by Theodorsen's theory, while the local pressure differences in figure 6.4(a) do not indicate a comparable deviation.

It is noteworthy that the measurements at  $x/c = 0.133$  are very close to Theodorsen's theory, whereas the measurements at  $x/c = 0.49$  indicate deviations which we also observed in the total force. This leads us to the conclusion that the non-dimensional pressure difference at  $x/c = 0.133$  is not an accurate indication of the total force on the airfoil if there is a significant separation of the flow over the airfoil.

### 6.2.2 Airfoil with cavity A

In the preceding section we have seen that the results for the clean airfoil display deviations with respect to Theodorsen’s theory. In this section we will present the numerical results obtained for the airfoil with cavity *A*. These results will be compared to the numerical results obtained for the clean airfoil. This will make it easier to identify specific effects of the cavity, rather than deviation to Theodorsen’s theory, which have already been discussed. Figures 6.5(a) and 6.5(b) display the amplitude and phase of the non-dimensional force ( $l/l_0$ ) as a function of the reduced frequency  $k$ . Figures 6.6(a) and 6.6(b) show the amplitude and phase of  $\Delta C_{pu}$  as a function of the reduced frequency at two chordwise locations. We see that the cavity does not significantly affect the results.

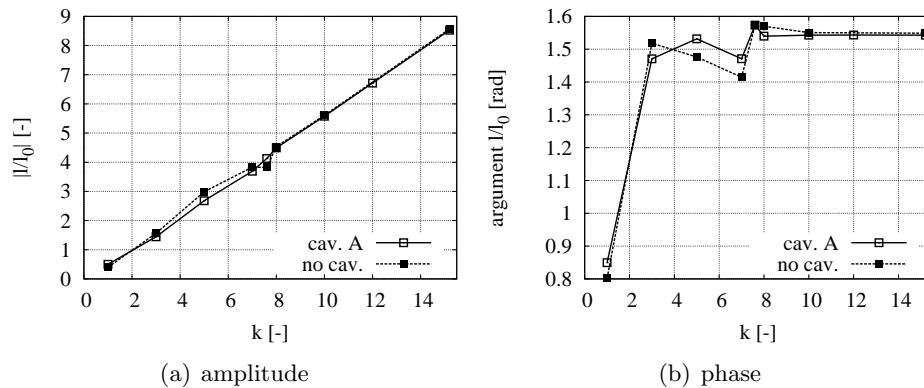


**Figure 6.5** – Results of numerical simulations based on the Navier–Stokes equations. Amplitude and corresponding phase of the non-dimensional lift force on the airfoil with cavity *A* for  $Re_c = 2 \cdot 10^4$ ,  $\alpha = 0^\circ$  and  $v'/U_\infty = 5 \cdot 10^{-2}$ .

### 6.2.3 Airfoil with cavity B

In the preceding section the deviations between the numerical results for cavity *A* were compared to the results for the clean airfoil. In this section the numerical results obtained for cavity *B* will be compared to those obtained for cavity *A*. The comparison will indicate the effect of small changes in the geometry of the cavity. The amplitude and phase of the non-dimensional lift force are presented in figures 6.7(a) and 6.7(b).

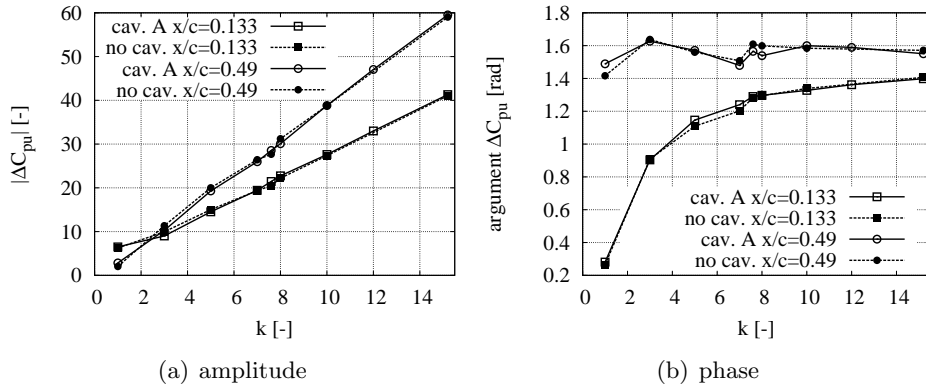


**Figure 6.6** – Results of numerical Navier–Stokes simulations. Amplitude and corresponding phase of  $\Delta C_{pu}$  for the airfoil with cavity A for  $Re_c = 2 \cdot 10^4$ ,  $\alpha = 0^\circ$  and  $v'/U_\infty = 5 \cdot 10^{-2}$ .

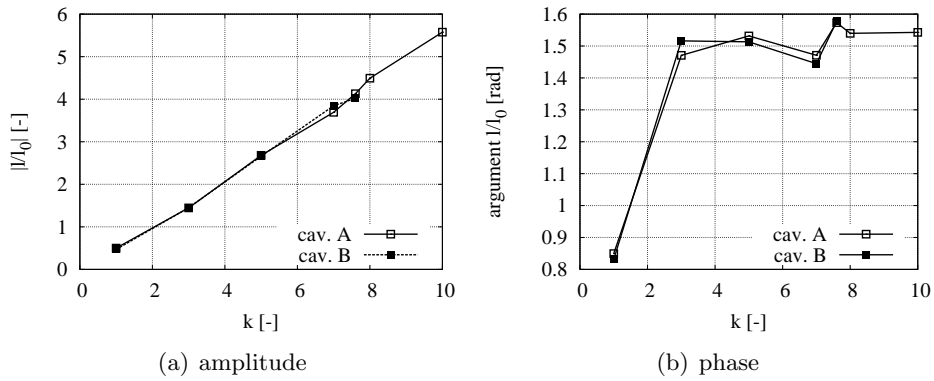


**Figure 6.7** – Results of numerical simulations based on the Navier–Stokes equations. Amplitude and corresponding phase of the non-dimensional force on the airfoil with cavity B for  $Re_c = 2 \cdot 10^4$ ,  $\alpha = 0^\circ$  and  $v'/U_\infty = 5 \cdot 10^{-2}$ .

Only minor deviations between the forces on the airfoil with cavity *A* and those for the airfoil with cavity *B* are observed.

Figures 6.8(a) and 6.8(b) show the amplitude and phase of  $\Delta C_{pu}$  for different values of the reduced frequency. Again no significant deviations

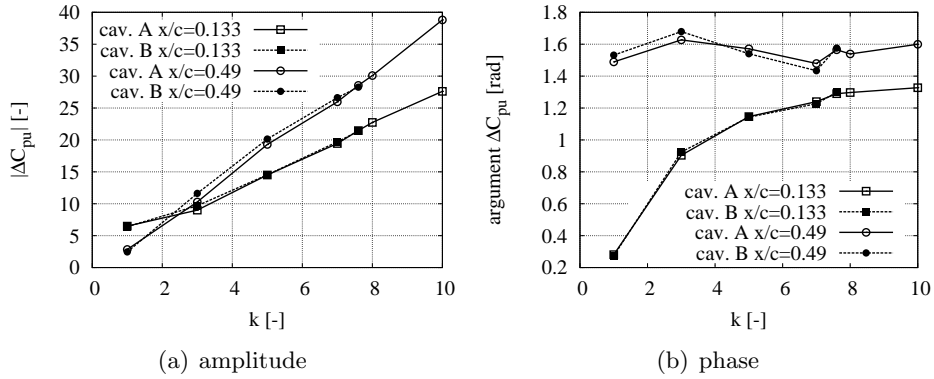


**Figure 6.8** – Results of numerical simulations based on the Navier–Stokes equations. Amplitude and corresponding phase of  $\Delta C_{pu}$  for the airfoil with cavity *B* for  $Re_c = 2 \cdot 10^4$ ,  $\alpha = 0^\circ$  and  $v'/U_\infty = 5 \cdot 10^{-2}$ .

occur. From this we conclude that at low Reynolds number, small changes in geometry have little to no effect on the pressure differences or the lift force.

In the numerical simulation we did observe that the shear layer is sensitive to the forcing frequency. At  $k = 1$  and  $k = 3$  we observe the second shear layer mode, while at  $k > 5$  we observe the first shear layer mode. However, this change in shear layer mode does not appear to have a noticeable effect on the local pressure differences nor on the lift force.

## 6.3 Wind tunnel experiments

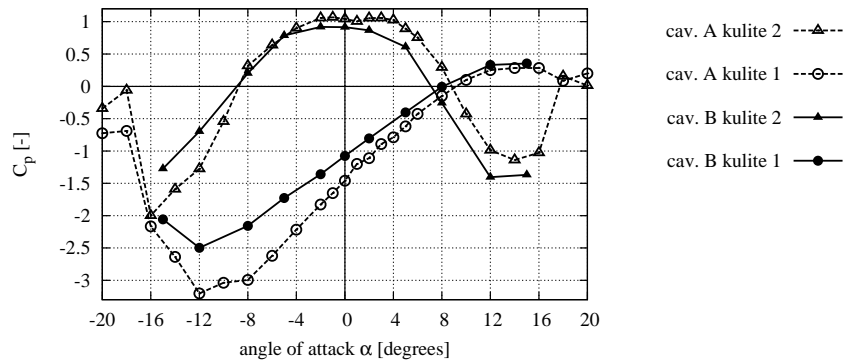
In the preceding section the results of two-dimensional, numerical simulations for low Reynolds number ( $Re_c = 2 \cdot 10^4$ ) have been presented. In this section the results of wind tunnel measurements at higher Reynolds ( $Re_c \approx 5 \cdot 10^5$ ) number are discussed.

### 6.3.1 Steady flow

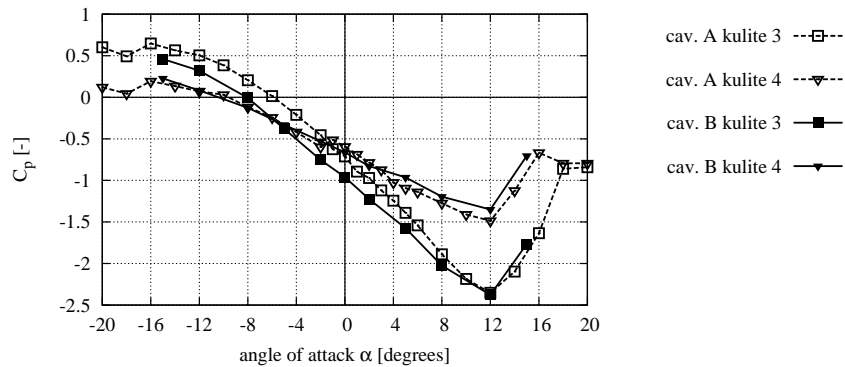
The experimental values for the time averaged pressure coefficient  $C_p$  for the airfoil with cavity *A* have already been discussed and compared to



numerical results in Chapter 4. In this subsection the experimental results in the absence of acoustic forcing are presented. The values of  $C_p$  are shown for the airfoil with cavities  $A$  and  $B$  in figure 6.9. These results are obtained for  $Re_c = 4.4 \cdot 10^5$ . We observe that the results obtained for cavity  $A$  and  $B$  are quite similar. Only at negative angles of attack the pressure on the suction side attains lower values for cavity  $A$  compared to cavity  $B$ .



(a)



(b)

**Figure 6.9** – Experimental values of the time-averaged pressure coefficient  $C_p$  as a function of the angle of attack,  $\alpha$ , for the airfoil with cavities  $A$  and  $B$  at four different locations on the airfoil surface.  $Re_c = 4.4 \cdot 10^5$ . The locations are indicated by the numbers in the legend, which correspond to the numbers in figure 6.1(b).

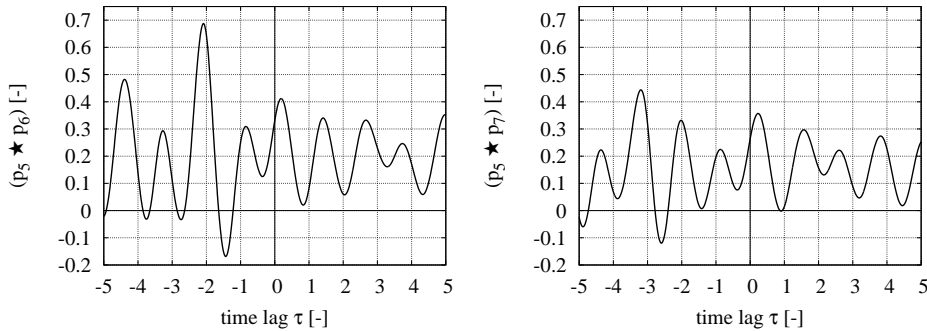
The airfoil with cavity  $B$  is equipped with three pressure transducers downstream of the cavity. If there is periodic vortex shedding from the cavity we might be able to detect this vortex shedding by cross-correlating

the time signals from these pressure transducers.

The cross-correlation between two signals in the time domain  $S_1(t)$  and  $S_2(t)$  is normalised by the square root of the product of the separate auto-correlations at zero time lag and is defined as

$$(S_1 \star S_2)(\tau) = \frac{\int_{-\infty}^{+\infty} (S_1(t) - \overline{S_1}) \cdot (S_2(t + \tau) - \overline{S_2}) dt}{\sqrt{\int_{-\infty}^{+\infty} (S_1(t) - \overline{S_1})^2 dt \cdot \int_{-\infty}^{+\infty} (S_2(t) - \overline{S_2})^2 dt}}, \quad (6.1)$$

where the overbar denotes the time-averaged value. In the numerical simulations presented in Chapter 4 and in the water channel visualisations of Chapter 5, we clearly observed periodic vortex shedding from the cavity. To illustrate the signal we may expect from the cross-correlation we calculate the cross-correlations from the numerical simulation of the airfoil with cavity  $A$ . Here we use the numerical data without external forcing, at  $\alpha = 0^\circ$  and  $Re_c = 2.01 \cdot 10^4$ . We calculate the cross-correlation between the pressure probes near the airfoil surface, downstream of the cavity at  $x/c = 0.49$ ,  $x/c = 0.7$  and  $x/c = 0.8$ . These signals will be denoted by  $p_5$ ,  $p_6$  and  $p_7$ , respectively. Figures 6.10(a) and 6.10(b) display the resulting cross-correlations as a function of the time lag  $\tau$ . The time  $\tau$  corresponds



(a) Cross-correlation between  $p_5$  and  $p_6$ . (b) Cross-correlation between  $p_5$  and  $p_7$ .

**Figure 6.10** – Cross-correlations as a function of the time lag  $\tau$  of the pressure signals obtained for NACA0018 with cavity  $A$  by numerical Navier–Stokes simulations at  $\alpha = 0^\circ$  and  $Re_c = 2.01 \cdot 10^4$ . Pressure probe  $p_5$  is located just downstream of the cavity at  $x/c = 0.5$ ,  $p_6$  is located at  $x/c = 0.7$  and  $p_7$  at  $x/c = 0.8$ .

to the non-dimensional time in the numerical simulations, which is made non-dimensional with the reference length and the reference velocity, which are both unity. In the simulations the chord length of the airfoil is 6.7, which means that every non-dimensional time unit the free stream travels approx-

imately 0.15 chord lengths. In figure 6.10(a) we observe a peak at a time lag of  $\tau = -2$ , which corresponds to a convective velocity of  $\frac{(0.7-0.5) \cdot 6.7}{2} = 0.67$ , which is 67% of the free stream velocity. In figure 6.10(b) the peak is located at  $\tau = -3.2$ , which corresponds to 63% of the free stream velocity. From the figures we can also estimate the frequency of the vortex shedding and calculate the Strouhal number  $St_W = \frac{fW}{U_\infty}$ , based on the width of the cavity opening  $W$ . From the figures we estimate that  $f = 0.83$  and it follows that  $St_W = 1.14$ .

From the pressure measured at probe  $p_5$ , just downstream of the cavity, we estimate that the amplitude of the fluctuations in the pressure coefficient is of the order of 0.1. This corresponds to pressure fluctuations of the order of 10% of the stagnation pressure,  $\frac{1}{2}\rho U_\infty^2$ , which should be large enough to detect using the pressure transducers used in our experiments.

From experimental data the cross-correlation between the pressure signals from pressure transducers 5, 6 and 7 has been calculated, for the airfoil with cavity  $B$ . These cross-correlations do not show the clear sinusoidal signal as observed in the numerical data. At angles of attack up to  $+5^\circ$  no clear peak can be detected, which may indicate that the pressure fluctuations are too small to measure. For an angle of attack of  $+15^\circ$  the cross-correlation displays only one peak at a convective velocity of 30 m/s, with a free stream velocity of 40 m/s. The presence of only one peak which does not repeat itself is an indication for turbulence, which is convected downstream, rather than periodic vortex shedding as observed at low Reynolds number, as demonstrated in Chapters 4 and 5.

### 6.3.2 Hot-wire anemometry

At high Reynolds numbers ( $Re_c \geq 10^5$ ) we were not able to observe vortex shedding as predicted by two-dimensional flow simulations, using the available pressure transducers. This could be due to the effect of turbulence. At low velocities corresponding to the Reynolds number of the numerical simulations ( $Re_c = O(10^4)$ ), the pressure transducers are not sensitive enough to detect flow fluctuations. We use hot-wire anemometry in order to allow measurements at these low flow velocities.

The hot-wire probe (one-dimensional Dantec P5511, wire thickness 5  $\mu\text{m}$ ) can be used for velocities above 1 m/s. Our probe is fixed to the bottom of the test section, as shown in the schematic drawing in figure 6.11. The probe holder consists of a small tube with a diameter of 6 mm and a length of 200 mm, which is reinforced at the rear by means of a copper

plate of 2 mm thickness and 20 mm width. The tube with the copper plate is fixed to the bottom of the test section, such that the copper plate at the rear is aligned along the flow direction. Inside the tube a narrower tube is fitted, which holds a small construction in which the hot-wire is mounted horizontally. The narrower tube can rotate inside the wider tube, which allows the positioning of the hot-wire with an accuracy of 1 mm. The hot-wire is positioned at 145 mm up from the bottom of the test section. The position of the hot-wire will be given in a coordinate system fixed to the airfoil, with the origin at the upstream edge of the cavity and the  $x$ -axis parallel to the chord line, see figure 6.12. The position of the hot-

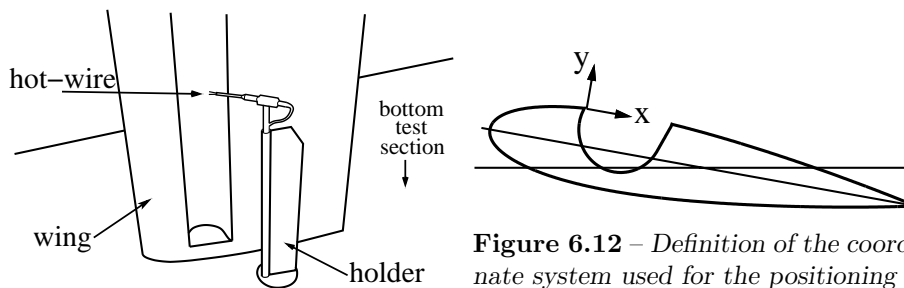


**Figure 6.12** – Definition of the coordinate system used for the positioning of the hot-wire.

**Figure 6.11** – Sketch of the hot-wire mounting inside the test section.

wire probe is made non-dimensional with the width of the cavity opening  $W$ . The upstream edge is at the origin while the downstream edge of the cavity is located close to  $(x/W, y/W) = (1, 0)$ . The difference between the downstream edge of the cavity and  $(x/W, y/W) = (1, 0)$  is due to the fact that the line joining the edges of the cavity is not exactly parallel to the chord line.

All hot-wire signals are recorded with a data acquisition system (National Instruments) at a sampling frequency of 12 kHz. The time signals are post-processed with a Fast Fourier Transform, using averaging over windows, with 50% overlap and on every window a Hanning window is applied. The width of the windows is approximately 1.3 seconds and a total of 150 windows is typically used for this averaging.

Here we present measurements carried out on the airfoil with cavity A, see figure 6.1(a). The hot-wire is positioned just upstream of the downstream edge of the cavity. The largest flow oscillations of the shear layer are expected at the downstream side of the cavity. Figure 6.13 shows the time averaged velocity profile over the shear layer for  $\alpha = +5^\circ$  and  $Re_c = 3.3 \cdot 10^4$ . The magnitude of the velocity is made non-dimensional with the free stream

velocity  $U_\infty$ . The free stream velocity  $U_\infty$  is measured at  $\alpha = 0^\circ$  with the hot-wire positioned at  $(\frac{x}{W}, \frac{y}{W}) = (1.7, 1.8)$ . We see that the shear layer has an approximate thickness of 3 mm and the air inside the cavity is almost stagnant. The fact that the velocity in the cavity is very low indicates that, as observed in the visualisations and the Navier–Stokes simulations, we do not have a Batchelor flow in the cavity, which would involve a uniform vorticity distribution (section 4.2).

We need to be careful in interpreting the hot-wire signal because the hot-wire measures the absolute value of the velocity in the direction perpendicular to the wire. A purely sinusoidal time dependence of the velocity at a frequency  $f$  would result in a hot-wire signal with a fundamental frequency at  $2f$ . At the outer edge of the shear layer this problem does

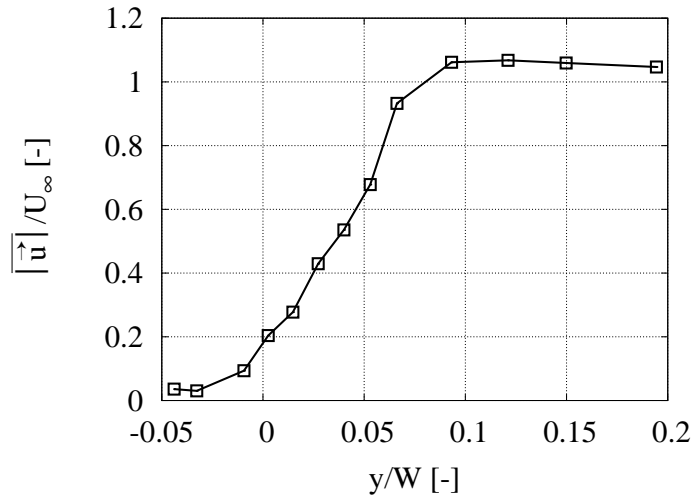


**Figure 6.13** – Measured mean velocity profile across the shear layer over cavity A as a function of  $y/W$ , for  $Re_c = 3.3 \cdot 10^4$ ,  $\alpha = +5^\circ$  and  $0.7 < x/W < 0.93$ .

not occur because the velocity never vanishes, due to the contribution of the main flow. We expected problems at the inner cavity side of the shear layer. However, for all the measurement locations within the shear layer of figure 6.13 we observed only one dominant peak in the frequency domain at 56 Hz. Even at the inner side of the shear layer we did not observe a frequency doubling. We therefore conclude that the measured frequency is the actual oscillation frequency of the shear layer.

At a Reynolds number of  $Re_c = 3.3 \cdot 10^4$  we observe a laminar flow type of signal, with distinct peaks in the frequency domain. Figures 6.14 to 6.18 show a short sample of the hot-wire signal on the left and the corresponding

averaged power spectrum on the right for different values of the angle of attack  $\alpha$ . The magnitude of the velocity is made non-dimensional with the free stream velocity  $U_\infty$  and time is made non-dimensional with the ratio of the free stream velocity and the chord length  $c$  of the airfoil. At each angle of attack the hot-wire position is such that  $0.2 \leq |\bar{u}|/U_\infty \leq 0.7$ , which ensures that the hot-wire is inside the shear layer. For  $\alpha = +5^\circ$ , in figure 6.15, also the hot-wire signal and power spectrum are shown with an acoustic forcing of  $v'/U_\infty = 2.5 \cdot 10^{-2}$ .

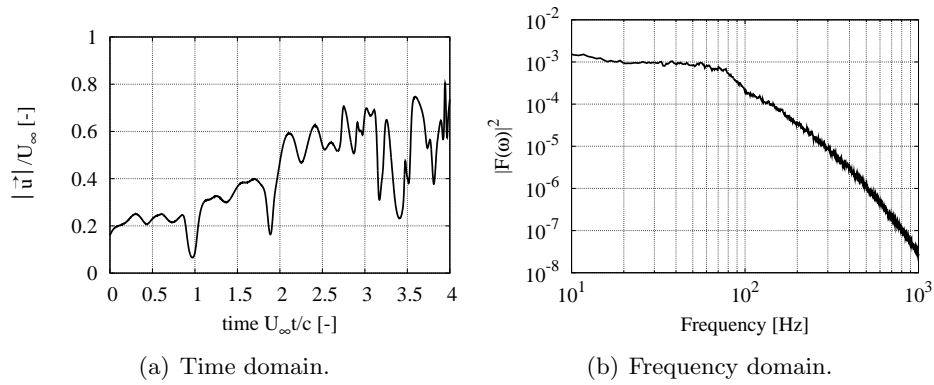


**Figure 6.14** – Time and frequency domain data for the airfoil with cavity A at  $Re_c = 3.3 \cdot 10^4$  and  $\alpha = +10^\circ$ . Hot-wire position:  $(x/W, y/W) = (0.66, 0.20)$ . No acoustic forcing.

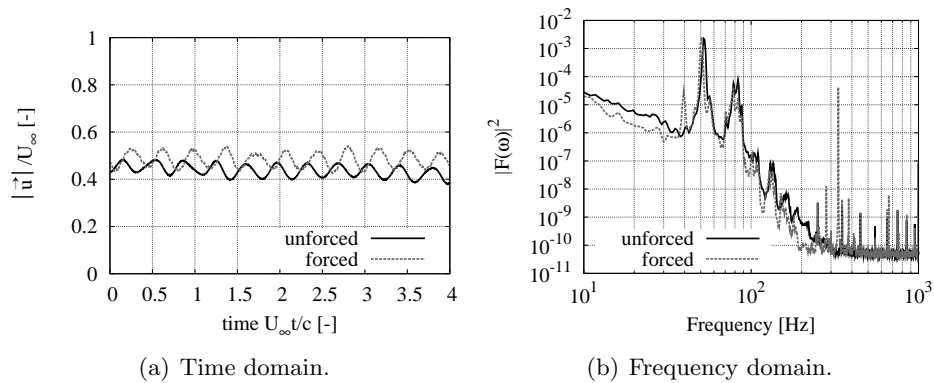


**Figure 6.15** – Time and frequency domain data for the airfoil with cavity A at  $Re_c = 3.3 \cdot 10^4$  and  $\alpha = +5^\circ$ . Hot-wire position:  $(x/W, y/W) = (0.89, -0.0094)$ . Without (unforced) and with an acoustic forcing of  $v'/U_\infty = 2.5 \cdot 10^{-2}$  (forced). The peaks at 51 and 78 Hz corresponds to  $St_W = 0.6$  and  $St_W = 0.9$ , respectively.

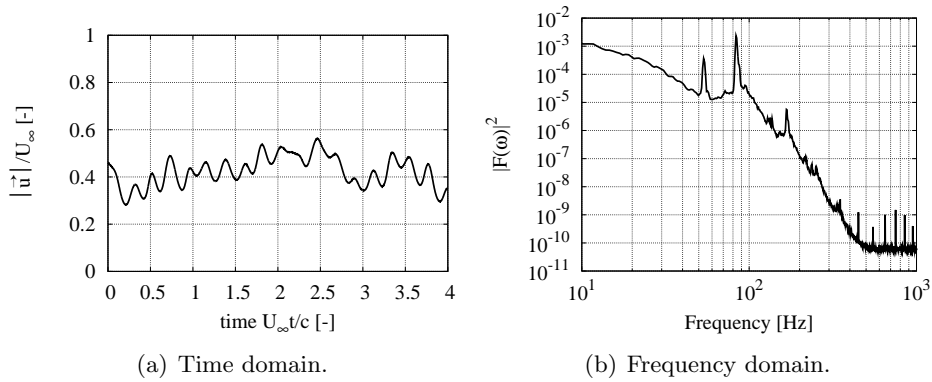


**Figure 6.16** – Time and frequency domain data for the airfoil with cavity A at  $Re_c = 3.3 \cdot 10^4$  and  $\alpha = 0^\circ$ . Hot-wire position:  $(x/W, y/W) = (0.92, -0.045)$ . No acoustic forcing. The peaks at 53 and 83 Hz correspond to  $St_W = 0.6$  and  $St_W = 0.9$ , respectively.

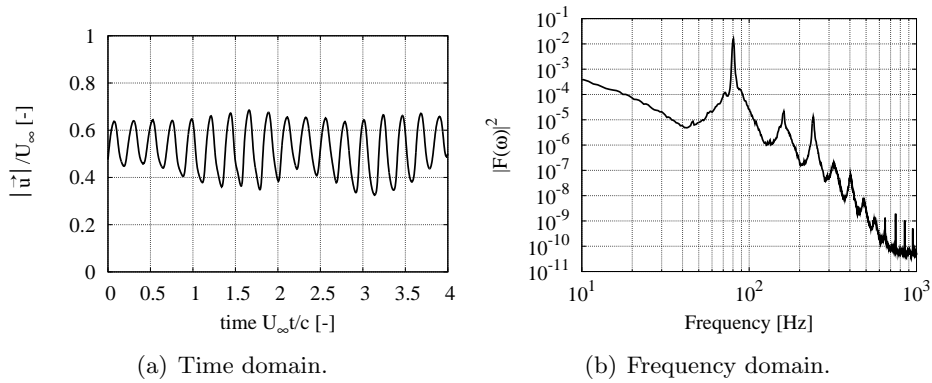


**Figure 6.17** – Time and frequency domain data for the airfoil with cavity A at  $Re_c = 3.3 \cdot 10^4$  and  $\alpha = -5^\circ$ . Hot-wire position:  $(x/W, y/W) = (0.93, -0.054)$ . No acoustic forcing. The peak at 80 Hz corresponds to  $St_W = 0.9$ .

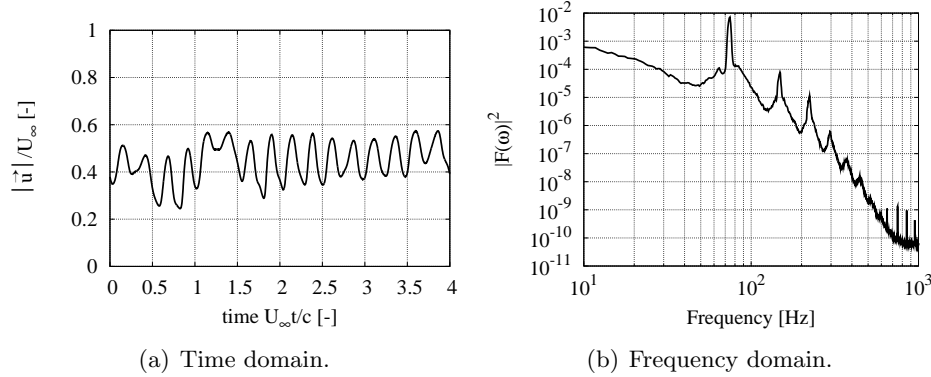


**Figure 6.18** – Time and frequency domain data for the airfoil with cavity A at  $Re_c = 3.3 \cdot 10^4$  and  $\alpha = -10^\circ$ . Hot-wire position:  $(x/W, y/W) = (0.95, -0.077)$ . No acoustic forcing. The peak at 76 Hz corresponds to  $St_W = 0.9$ .

For  $\alpha = +10^\circ$  no peak in the spectrum is present and the time signal oscillates in a larger range from  $|u|/U_\infty \approx 0.2$  up to  $|u|/U_\infty \approx 0.7$ . Most likely the flow is separated upstream of the cavity and turbulent at the position of the hot-wire. At  $\alpha = +5^\circ$  a clear narrow peak in the spectrum at 51 Hz is observed. This corresponds to a Strouhal number based on the width of the cavity opening of  $St_W = \frac{fW}{U_\infty} = 0.6$ , which indicates the presence of the first shear layer mode. We also observe a lower peak at 78 Hz, corresponding to  $St_W = 0.9$ , which might correspond to the second shear layer mode. With the acoustic forcing switched on a large peak at the forcing frequency of 332 Hz appears, but no clear peak appears at the second harmonic of the forcing frequency at 664 Hz. A peak at the second harmonic would indicate non-linear effects, such as the roll-up of the shear layer. With forcing the peaks at 51 Hz and 78 Hz remain. Also the hot-wire signals with and without acoustic forcing are very similar (figure 6.15(a)). These are all indications that the shear layer is not sensitive to the acoustic forcing, which might be due to the low Reynolds number and the correspondingly thick shear layer. This is confirmed by the measurements of the amplitude dependency of the response, which will be discussed later. For  $\alpha = 0^\circ$  we also observe two peaks at 53 and 83 Hz, however, now the peak at 83 Hz is dominant. For  $\alpha = -5^\circ$  and  $\alpha = -10^\circ$  the dominant peaks are located around 80 Hz, which corresponds to  $St_W = 0.9$ .

For  $\alpha < 0^\circ$  only the second shear layer mode is present. For  $\alpha \geq 0^\circ$  two peaks appear, which could be due to a mix of the first and second shear layer mode. It is, however, also possible that only the second shear



layer mode is present but one rolled-up vortex is injected into the cavity and the next vortex is ejected out of the cavity. The alternating injection and subsequent ejection of a vortex is repeated periodically, resulting into period doubling. This behaviour is illustrated in Hofmans (1998) (page 178, figure 6.28).

We now increase the Reynolds number for  $\alpha = +5^\circ$  and show the hot-wire signal and power spectra with and without acoustic forcing. In figure 6.19 the hot-wire signal and power spectrum are shown at  $Re_c = 6.3 \cdot 10^4$ , without acoustic forcing and with an acoustic forcing of  $v'/U_\infty = 3.9 \cdot 10^{-2}$ . Here two clear peaks are present in the spectrum without acoustic forcing: one at 86 Hz and one at 147 Hz, corresponding to  $St_W = 0.6$  and  $St_W = 1.1$ ,

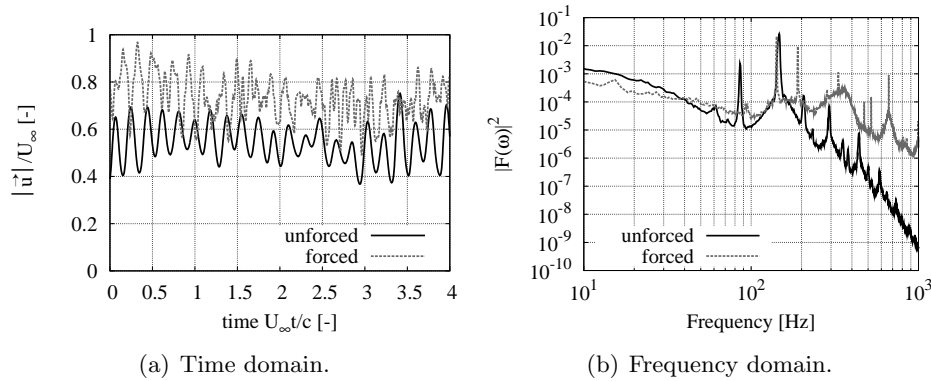


**Figure 6.19** – Time and frequency domain data for the airfoil with cavity A at  $Re_c = 5.0 \cdot 10^4$  and  $\alpha = +5^\circ$ . Without (unforced) and with an acoustic forcing of  $v'/U_\infty = 3.9 \cdot 10^{-2}$  (forced). Hot-wire position:  $(x/W, y/W) = (0.89, -0.0094)$ . The peaks in the spectrum without acoustic forcing at 86 and 147 Hz correspond to  $St_W = 0.6$  and  $St_W = 1.1$ , respectively. With acoustic forcing the peaks at 142 and 190 Hz correspond to  $St_W = 1.1$  and  $St_W = 1.4$ .

respectively. With the acoustic forcing switched on the mean velocity in the shear layer increases and the hot-wire signal is more irregular. In the spectrum the peak at 86 Hz disappears, but a new peak at 190 Hz appears. Furthermore, we see a peak at the forcing frequency (332 Hz) and its higher harmonics. At  $Re_c = 5.0 \cdot 10^4$  the acoustic forcing has an effect, but it does not completely dominate the shear layer dynamics.

Figure 6.20 shows the hot-wire signal and power spectrum at  $Re_c = 6.3 \cdot 10^4$  without acoustic forcing and with an acoustic forcing of  $v'/U_\infty = 2.5 \cdot 10^{-2}$ . Without acoustic forcing a low peak at 108 Hz is observed and a high peak at 270 Hz, corresponding to  $St_W = 0.6$  and  $St_W = 1.6$ , respectively.

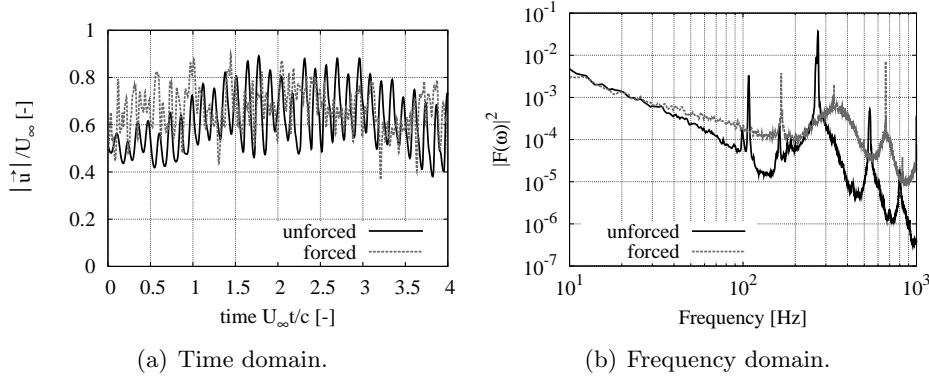


**Figure 6.20** – Time and frequency domain data for the airfoil with cavity A at  $Re_c = 6.3 \cdot 10^4$  and  $\alpha = +5^\circ$ . Without (unforced) and with an acoustic forcing of  $v'/U_\infty = 2.5 \cdot 10^{-2}$  (forced). Hot-wire position:  $(x/W, y/W) = (0.89, -0.0094)$ . The peaks in the spectrum without acoustic forcing at 108 and 270 Hz correspond to  $St_W = 0.6$  and  $St_W = 1.6$ , respectively.

The subsequent peaks are higher harmonics of the peak at 270 Hz. With the acoustic forcing switched on the peaks at 108 Hz and 270 Hz (and the higher harmonics) disappear and peaks at the forcing frequency of 332 Hz and its higher harmonics (664 Hz) appear. Also a peak at the first subharmonic appears at 166 Hz. An example of a non-linear effect causing a subharmonic (period doubling) is the previously discussed periodic alternation between injection and subsequent ejection of a vortex. Here the shear layer clearly locks in at the forcing frequency, which results in  $St_W = 1.9$ . Also the hot-wire signals are different, with the acoustic forcing switched on the velocity fluctuations are more irregular. At this Reynolds number ( $Re_c = 6.3 \cdot 10^4$ ) the lock-in of the shear layer to the forcing frequency occurs even for extremely low forcing amplitudes, such as  $v'/U_\infty = 3.5 \cdot 10^{-4}$ . In the spectrum with acoustic forcing there also appears a peak at 4 Hz (not shown), which is likely to be a global oscillation of the entire wind tunnel flow.

Figure 6.21 shows the time signal and power spectrum at  $\alpha = +5^\circ$  and  $Re_c = 1.0 \cdot 10^5$ . The data is shown without acoustic forcing and with an acoustic forcing of  $v'/U_\infty = 1.4 \cdot 10^{-3}$ . Here also the peak at 4 Hz is present, both with and without acoustic forcing. Without acoustic forcing we also observe two oscillations of the shear layer, a low peak at 460 Hz and a high peak at 915 Hz, which correspond to  $St_W = 1.7$  and  $St_W = 3.4$ , respectively. With acoustic forcing we again observe high peaks at the

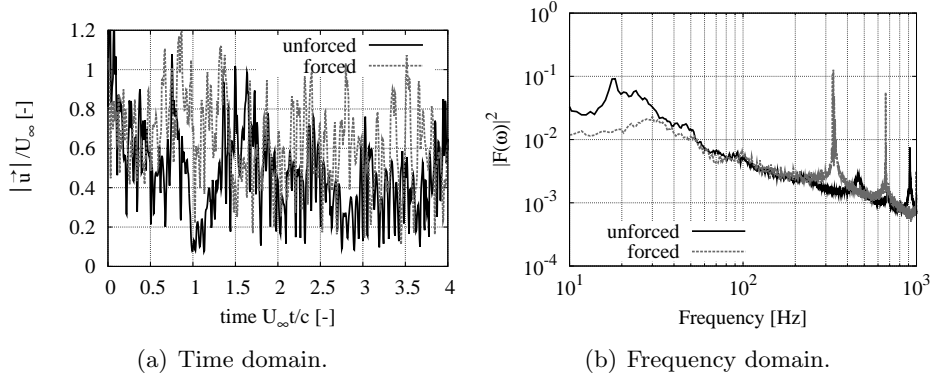


**Figure 6.21** – Time and frequency domain data for the airfoil with cavity A at  $Re_c = 1.0 \cdot 10^5$  and  $\alpha = +5^\circ$ . Without (unforced) and with an acoustic forcing of  $v'/U_\infty = 1.4 \cdot 10^{-3}$  (forced). Hot-wire position:  $(x/W, y/W) = (0.93, -0.044)$ . The peaks in the spectrum without acoustic forcing at 460 and 915 Hz correspond to  $St_W = 1.7$  and  $St_W = 3.4$ , respectively.

forcing frequency of 332 Hz and its higher harmonics. We do not observe a subharmonic at 166 Hz. The peaks at 460 Hz and 915 Hz have disappeared. The hot-wire signals with and without acoustic forcing are similar.

When the shear layer locks in at the forcing frequency we expect the Fourier coefficient of the hot-wire signal at the forcing frequency to be independent of the forcing amplitude. This is due to the saturation of the shear layer response. The acoustic forcing only triggers the shear layer instability. In figure 6.22 the shear layer response at the forcing frequency is plotted as a function of the forcing amplitude. The response at the forcing frequency and the plunging velocity amplitude are made non-dimensional with the free stream velocity  $U_\infty$ . We see that for  $Re_c = 3.3 \cdot 10^4$  the response is nearly linear, which means that there is only a superposition of the acoustic field on the natural shear layer oscillation mode. However, at  $Re_c = 6.3 \cdot 10^4$  and  $Re_c = 1.0 \cdot 10^5$  the shear layer response shows a very different behaviour. For  $v'/U_\infty < 10^{-2}$  the response is at least an order of magnitude larger compared to the case of  $Re_c = 3.3 \cdot 10^4$  and does not depend linearly on the forcing amplitude. This confirms that the signal is due to a lock-in of the shear layer oscillation to the acoustic forcing.

At  $Re_c = 2.0 \cdot 10^5$  and  $Re_c = 4.4 \cdot 10^5$  the boundary layer is likely to be turbulent upstream of the cavity. The results obtained with the hot-wire are similar. For this reason we only show the results obtained at  $Re_c = 4.4 \cdot 10^5$  in figure 6.23. Both results without acoustic forcing and with an

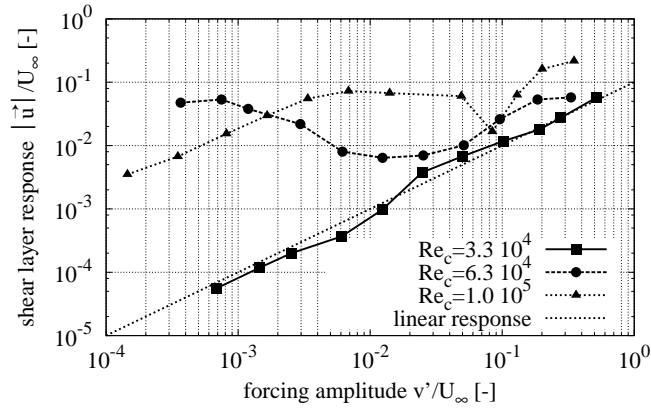


**Figure 6.22** – Shear layer response as a function of the forcing amplitude  $v'/U_\infty$  for three values of the Reynolds number  $Re_c$ , based on the chord length.

acoustic forcing of  $v'/U_\infty = 1.0 \cdot 10^{-2}$  are shown. In figure 6.23(a) both hot-wire signal appear similar with and without acoustic forcing. Also the power spectra are similar, except for the peak at the forcing frequency of 332 Hz and a peak at 358 Hz. In both spectra two peaks at 26 Hz and 53 Hz are observed, which most likely correspond to an acoustic wind tunnel resonance.

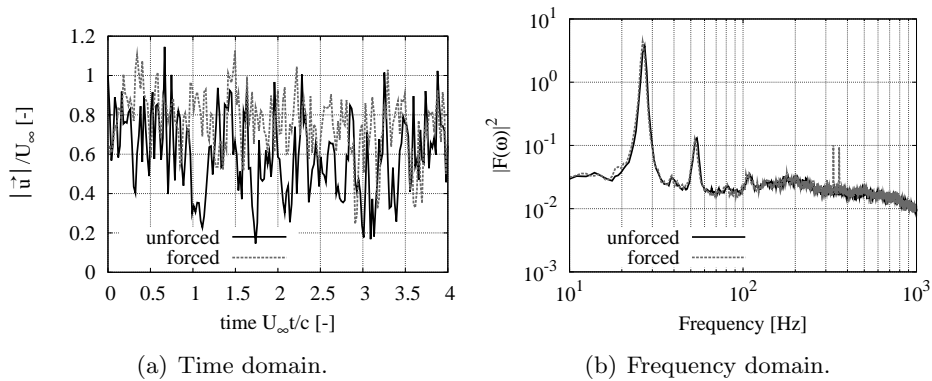


**Figure 6.23** – Time and frequency domain data for the airfoil with cavity A at  $Re_c = 4.4 \cdot 10^5$  and  $\alpha = +5^\circ$ . Without (unforced) and with an acoustic forcing of  $v'/U_\infty = 1.0 \cdot 10^{-2}$  (forced). Hot-wire position:  $(x/W, y/W) = (0.95, -0.055)$ .

At low Reynolds numbers  $Re_c = 3.3 \cdot 10^4$  there are clear peaks in the spectrum, but the shear layer does not respond to the acoustic forcing. Most likely this is due to a thick shear layer. In the range of Reynolds

numbers  $5.0 \cdot 10^4 \leq Re_c < 2 \cdot 10^5$  a clear peak in the power spectrum can be identified. In this range of Reynolds numbers the shear layer is sensitive to acoustic forcing. As soon as the acoustic forcing is switched on, even at extremely low amplitude ( $v'/U_\infty \approx 10^{-4}$ ), the shear layer immediately locks in at the forcing frequency. At higher Reynolds numbers the flow becomes turbulent and only a small peak in the spectrum with acoustic forcing can be identified, which is due to a superposition of the acoustic field. At these Reynolds numbers ( $Re_c < 5 \cdot 10^4$  or  $Re_c > 2 \cdot 10^5$ ) the shear layer does not respond to the acoustic forcing. The water channel experiments at  $Re_c = 2 \cdot 10^4$  indicated, however, that periodic flow perturbations will synchronise vortex shedding along the span of the cavity (figure 5.9). In contrast to the hot-wire data presented here, the excitation amplitude and the forcing frequency in the flow visualisation were not controlled nor measured. This calls for better conditioned flow visualisation experiments.

The measurement presented in this section have also been carried out for the airfoil with cavity *B*. The results of these experiments are similar to the results presented in this section. A summary of the data for cavity *B* can be found in Appendix F.

### 6.3.3 Unsteady flow

In section 6.2 the results of low Reynolds number numerical simulations with external forcing have been discussed for the airfoil without cavity and the airfoils with cavity *A* and cavity *B*. In this section the experimental results, at high Reynolds numbers, obtained with acoustic forcing, as described in Chapter 3 are presented for the airfoils with cavity *A* and cavity *B*.

Figures 6.24(a) and 6.24(b) show the amplitude and corresponding phase of  $\Delta C_{pu}$ , for the airfoil with cavity *A*, at  $x/c = 0.133$  as a function of the reduced frequency  $k$  for two different ranges of forcing amplitudes determined by lock-in. Note that the forcing amplitude varies as a function of the reduced frequency  $k$ , because we fix  $v'$  and vary  $U_\infty$ . It is observed that no significant amplitude dependence is present. It is remarkable that the amplitude dependence of the phase, which was observed for the airfoil without cavity (figure 3.19(b)) is not observed with cavity. We also repeated these experiments for different values of the angle of attack, yielding results that are similar to those shown in figures 6.24(a) and 6.24(b).

Because the airfoil with cavity *B* is equipped with more pressure transducers we can measure  $\Delta C_{pu}$  at multiple chordwise locations, namely  $x/c =$

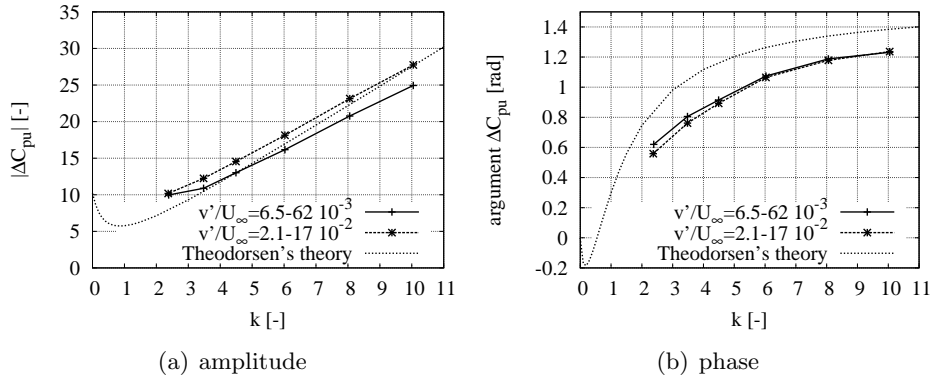


**Figure 6.24** – Experimental  $\Delta C_{pu}$  values at  $x/c = 0.133$ , as a function of the reduced frequency  $k$ , for cavity A for  $\alpha = 0^\circ$  and  $1.9 \cdot 10^5 < Re_c < 7.8 \cdot 10^5$ .

0.133,  $x/c = 0.49$  and  $x/c = 0.85$  (measured from the leading edge). The amplitude and phase at these difference chordwise locations are shown in figures 6.25 to 6.27. The figures 6.25(a) and 6.25(b) again show the ampli-

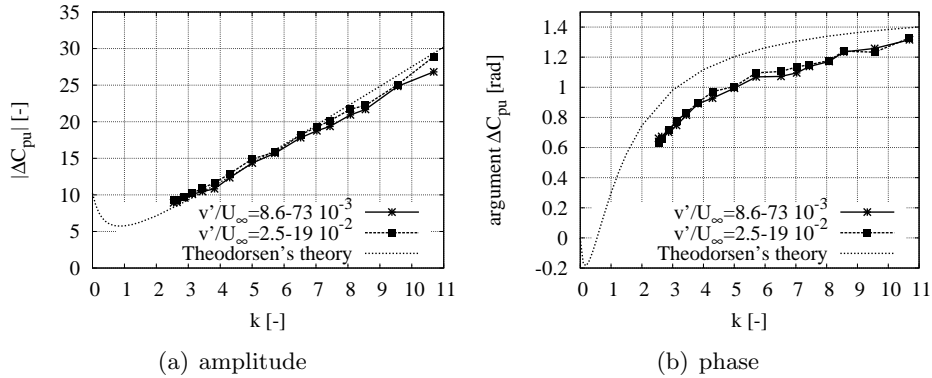


**Figure 6.25** – Experimental  $\Delta C_{pu}$  values at  $x/c = 0.133$ , as a function of the reduced frequency  $k$ , for cavity B for  $\alpha = 0^\circ$ ,  $1.8 \cdot 10^5 < Re_c < 7.8 \cdot 10^5$  and two different ranges of the forcing amplitude  $v'/U_\infty$ .

tude and phase at the forcing frequency for two different ranges of forcing amplitudes at  $x/c = 0.133$  for  $\alpha = 0^\circ$ , and again no significant effect of the amplitude is observed. Therefore the results at  $x/c = 0.49$  and at  $x/c = 0.85$  are only shown for one range of the forcing amplitude.

Figures 6.26(a) and 6.26(b) display the amplitude and corresponding phase of  $\Delta C_{pu}$  as a function of the reduced frequency, at  $x/c = 0.49$  for  $\alpha = 0^\circ$ . In figures 6.27(a) and 6.27(b) the amplitude and corresponding phase of  $\Delta C_{pu}$  are shown as a function of the reduced frequency, at  $x/c = 0.85$  and  $\alpha = 0^\circ$ .

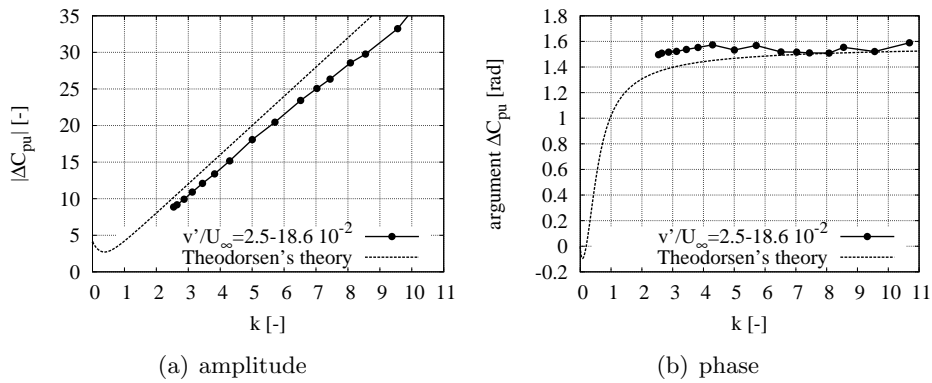


**Figure 6.26** – Experimental  $\Delta C_{pu}$  values at  $x/c = 0.49$ , as a function of the reduced frequency  $k$ , for cavity  $B$  for  $\alpha = 0^\circ$ ,  $1.8 \cdot 10^5 < Re_c < 7.8 \cdot 10^5$  and a forcing amplitude  $2.5 \cdot 10^{-2} \leq v'/U_\infty \leq 18.6 \cdot 10^{-2}$ .

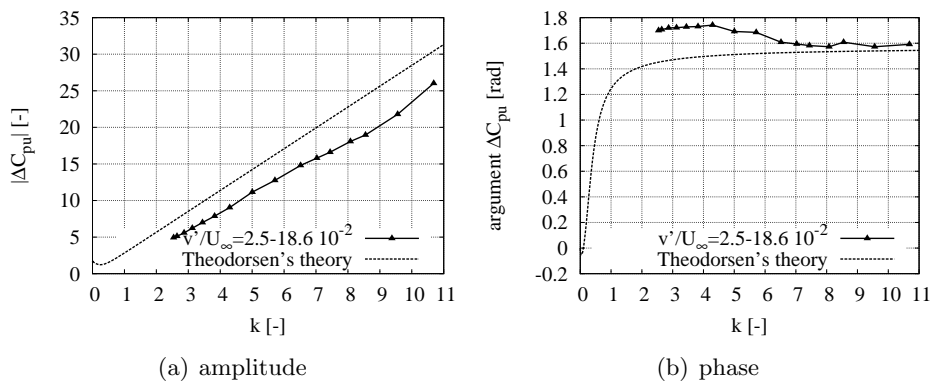


**Figure 6.27** – Experimental  $\Delta C_{pu}$  values at  $x/c = 0.85$ , as a function of the reduced frequency  $k$ , for cavity  $B$  at  $\alpha = 0^\circ$ ,  $1.8 \cdot 10^5 < Re_c < 7.8 \cdot 10^5$  and a forcing amplitude  $2.5 \cdot 10^{-2} \leq v'/U_\infty \leq 18.6 \cdot 10^{-2}$ .

## 6.4 Conclusion

Wind tunnel measurements have been presented for two different cavities ( $A$  and  $B$ ) with and without acoustic forcing. The presence of periodic vortex shedding was illustrated by calculation of the cross-correlations of surface pressures from numerical simulations. The cross-correlations of the experimentally obtained surface pressures at  $Re_c > 2 \cdot 10^5$  did not indicate such a periodic vortex shedding. At high positive angle of attack ( $\alpha = +15^\circ$ ) one peak was observed in the cross-correlation, which is expected to be due to the presence of broadband turbulence noise. At lower velocities the pressure transducers are not sensitive enough to detect vortices. We therefore used hot-wire anemometry. The use of hot-wire anemometry revealed the presence of a shear layer and allowed the determination of its oscillatory behaviour.

Numerical simulations for two-dimensional flow, based on the Navier–Stokes equations, at  $Re_c = 2 \cdot 10^4$  with external forcing showed that there are no significant deviations between an airfoil with and without cavity.

Experiments and simulations performed for both cavity shapes yield very similar results, which indicates that the flow is not sensitive to small changes in geometry. Placement of a cavity of the dimensions and geometry described in this thesis does not induce a significant deviation, for Strouhal numbers corresponding to vortex shedding of the cavity, in pressure coefficient and lift from the same clean airfoil or linear theory for a flat plate. The forces and pressure differences are mainly determined by the effect of the added mass of the airfoil.

Based on numerical results we conclude that for the case with forcing the pressure difference near the leading edge of the airfoil is not an accurate measure of the behaviour of the integrated lift force. When there is no forcing the local pressure difference at  $x/c = 0.133$  is a good indication for the integral lift coefficient.

The hot-wire measurements revealed the presence of the shear layer in the wind tunnel experiments, as expected from numerical simulations and water channel experiments at  $Re_c = 2 \cdot 10^4$ . At low Reynolds number,  $Re_c = 3.3 \cdot 10^4$ , the flow is laminar and clear oscillations are observed. The shear layer does not respond to the acoustic forcing. For Reynolds numbers in the range  $5 \cdot 10^4 < Re_c < 2 \cdot 10^5$  the shear layer is still laminar and displays the first and second shear layer modes. At these Reynolds numbers the shear layer is sensitive to acoustic forcing. For higher Reynolds numbers the flow becomes turbulent and the acoustic forcing has no apparent effect



on the shear layer oscillation.

The wind tunnel hot-wire and pressure measurements at  $Re_c = 4.4 \cdot 10^5$  do not indicate a periodic vortex shedding as observed in the two-dimensional numerical simulation and the flow visualisation at  $Re_c = 2 \cdot 10^4$ . This is likely due to the effects of turbulence, which are not represented in the numerical simulations.

## Chapter 7

# Conclusions

### Overview

The development of a new type of airfoil with a vortex trapped inside a cavity motivated our interest in the dynamic behaviour of such an airfoil. In order to carry out dynamical plunging measurements at such high values of the reduced frequency,  $k = \frac{\omega b}{U_\infty}$ , a new experimental approach has been developed. This method exploits the first acoustic transversal eigen mode of the wind tunnel test section. The airfoil is fixed to the wind tunnel wall while the flow is oscillating. In the conventional method the airfoil is oscillating. This new measurement method has been validated by means of experiments on a NACA0018 airfoil. Thereafter two NACA0018 airfoils with slightly different cavity geometries have been investigated in the wind tunnel. This includes dynamic pressure measurements on the airfoil and hot-wire measurements of the shear layer oscillations in the cavity. These wind tunnel experiments are complemented by numerical simulations using a method to solve the two-dimensional Navier–Stokes equations. In order to validate the numerical results and to gain more insight in the flow physics, flow visualisations have been performed in a water channel at the same Reynolds numbers for which the numerical simulations were carried out.

### New measurement method

For simulating the plunging motion of an airfoil the main fundamental difference between the new experimental method and the conventional method of physically moving the airfoil is the presence of a uniform time dependent pressure gradient, needed to accelerate the oscillating flow. With the new experimental method presented in Chapter 3 it is possible to reach high

values of the reduced frequency,  $2 < k < 10$ , which are difficult to reach with the conventional method. A strong point of the new measurement technique is that the forcing amplitude can easily be varied from extremely low amplitudes up to amplitudes of  $v'/U_\infty = O(10^{-1})$ . A weak point of the method is that due to the presence of the airfoil the acoustic field is localised around the airfoil and non-uniform. This limits the accuracy of the determination of the acoustic plunging velocity amplitude. A more uniform acoustic forcing could be achieved by lowering the Helmholtz number. This can be accomplished by reducing the ratio of the airfoil chord length and the test section width. On a standard airfoil the deviations between measured data and the results of linearised incompressible flow theory of Theodorsen are in our case mainly caused by the finite value of the Helmholtz number,  $He = \frac{\omega b}{c_\infty} \approx 0.5$ . This dependence on the Helmholtz number scales with  $He^2$ , so that a reduction of the chord by a factor of 2 would reduce this effect by a factor of 4.

### Failure of method based on Euler equations

For the case of a conventional airfoil without cavity, numerical solutions of the Euler equations yield results which are in good agreement with experiments. The Kutta condition at sharp edges, enforced by numerical dissipation, is in this case sufficient to obtain physically relevant solutions. However, when a cavity, with sharp edges, is placed in the airfoil the Euler solutions tend to a stable solution with uniform vorticity inside the cavity. This so-called Batchelor flow is not observed in our experiments. The lack of dissipation and slip allowed along the wall of the cavity are responsible for this unphysical solution. For the case of an airfoil with a cavity the Euler equations are therefore not suitable and numerical solutions based on the Navier–Stokes equations are necessary.

### Behaviour at low Reynolds number without external forcing

Experimental and numerical results presented in Chapters 4 and 5 show that for Reynolds numbers of the order of  $Re_c = 2 \cdot 10^4$ , a periodic vortex shedding results from the unstable shear layer passing over the cavity. Judging from experiments and two-dimensional numerical flow simulations, without external forcing, the effects of the cavity are noticeable. An asymmetry arises in the pressure distribution, which is not present for the same airfoil without cavity. The numerical simulations indicate that an airfoil

with cavity can have a higher aerodynamic efficiency, in terms of lift over drag ratio, compared to the same airfoil without cavity. These beneficial results are achieved for high positive angles of attack, for which the cavity breaks up the laminar separation bubble into small scale vortices. This reduces the width of the wake and therefore lowers the drag.

### Deviation from two-dimensional behaviour

Flow visualisations in the water channel, presented in Chapter 5, revealed the three-dimensionality of the cavity flow at low Reynolds number. When the airfoil is placed between two end plates Bödewadt boundary layers at the spanwise cavity ends drive a secondary flow in the cavity. In case one or two end plates are removed, or a small hole is present in the end plate of the cavity, the vortical flow is destroyed and a turbulent flow results. Our water channel experiments also demonstrate that at  $Re_c = 2 \cdot 10^4$  an oscillation of the flow synchronises the vortex shedding and enhances the two-dimensionality of the flow.

### Effect of external forcing on behaviour at low Reynolds number

The two-dimensional Navier–Stokes simulations, at low Reynolds numbers, with external forcing, indicate that in the range of reduced frequencies between  $1 < k < 15$  a cavity has no significant influence on the unsteady local pressure differences or on the unsteady forces on the airfoil. Deviations from Theodorsen’s theory are similar for airfoils with and without cavity. These numerical simulations do show that the local pressure difference,  $\Delta C_{pu}$ , at  $x/c = 0.133$  is not an accurate indication for the lift force if there is a significant separation of the boundary layer on the airfoil.

### Experiments at high Reynolds number

The high Reynolds number wind tunnel experiments ( $Re_c = 4 \cdot 10^5$ ) with applied acoustic forcing lead to the same conclusion as the numerical simulations: the cavity has no significant effect on the unsteady pressure difference. The frequencies at which the shear layer oscillates are so high that at these frequencies the dynamical behaviour of the airfoil is dominated by the added mass of the airfoil. Hot-wire measurements show that the shear layer oscillates and is sensitive to the acoustic forcing at Reynolds numbers in the range  $5 \cdot 10^4 < Re_c < 2 \cdot 10^5$ . At lower Reynolds numbers the shear layer does not respond to the acoustic forcing, most likely due to the thick

shear layer. At higher Reynolds numbers the shear layer becomes turbulent and the acoustic forcing has no effect on the shear layer either.

### Perspectives

For the cavity sizes we presented in this thesis we did not observe a significant effect of the cavity on the dynamical behaviour of the airfoil. However, if the ratio of cavity size to chord length is much higher than that of the airfoils presented in this thesis, the shear layer will oscillate at lower frequencies and we do expect significant effects of the cavity on the unsteady forces on the airfoil.

The application of the new experimental method, as described in Chapter 3, is not limited to airfoils. With this method the oscillating flow around any object can be studied, as long as the Helmholtz number  $He$  is small.

In order to simulate the flow over an airfoil with cavity at high Reynolds numbers a Large Eddy Simulations for three-dimensional flow are needed, as the results show that turbulent phenomena considerably modify the flow's behaviour.

## Appendix A

# Geometry of NACA0018 airfoils

The family of symmetric NACA profiles are derived from an analytical formula, which can be found in literature, see Abbott & von Doenhoff (1949), or Fletcher (1988). In  $x, y$ -coordinates the profile is given by the formula:

$$\begin{aligned}
 y(x) &= t (a_1\sqrt{x} + a_2x + a_3x^2 + a_4x^3 + a_5x^4), \quad 0 \leq x \leq 1 \quad (\text{A.1}) \\
 a_1 &= 1.4779155 \\
 a_2 &= -0.624424 \\
 a_3 &= -1.727016 \\
 a_4 &= 1.384087 \\
 a_5 &= -0.489769.
 \end{aligned}$$

The thickness is determined by the coefficient  $t$ , for a profile with a thickness of 18%  $t = 0.18$ . The formula above gives only the upper half of the profile, the lower half is easily obtained by reflection in the  $x$ -axis.

The NACA0018 profile used in the experiment is made out of aluminum and manufactured by extrusion. The chord length is 165 mm. The radius of curvature of the trailing edge is 0.5 mm. The geometric definition is given in figure A.1.

The profile with cavity is manufactured from the standard profile shown in figure A.1, a solid aluminum block was inserted in the middle chamber and the cavity was milled with a mill of 30 mm. diameter, milled at angle of 70 degrees with respect the chord line of the profile. The geometry definition

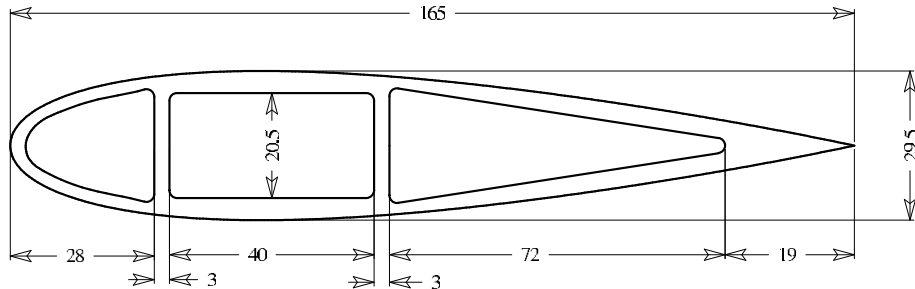


**Figure A.1** – Geometry definition of the standard NACA0018 profile used in the experiments. All dimensions in mm.

is given is figure A.2.

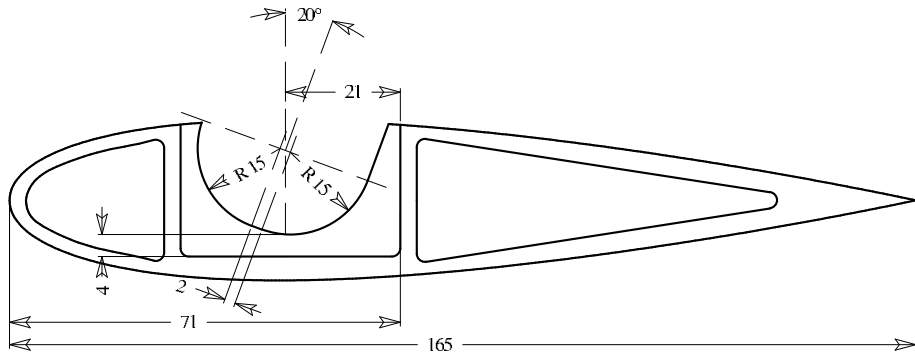


**Figure A.2** – Geometry definition of the standard NACA0018 profile with cavity A used in the experiments. All dimensions in mm.

The second profile with cavity has a rounded rear edge of the cavity and a replaceable strip at front edge of the cavity. The definition of the geometry is given in figure A.3.

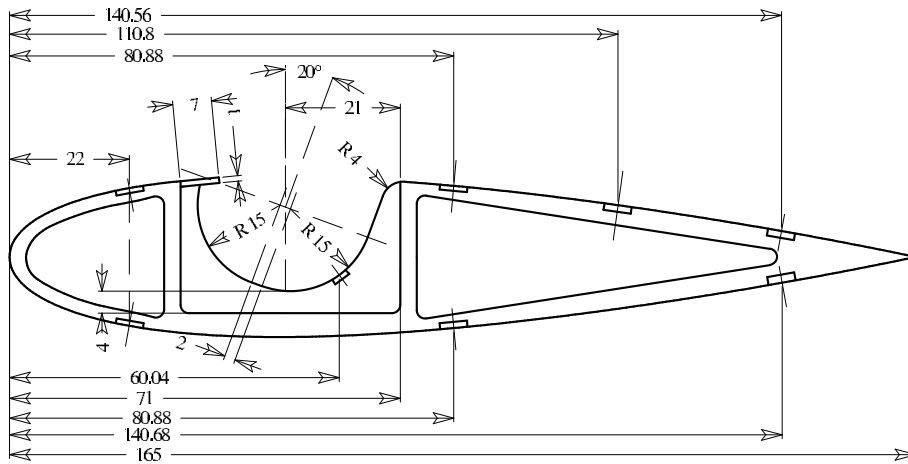


**Figure A.3** – Geometry definition of the standard NACA0018 profile with cavity *B* used in the experiments. All dimensions in mm.



## Appendix B

# Added mass of a flat plate

If an object is accelerated in a fluid the force required to give the object a certain acceleration is the sum of the force required to accelerate the mass of the object and the force required to accelerate the mass of the fluid around the object. This second mass is known as the added mass or virtual mass of an object and solely depends on the geometry of the object. In daily life we experience that moving your arms in air requires less force compared to moving your arms in water. This is mainly due to the added mass effect since the density of water is  $10^3$  times higher than that of air.

The added mass of an object can be calculated by means of potential flow theory. In this appendix we will calculate the added mass of a flat plate which is moving in a direction perpendicular to the plate. The thickness of the plate is taken to be zero.

Consider a flat plate with zero thickness moving in a flow, in the direction normal to the plate. The added mass term is due to the kinetic energy of the flow around the plate, this is certainly not zero.

The kinetic energy of a potential flow can be elegantly written as an integral over the surface of the body:

$$K = -\frac{1}{2}\rho \int_{\partial A} (\phi \nabla \phi) \cdot \vec{n} dA, \quad (\text{B.1})$$

see Batchelor (1967) (page 402-403), or:

$$K = -\frac{1}{2}\rho U_i \int_{\partial A} \phi n_i dA. \quad (\text{B.2})$$

Here  $\rho$  is the density of the fluid,  $U_i$  is the translational velocity of the

body,  $\phi$  is the velocity potential at the surface of the body and  $n_i$  is the normal of the surface element  $dA$ .

To find the flow around the plate we make use of the Joukowski transformation,  $z = \zeta + \frac{a^2}{\zeta}$ . This transformation transforms a circle with radius  $a$  in the complex  $\zeta$ -plane into a flat plate with zero thickness in the complex  $z$ -plane. Here  $\zeta = \xi + i\eta$  and  $z = x + iy$ . The plate lies on the  $x$ -axis between  $x = -2a$  and  $x = 2a$  in the  $z$ -plane. The derivative of the transformation is

$$\frac{dz}{d\zeta} = 1 - \frac{a^2}{\zeta^2} \quad (\text{B.3})$$

$$\frac{d\zeta}{dz} = \frac{\zeta^2}{\zeta^2 - a^2}. \quad (\text{B.4})$$

The complex potential  $F$  for the flow around the circle of radius  $a$  in the  $\zeta$ -plane, can be found with the use of the Circle theorem of Milne-Thompson

$$F(\zeta) = -iU\zeta + \frac{iUa^2}{\zeta}. \quad (\text{B.5})$$

This is the complex potential of the flow around the flat plate placed in a parallel flow along the  $y$ -axis with free stream velocity  $U$  and flowing around the stationary circle in the  $\zeta$ -plane. The kinetic energy of this flow is infinite since the circle is stationary and the fluid velocity at infinite distance from the circle has a constant value  $U$ . We need the solution of the flow around a circle moving in a quiescent fluid. In order to obtain this potential we add a uniform flow with velocity  $-Ui$  in the  $z$ -plane. Now the potential becomes

$$F(\zeta) = -iU\zeta + \frac{iUa^2}{\zeta} + iUz \quad (\text{B.6})$$

$$F(\zeta) = -iU\zeta + \frac{iUa^2}{\zeta} + iU\left(\zeta + \frac{a^2}{\zeta}\right) \quad (\text{B.7})$$

$$F(\zeta) = \frac{i2Ua^2}{\zeta}. \quad (\text{B.8})$$

The surface of the plate corresponds to the surface of the circle in the transformed plane. Therefore the complex potential on the surface of the circle is given by

$$F(\zeta)|_{\zeta=ae^{i\theta}} = \frac{i2Ua^2}{ae^{i\theta}} = \frac{i2Ua^2ae^{-i\theta}}{ae^{i\theta}ae^{-i\theta}} = i2Ua(\cos\theta - i\sin\theta). \quad (\text{B.9})$$

So on the surface of the plate the velocity potential is given by

$$\phi|_{surface} = 2Ua \sin \theta, \quad (\text{B.10})$$

where  $\theta$  is related to  $x$  by  $x = 2a \cos \theta$  and so  $dx = -2a \sin \theta d\theta$ .

The integral to be evaluated is

$$-\frac{1}{2}\rho U \int_{x=-2a}^{x=2a} \phi(x, y) n_i dx \quad (\text{B.11})$$

$$\begin{aligned} \frac{1}{2}\rho U \int_{\theta=0}^{\theta=2\pi} i2Ua \sin \theta \ 2a \sin \theta d\theta &= \frac{1}{2}\rho 4U^2 a^2 \int_{\theta=0}^{\theta=2\pi} \sin^2 \theta d\theta = \dots \\ &= \frac{1}{2}\rho 4U^2 a^2 \pi = \frac{1}{2}\rho \frac{\pi c^2}{4} U^2. \end{aligned} \quad (\text{B.12})$$

Therefore the added mass (per unit length in the  $z$ -direction) of a flat plate with zero thickness is given by  $M' = \rho \frac{\pi c^2}{4}$  where  $c = 4a$  is the chord of the plate and  $\rho$  is the density of the fluid.

It is also possible to consider the total kinetic energy of the fluid in motion. This involves the calculation of the integral

$$\frac{1}{2}\rho \int_S |u|^2 dx dy, \quad (\text{B.13})$$

where  $S$  is the fluid domain. The integral can be evaluated by transforming the integral to the  $\zeta$ -plane.

$$u - iv = \frac{dF}{d\zeta} \frac{d\zeta}{dz} = \frac{-2iUa^2}{\zeta^2 - a^2} \quad (\text{B.14})$$

$$|u - iv|^2 = \frac{4U^2 a^4}{(\xi^2 - \eta^2 - a^2)^2 + 4\xi^2 \eta^2} \quad (\text{B.15})$$

$$z = x + iy = \zeta + \frac{a^2}{\zeta} = \xi + i\eta + \frac{a^2(\xi - i\eta)}{\xi^2 + \eta^2} \quad (\text{B.16})$$

$$x = \xi + \frac{a^2 \xi}{\xi^2 + \eta^2} \quad (\text{B.17})$$

$$y = \eta - \frac{a^2 \eta}{\xi^2 + \eta^2} \quad (\text{B.18})$$

$$J = \frac{\partial x}{\partial \xi} \frac{\partial y}{\partial \eta} - \frac{\partial x}{\partial \eta} \frac{\partial y}{\partial \xi} = \frac{a^4 + 2a^2(\eta^2 - \xi^2)}{(\eta^2 + \xi^2)^2} + 1 \quad (\text{B.19})$$

$$\xi = r \cos \theta \quad (\text{B.20})$$

$$\eta = r \sin \theta \quad (\text{B.21})$$

$$\frac{1}{2}\rho \int_S |u|^2 dx dy = \frac{1}{2}\rho \int_{r=a}^{\infty} \int_{\theta=0}^{2\pi} |u(r, \theta)|^2 J(r, \theta) r d\theta dr. \quad (\text{B.22})$$

The integral can be evaluated and yields the same result as before.

It is also possible to calculate the local pressure difference over the plate as a result of the added mass effect. In this case

$$\Delta p = \rho \frac{\Delta\phi}{\partial t}, \quad (\text{B.23})$$

where  $\Delta\phi$  is the difference in the value of the velocity potential between upper and lower surface of the plate,  $\rho$  the density. The velocity potential is the real part of the complex velocity potential and is easily computed from equation (B.10). The difference in velocity potential is then given by

$$\Delta\phi = -4aU \sin\theta, \quad \text{with } 0 \leq \theta \leq \pi. \quad (\text{B.24})$$

If the potential has a simple harmonic time dependence ( $e^{i\omega t}$ ), its time derivative is

$$\frac{\Delta\phi}{\partial t} = -4i\omega aU \sin\theta, \quad \text{with } 0 \leq \theta \leq \pi \quad (\text{B.25})$$

Note that  $c = 4a$

$$\Delta p = -i\rho\omega U c \sin\theta. \quad (\text{B.26})$$

The total force due to the added mass can be calculated by integrating the pressure difference along the plate. Using  $x = 2a \cos\theta$ , such that  $dx = -2a \sin\theta d\theta$ ,

$$F = \int_{\theta=0}^{\pi} \frac{1}{2} i\rho\omega U c^2 \sin^2\theta d\theta = i\pi\rho\omega U \frac{c^2}{4}, \quad (\text{B.27})$$

which is equal to the product of added mass times the acceleration of the plate. The remarkable fact is that the added mass of a flat plate with chord  $c$  is exactly the same as that of a circular cylinder of diameter  $c$ , also the pressure difference distribution is exactly the same.

## Appendix C

# Kármán–Trefftz airfoil

In section 2.3 in Chapter 2 the Von Kármán–Trefftz transformation is used to estimate the effects of finite airfoil thickness. The details of the mapping and derivations discussed are given in this appendix. The Von Kármán–Trefftz (K-T) transformation is a conformal mapping that can be used to map a circle in the  $\zeta$ -plane to an airfoil with a finite trailing edge angle in the physical  $z$ -plane. The mapping is given by

$$\frac{z - 2a}{z + 2a} = \left( \frac{\zeta - a}{\zeta + a} \right)^n, \quad (\text{C.1})$$

where  $z = x + iy$  and  $\zeta = \xi + i\eta$ . (Note that for  $n = 2$  the well-known Joukowski mapping from a circle with radius  $a$  centered at the origin in the  $\zeta$ -plane to a plate between  $x = -2a$  and  $x = 2a$ , in the  $z$ -plane is obtained.) Equation (C.1) can also be written as

$$z(\zeta) = 2a \frac{1 + f(\zeta)}{1 - f(\zeta)}, \quad \text{with} \quad f(\zeta) = \left( \frac{\zeta - a}{\zeta + a} \right)^n. \quad (\text{C.2})$$

This equation maps the circle  $\zeta = -\varepsilon a + Re^{j\theta}$ , with  $R = (1 + \varepsilon)a$  and  $\varepsilon$  real, to a symmetric airfoil with a finite trailing edge angle in the  $z$ -plane. For these symmetric airfoils  $a$  is given by

$$a = \frac{c}{4} \left( \frac{-1 + \left(\frac{1+\varepsilon}{\varepsilon}\right)^n}{\left(\frac{1+\varepsilon}{\varepsilon}\right)^n} \right). \quad (\text{C.3})$$

The geometry of the airfoil is determined by the values of  $\varepsilon$  and  $n$ . A close approximation of the NACA0018 airfoil is obtained for  $\varepsilon = 0.12$  and  $n = 1.93$ . In figure C.1 the K-T airfoil is plotted (for  $\varepsilon = 0.12$  and  $n = 1.93$ ), along with the NACA0018 airfoil.

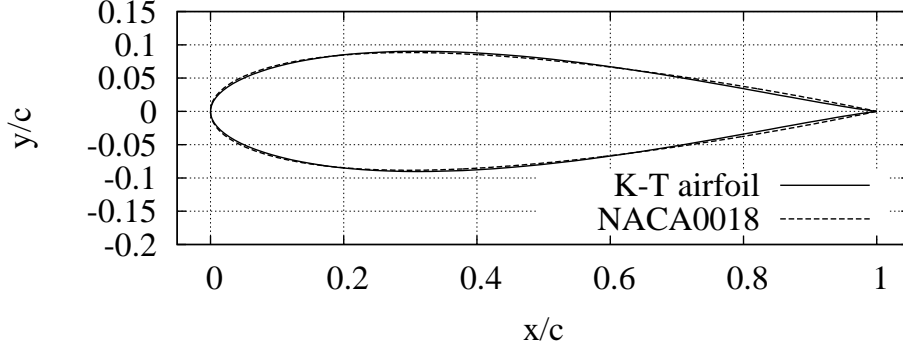


Figure C.1 – Von Kármán–Trefftz airfoil and the NACA0018 airfoil.

## C.1 Quasi-steady solution

To calculate the quasi-steady pressure difference we need to compute the velocity at the airfoil surface, from which the pressure difference is then computed using the Bernoulli equation. The complex potential in the  $\zeta$ -plane is

$$F(\zeta) = U(\zeta - \zeta_c)e^{-i\alpha} + \frac{UR^2}{\zeta - \zeta_c}e^{i\alpha} + \frac{i\Gamma}{2\pi} \ln(\zeta - \zeta_c) \quad (\text{C.4})$$

where  $\zeta_c = \varepsilon a$ . The value of  $\Gamma$  is determined by the Kutta condition imposed at the trailing edge

$$\Gamma = 4\pi RU \sin \alpha. \quad (\text{C.5})$$

The square of the velocity in the  $z$ -plane is computed from the complex potential as

$$|u - iv|^2 = (u - iv)(u + iv) = \frac{dF}{dz} \cdot \overline{\frac{dF}{dz}} = \frac{dF}{d\zeta} \cdot \overline{\frac{dF}{d\zeta}} \cdot \frac{d\zeta}{dz} \cdot \overline{\frac{d\zeta}{dz}}. \quad (\text{C.6})$$

The non-dimensional dynamical pressure difference can be calculated from the Bernoulli equation:

$$\Delta C_{pu} = \frac{2\Delta p}{\rho U_\infty^2 \frac{v'}{U_\infty}} = \frac{|\vec{u}_{up}|^2}{U_\infty v'} - \frac{|\vec{u}_{low}|^2}{U_\infty v'}. \quad (\text{C.7})$$

For small values of  $\alpha$  we can write  $\alpha = v'/U$ . For a K-T airfoil with  $\varepsilon = 0.12$  and  $n = 1.93$  the non-dimensional pressure difference  $\Delta C_{pu}$  can be computed for  $0 < \theta < \pi$ .

## C.2 Added mass

In order to compute the pressure difference over the airfoil due to the added mass we compute the instantaneous potential around the airfoil when moving upwards at constant velocity. The pressure difference can then be computed from the unsteady Bernoulli equation. The complex instantaneous potential of the flow around the K-T airfoil moving upwards with velocity  $U$  can be found in the  $\zeta$ -plane and is given by

$$F = \phi + j\psi = -jU(\zeta - \zeta_c) + jU \frac{R^2}{(\zeta - \zeta_c)} + iUz. \quad (\text{C.8})$$

Note that we add a flow in the negative  $y$ -direction in the physical  $z$ -plane. The unsteady Bernoulli equation reads

$$\rho \frac{\partial \phi}{\partial t} + \frac{1}{2} \rho |\vec{u}|^2 + p = \text{constant}. \quad (\text{C.9})$$

Since we will be dealing with a symmetric airfoil and we are only interested in the pressure difference on corresponding points on the lower and upper surface, the velocities at these corresponding points will have the same magnitude. Therefore the Bernoulli equation simplifies to

$$\Delta p = p_{low} - p_{up} = \rho \frac{\partial \Delta \phi}{\partial t}. \quad (\text{C.10})$$

Since we are considering harmonic time dependence we can replace the time derivative with  $i\omega$ .

$$\Delta p = i\omega \rho \Delta \phi. \quad (\text{C.11})$$

We do not need the derivative of the mapping because the potential is invariant under conformal mapping. The difference in velocity potential is easily calculated by putting  $\zeta = (1 + \varepsilon)ae^{j\theta} - \varepsilon a$  and  $\zeta_c = -\varepsilon a$  and taking the real part of equation (C.8).

For a K-T airfoil with  $\varepsilon = 0.12$  and  $n = 1.93$  13.3% of the chord corresponds to  $\theta = 2.3468$  and the pressure difference  $\Delta p = -0.638i\omega \rho cU$ . Previously we obtained for the flat plate  $\Delta p = -i\omega \rho cU \sin \theta$  and here 13.3% of the chord corresponds to  $\theta = 2.395$ , which yields  $\Delta p = -0.679i\omega cU$ .

From this we can conclude that the pressure difference at  $x/c = 0.133$  due to the added mass of a K-T airfoil, which closely resembles the NACA0018 airfoil, is 6% lower than a flat plate with the same chord length.

## Appendix D

# Pressure difference without Kutta condition

In section 2.4 of Chapter 2 the force on a flat plate in an oscillating flow is discussed. Here no Kutta condition is applied, and the only force acting on the plate is due to the added mass of the plate. In this appendix we derive the pressure difference over the plate by the use of complex potential.

The complex potential is given by

$$\Phi = U_\infty \left( \zeta + \frac{R^2}{\zeta} \right) - \tilde{v} \cos \omega t \left( j\zeta - \frac{jR^2}{\zeta} \right). \quad (\text{D.1})$$

Here  $\zeta = \xi + j\eta$ . The complex velocity in the physical  $z$ -plane ( $z = x + jy$ ) is computed from  $\frac{d\Phi}{d\zeta} \cdot \frac{d\zeta}{dz}$  and is given by

$$u - jv = \frac{d\Phi}{d\zeta} \cdot \frac{d\zeta}{dz} = \left[ U_\infty \left( 1 - \frac{R^2}{\zeta^2} \right) - \tilde{v} \cos \omega t \left( j + \frac{jR^2}{\zeta^2} \right) \right] \frac{\zeta^2}{\zeta^2 - R^2}. \quad (\text{D.2})$$

On the surface of the cylinder, which corresponds to the surface of the plate,  $\zeta = Re^{j\theta}$  and

$$|\vec{u}|^2 = (u - jv)(u + jv) = \frac{d\Phi}{d\zeta} \cdot \frac{d\zeta}{dz} \cdot \overline{\frac{d\Phi}{d\zeta}} \cdot \overline{\frac{d\zeta}{dz}} = \left( U_\infty - \tilde{v} \frac{\cos(\omega t)}{\tan \theta} \right)^2. \quad (\text{D.3})$$

The velocity potential  $\phi$  is the real part of the complex velocity potential  $\Phi$  and is given by

$$\phi = U_\infty \left( \xi + \frac{R^2 \xi}{\xi^2 + \eta^2} \right) + \tilde{v} \cos \omega t \left( \eta + \frac{R^2 \eta}{\xi^2 + \eta^2} \right). \quad (\text{D.4})$$



The time derivative of equation (D.4) is given by

$$\frac{\partial \phi}{\partial t} = -\omega \tilde{v} \sin \omega t \left( \eta + \frac{R^2 \eta}{\xi^2 + \eta^2} \right). \quad (\text{D.5})$$

Substitution of  $\xi = R \cos \theta$  and  $\eta = R \sin \theta$  (valid on the cylinder surface), yields

$$\frac{\partial \phi}{\partial t} = -2R\omega \tilde{v} \sin(\omega t) \sin \theta. \quad (\text{D.6})$$

Application of the unsteady Bernoulli equation to calculate the pressure difference gives

$$\Delta p = p(-\theta) - p(\theta) = \rho \frac{\partial(\phi(\theta) - \phi(-\theta))}{\partial t} + \frac{\rho}{2} (|\vec{u}(\theta)|^2 - |\vec{u}(-\theta)|^2) \quad (\text{D.7})$$

$$\Delta p = -4R\rho\omega \tilde{v} \sin(\omega t) \sin \theta - 2\rho U_\infty \tilde{v} \frac{\cos(\omega t)}{\tan \theta}. \quad (\text{D.8})$$

In non-dimensional form

$$\frac{2\Delta p}{\rho U_\infty \tilde{v}} = -8R \frac{\omega}{U_\infty} \sin \omega t \sin \theta - 4 \frac{\cos \omega t}{\tan \theta}. \quad (\text{D.9})$$

Note that  $2R = b$  with  $b$  the semi chord of the plate ( $b = c/2$ ), so that

$$\frac{2\Delta p}{\rho U_\infty \tilde{v}} = -4 \frac{\omega b}{U_\infty} \sin \omega t \sin \theta - 4 \frac{\cos \omega t}{\tan \theta}. \quad (\text{D.10})$$

The minus sign in the first term comes from differentiation of  $\cos \omega t$  with respect to time. We can also write the non-dimensional pressure difference in the complex  $e^{i\omega t}$  notation as

$$\frac{2\Delta p}{\rho U_\infty \tilde{v}} = \Re \left[ \left( 4i \frac{\omega b}{U_\infty} t \sin \theta - \frac{4}{\tan \theta} \right) e^{i\omega t} \right]. \quad (\text{D.11})$$

## Appendix E

# Lock-in method

Throughout this thesis the lock-in method is used to extract the amplitude and phase of a signal in the time domain. This appendix gives a description of this lock-in method.

In case a system is excited with a known periodic excitation it is possible to extract from the output signal the amplitude and phase of the frequency component which corresponds to that of the excitation signal. This is known as a lock-in method.

In general a periodic function of time  $f(t)$  can be written as a Fourier series:

$$f(t) = \frac{1}{2}a_0 + \sum_{n=1}^{\infty} [a_n \cos(\omega_n t) + b_n \sin(\omega_n t)], \quad (\text{E.1})$$

with  $a_n$  and  $b_n$  the Fourier coefficients and  $\omega_n$  the frequency in rad/s. The coefficients of the Fourier series are given by

$$a_0 = \frac{2}{T} \int_0^T f(t) dt \quad (\text{E.2})$$

$$a_n = \frac{2}{T} \int_0^T f(t) \cos(\omega_n t) dt \quad (\text{E.3})$$

$$b_n = \frac{2}{T} \int_0^T f(t) \sin(\omega_n t) dt. \quad (\text{E.4})$$

$\frac{1}{2}a_0$  is the average of the function  $f(t)$  over one period. With the lock-in method one only solves the Fourier series for the first components of the

series:

$$f(t) = \frac{1}{2}a_0 + [a_1 \cos(\omega t) + b_1 \sin(\omega t)] \quad (\text{E.5})$$

where  $\omega$  now corresponds to the frequency of the input signal that is attempted to identify in the signal  $f(t)$ . The sum of a  $\sin(\omega t)$  and  $\cos(\omega t)$  function is also a periodic function with frequency  $\omega$ :

$$\begin{aligned} a \cos(\omega t) + b \sin(\omega t) &= \text{Re}\{(a - ib)e^{i\omega t}\} = \quad (\text{E.6}) \\ \text{Re}\{\sqrt{a^2 + b^2}e^{i \arctan(b/a)} e^{i\omega t}\} &= \text{Re}\{\sqrt{a^2 + b^2}e^{i(\omega t + \arctan(b/a))}\} = \\ \sqrt{a^2 + b^2} \cos(\omega t + \arctan(b/a)) &= \sqrt{a^2 + b^2} \sin(\omega t + \arctan(b/a) + \frac{\pi}{2}) \end{aligned}$$

Note that in the numerical implementation the  $\arctan 2(y, x)$  function should be used. With the use of the lock-in method it is possible to extract the amplitude and phase of one frequency component out of a signal.

In practice one should use the real driving signal as a reference signal. The complex conjugate of the signal can be found by means of a Hilbert transformation. Since the electronic function generator is not infinitely accurate the frequency it produces may shift during time. By using the real signal of the function generator this shift is automatically taken into account in the analysis.

## Appendix F

# Hot-wire measurements for cavity $B$

In this appendix the data of the hot-wire measurements on cavity  $B$  are presented. Figure F.1 shows the time-averaged velocity profile over the shear layer for  $\alpha = +5^\circ$  and  $Re_c = 3.3 \cdot 10^4$ . The magnitude of the velocity is made non-dimensional with the free stream velocity  $U_\infty$ . This velocity  $U_\infty$  is measured for  $\alpha = 0^\circ$  with the hot-wire at  $(\frac{x}{W}, \frac{y}{W}) = (1.7, 1.8)$ . We see that the shear layer has an approximate thickness of 3 mm and the air inside the cavity is almost stagnant.

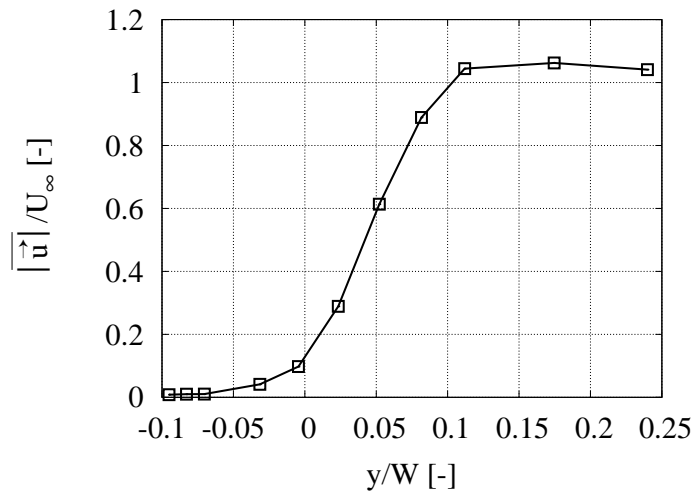


**Figure F.1** – Mean velocity profile across the shear layer over cavity  $B$  as a function of  $y/W$ , for  $Re_c = 3.3 \cdot 10^4$ ,  $\alpha = +5^\circ$  and  $0.72 < x/W < 0.97$ .

At a Reynolds number of  $Re_c = 3.3 \cdot 10^4$  we observe a laminar type of flow signal, with a distinct peak in the frequency domain. Figures F.2 to F.8 show the hot-wire signal on the left and the power spectrum on the right for different values of  $\alpha$ . The magnitude of the velocity is made non-dimensional with the free stream velocity  $U_\infty$  and time is made non-dimensional with the free stream velocity and the chord length of the airfoil  $c$ . At each angle of attack the hot-wire is positioned such that  $0.2 \leq |\bar{u}|/U_\infty \leq 0.7$ , which will ensure that the hot-wire is inside the shear layer. For  $\alpha = +5^\circ$  in figure F.3 also the hot-wire signal and power spectrum are shown with an acoustic forcing of  $v'/U_\infty = 1.5 \cdot 10^{-2}$ . The hot-wire signal is sampled with a frequency of 12 kHz and the power spectra are obtained by FFT and averaging over approximately 150 windows, with 50% overlap, of 1.3 seconds, with a Hanning window applied on each window.

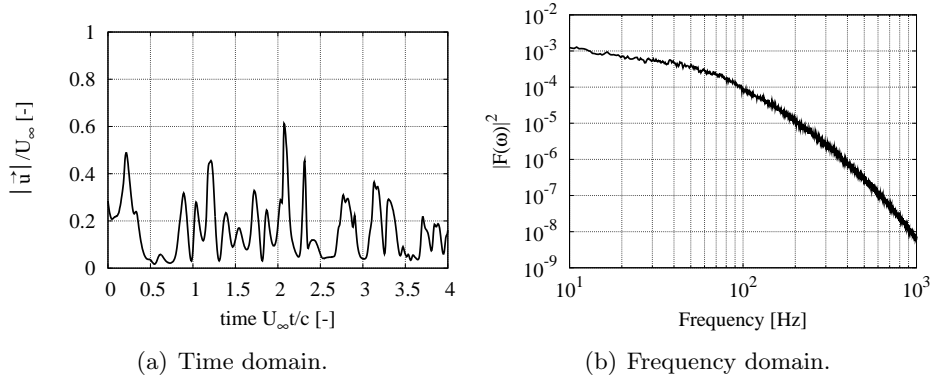


**Figure F.2** – Time and frequency domain data for the airfoil with cavity  $B$  at  $Re_c = 3.3 \cdot 10^4$  and  $\alpha = +10^\circ$ . Hot-wire position:  $(x/W, y/W) = (0.70, 0.15)$ . No acoustic forcing.

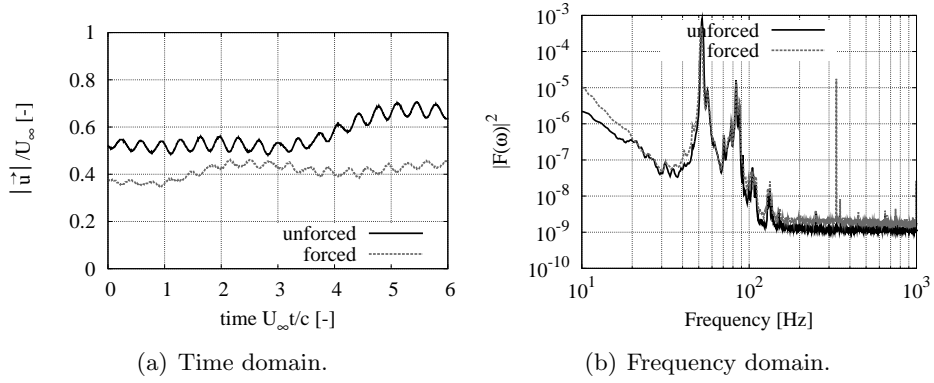


**Figure F.3** – Time and frequency domain data for the airfoil with cavity *B* at  $Re_c = 3.3 \cdot 10^4$  and  $\alpha = +5^\circ$ . Hot-wire position:  $(x/W, y/W) = (0.80, 0.08)$ . Without acoustic forcing (unforced) and with an acoustic forcing of  $v'/U_\infty = 1.5 \cdot 10^{-2}$  (forced).

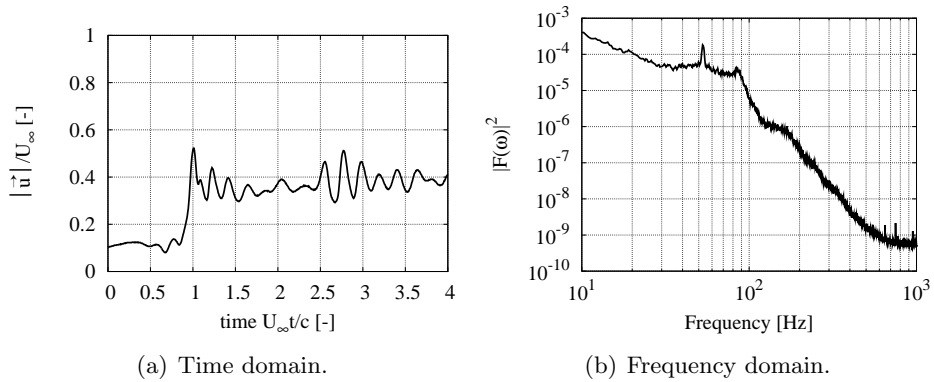


**Figure F.4** – Time and frequency domain data for the airfoil with cavity *B* at  $Re_c = 3.3 \cdot 10^4$  and  $\alpha = +3^\circ$ . Hot-wire position:  $(x/W, y/W) = (0.88, 0.0020)$ . No acoustic forcing.

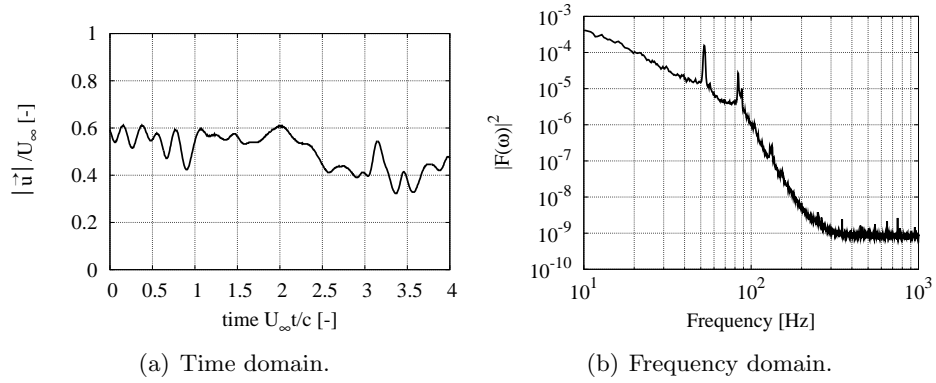


**Figure F.5** – Time and frequency domain data for the airfoil with cavity  $B$  at  $Re_c = 3.3 \cdot 10^4$  and  $\alpha = 0^\circ$ . Hot-wire position:  $(x/W, y/W) = (0.90, -0.018)$ . No acoustic forcing.

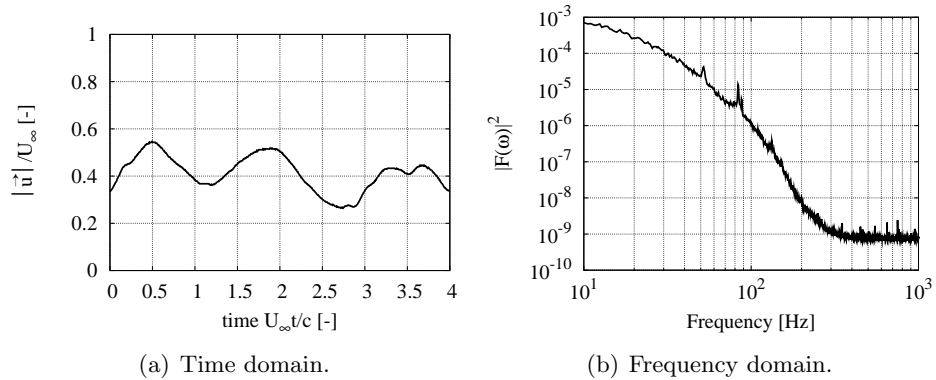


**Figure F.6** – Time and frequency domain data for the airfoil with cavity  $B$  at  $Re_c = 3.3 \cdot 10^4$  and  $\alpha = -3^\circ$ . Hot-wire position:  $(x/W, y/W) = (0.92, -0.039)$ . No acoustic forcing.

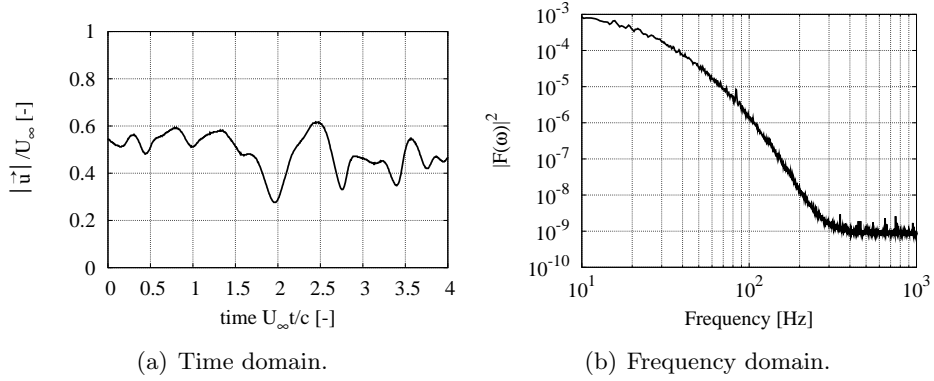


**Figure F.7** – Time and frequency domain data for the airfoil with cavity *B* at  $Re_c = 3.3 \cdot 10^4$  and  $\alpha = -5^\circ$ . Hot-wire position:  $(x/W, y/W) = (0.92, -0.039)$ . No acoustic forcing.

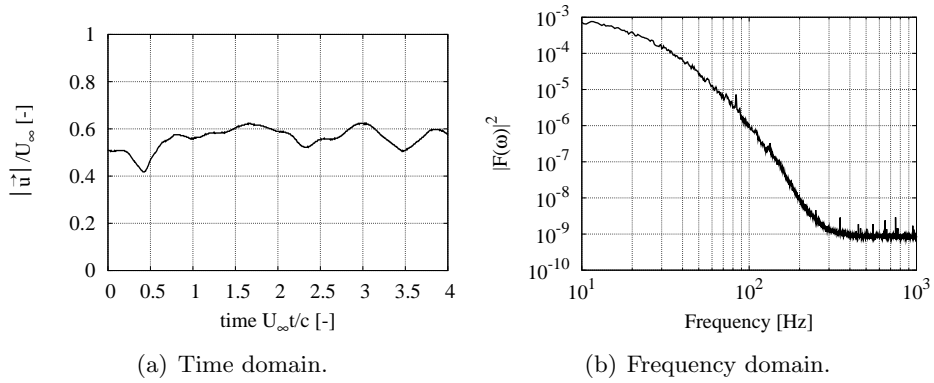


**Figure F.8** – Time and frequency domain data for the airfoil with cavity *B* at  $Re_c = 3.3 \cdot 10^4$  and  $\alpha = -10^\circ$ . Hot-wire position:  $(x/W, y/W) = (0.93, -0.045)$ . No acoustic forcing.



We observe that the shear layer oscillation without acoustic forcing is more intense for positive angles of attack than for negative  $\alpha$ -values. For  $\alpha = +10^\circ$  no peak in the spectrum is present. Most likely the flow is separated upstream of the cavity and turbulent. For  $\alpha = +5^\circ$  a clear peak at 54 Hz is observed, corresponding to a Strouhal number based on the width of the cavity opening of  $St_W = \frac{fW}{U_\infty} = 0.6$ , which indicates the presence of the first shear layer mode. We also observe a low peak at 85 Hz, corresponding to  $St_W = 0.96$ , which may indicate the second shear layer mode. With the acoustic forcing switched on a large peak at the forcing frequency of 332 Hz appears, but the peaks at 54 Hz and 85 Hz remain. Also the hot-wire signals with and without acoustic forcing are very similar. This is an indication that the shear layer is not very sensitive to the acoustic forcing, which might be due to the low Reynolds number and the corresponding thick shear layer. Without acoustic forcing we also observe peaks in the spectral density at 54 Hz and 85 Hz at the other values of  $\alpha$ .

Figure F.9 shows the hot-wire signal and power spectrum for  $\alpha = +5^\circ$  and  $Re_c = 6.3 \cdot 10^4$ , both without acoustic forcing and with an acoustic forcing of  $v'/U_\infty = 7.9 \cdot 10^{-3}$ . Without acoustic forcing a low peak at 160 Hz

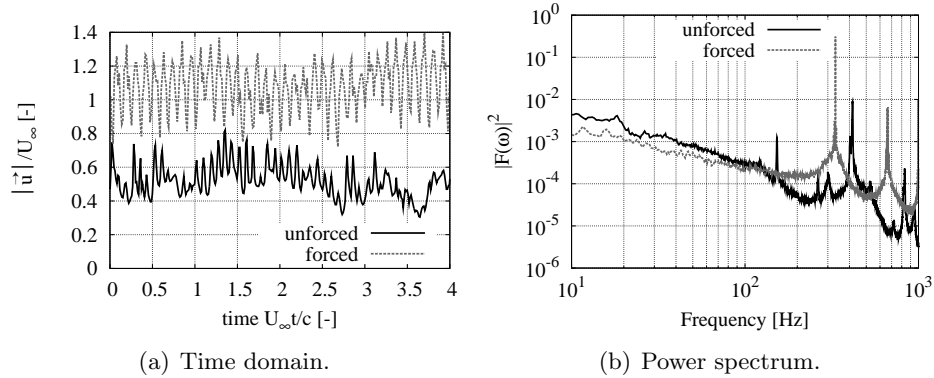


**Figure F.9** – Time and frequency domain data for the airfoil with cavity  $B$  at  $Re_c = 6.3 \cdot 10^4$  and  $\alpha = +5^\circ$ , without acoustic forcing (unforced) and with an acoustic forcing of  $v'/U_\infty = 7.9 \cdot 10^{-3}$  (forced). Hot-wire position:  $(x/W, y/W) = (0.88, 0.0026)$ .

is observed and a high peak at 417 Hz, which correspond to  $St_W = 0.95$  and  $St_W = 2.5$ , respectively. With the acoustic forcing switched on the peaks at 160 Hz and 417 Hz disappear and large peaks at the forcing frequency of 332 Hz and its higher harmonic at 664 Hz appear. Here the shear layer clearly locks in at the forcing frequency, which results in  $St_W = 2$ . Also the

hot-wire signals are quite different, with the acoustic forcing switched on the mean velocity increases and the amplitude of the oscillations is higher. At this Reynolds number ( $Re_c = 6.3 \cdot 10^4$ ) This lock-in of the shear layer to the forcing frequency happens for forcing amplitudes above  $v'/U_\infty = 4.9 \cdot 10^{-4}$ . In the spectrum with acoustic forcing there also appears a peak at 4 Hz, which is most likely an acoustic resonance of the entire wind tunnel.

Figure F.10 shows the time signal and power spectrum for  $\alpha = +5^\circ$  and  $Re_c = 1.0 \cdot 10^5$ . The data is shown for the cases without acoustic forcing and with an acoustic forcing of  $v'/U_\infty = 5.3 \cdot 10^{-3}$ . Here a high peak at 8 Hz is

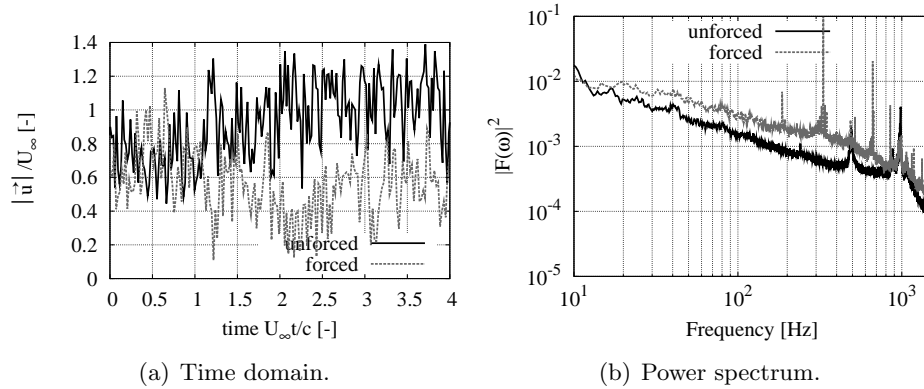


**Figure F.10** – Time and frequency domain data for the airfoil with cavity  $B$  at  $Re_c = 1.0 \cdot 10^5$  and  $\alpha = +5^\circ$ . Without acoustic forcing (unforced) and with an acoustic forcing of  $v'/U_\infty = 5.3 \cdot 10^{-3}$  (forced). Hot-wire position:  $(x/W, y/W) = (0.88, 0.0026)$ .

present, both with and without acoustic forcing. This peak is probably due to an acoustic resonance of the entire wind tunnel. Without acoustic forcing we also observe two oscillations of the shear layer at 490 Hz and 980 Hz, which correspond to  $St_W = 1.8$  and  $St_W = 3.7$ , respectively. With acoustic forcing we observe a low peak at 186 Hz and high peaks at the forcing frequency of 332 Hz and its higher harmonics. We also observe peaks at 490 Hz and 980 Hz, which were also present without the acoustic forcing. The hot-wire signals with and without acoustic forcing are very similar.

Figure F.11 shows the time signal and power spectrum for  $\alpha = +5^\circ$  and  $Re_c = 4.4 \cdot 10^5$  for the cases without acoustic forcing and with an acoustic forcing of  $v'/U_\infty = 3.4 \cdot 10^{-3}$ . At this Reynolds number the boundary layer is likely to be turbulent upstream of the cavity. In figure F.11(a) both hot-wire signals appear very similar with and without acoustic forcing. Also the power

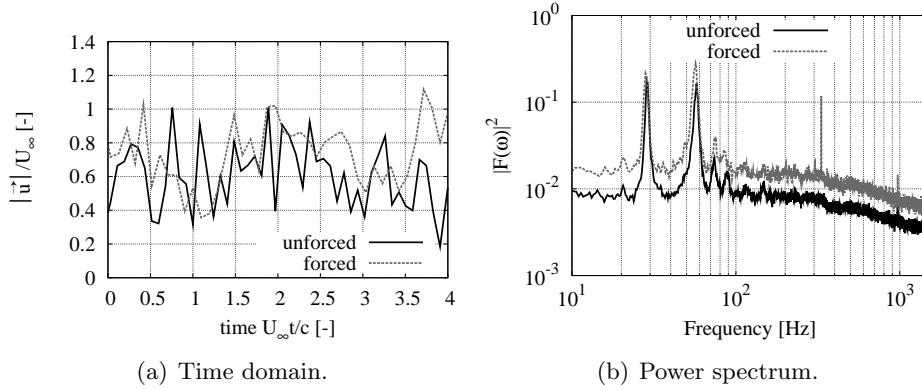


**Figure F.11** – Time and frequency domain data for the airfoil with cavity  $B$  at  $Re_c = 4.4 \cdot 10^5$  and  $\alpha = +5^\circ$ . Without acoustic forcing (unforced) and with an acoustic forcing of  $v'/U_\infty = 3.4 \cdot 10^{-3}$  (forced). Hot-wire position:  $(x/W, y/W) = (0.95, -0.055)$ .

spectra are very similar, except for the high peak at the forcing frequency of 332 Hz. In both spectra two peaks at 28 Hz and 57 Hz are observed, which are again most likely due to an acoustic wind tunnel resonance. Also a small peak at 970 Hz is observed in both spectra, corresponding to  $St_W = 0.82$ .

## Bibliography

- ABBOTT, I.H. & VON DOENHOFF, A.E. 1949 *Theory of Wing Sections*. Dover Publications. 131
- ARCHIBALD, F.S. 1975 The laminar boundary layer instability excitation of an acoustic resonance. *J. Sound Vib.* **38**, 387–402. 35
- BALAKRISHNAN, A.V. 1999 *Unsteady Aerodynamics-Subsonic Compressible Inviscid Case*. CR-1999-206583. NASA. 28
- BARANOV, P.A., GUVERNYUK, S.V., ZUBIN, M.A. & ISAEV, S.A. 2000 Numerical and physical modeling of the circulation flow in a vortex cell in the wall of a rectilinear channel. *J. Fluid Mech.* **35**, 663–673. 2
- BATCHELOR, G.K. 1956*a* A proposal concerning laminar wakes behind bluff bodies at large Reynolds number. *J. Fluid Mech.* **1**, 388–398. 65
- BATCHELOR, G.K. 1956*b* On steady laminar flow with closed stream lines at large Reynolds number. *J. Fluid Mech.* **1**, 177–190. 65
- BATCHELOR, G.K. 1967 *An Introduction to Fluid Dynamics*. Cambridge University Press. 8, 56, 134
- BLEVINS, R.D. 1979 *Formulas for Natural Frequency and Mode Shape*. Van Nostrand Reinhold Company. 43
- BÖDEWADT, U.T. 1940 Die Drehströmung über festem Grunde. *ZAMM* **20**, 241–245. 93
- BRÈS, G.A. & COLONIUS, T. 2008 Three-dimensional instabilities in compressible flow over open cavities. *J. Fluid. Mech.* **599**, 309–339. 63, 95

- BUNYAKIN, A.V., CHERNYSHENKO, S.I. & STEPANOV, G.YU. 1996 Inviscid Batchelor-model flow past an aerofoil with a vortex trapped in a cavity. *J. Fluid Mech.* **323**, 367–376. 62
- BUNYAKIN, A.V., CHERNYSHENKO, S.I. & STEPANOV, G.YU. 1998 High-Reynolds-number Batchelor-model asymptotics of a flow past an aerofoil with a vortex trapped in a cavity. *J. Fluid Mech.* **358**, 283–297. 62
- CHERNYSHENKO, S.I., GALLETTI, B., IOLLO, A. & ZANNETTI, L. 2003 Trapped vortices and a favourable pressure gradient. *J. Fluid Mech.* **482**, 235–255. 62
- COLONIUS, T. & TAIRA, K. 2008 A fast immersed boundary method using a nullspace approach and multi-domain far-field boundary conditions. *Comput. Meth. Appl. Mech. Eng.* **197**, 2131–2146. 29, 68
- DEQUAND, S. 2000 *Duct Aeroacoustics: from Technological Applications to the Flute*. PhD thesis, Eindhoven University of Technology. 63
- DOWLING, A.P. & FLOWCS WILLIAMS, J.E. 1983 *Sound and Sources of Sound*. Cambridge University Press. 39, 40
- DRAZIN, P. & REID, W. 1981 *Hydrodynamic Stability*. Cambridge University Press. 94
- FLETCHER, C.A.J. 1988 *Computational Techniques for Fluid Dynamics 2*. Springer. 131
- FLETCHER, C.A.J. & STEWART, G.D.H. 1986 Bus drag reduction by the trapped vortex concept for a single bus and two buses in tandem. *J. Wind Eng. Ind. Aerod.* **24**, 143–168. 2
- FUNG, Y.C. 1955 *An Introduction to the Theory of Aeroelasticity*. Dover Publications. 3, 8, 13, 57
- GHARIB, M. & ROSHKO, A. 1987 The effect of flow oscillations on cavity drag. *J. Fluid Mech.* **177**, 501–530. 3
- GÖRTLER, H. 1941 Instabilität laminarer Grenzschichten an konkaven Wänden gegenüber gewissen dreidimensionalen Störungen. *ZAMM* **21**, 250–252. 94

- GREENGARD, C. 1985 The core spreading vortex method approximates the wrong equation. *J. Comput. Phys.* **61**, 345–348. 24
- HALFMAN, R.L. 1952 *Experimental Aerodynamic Derivatives of a Sinusoidally Oscillating Airfoil in Two-Dimensional Flow*. Report 1108. NACA. 34
- HOFMANS, G.C.J. 1998 *Vortex Sound in Confined Flows*. PhD thesis, Eindhoven University of Technology. 118
- HUANG, M.K. & CHOW, C.Y. 1982 Trapping a free vortex by Joukowski airfoils. *AIAA J.* **20**, 292–298. 2
- HULSHOFF, S.J. 2000 *EIA: an Euler Code for Internal Acoustics. Part 1: Method Description and User's Guide*. Technical Report. Eindhoven University of Technology. 25
- ISAEV, S.A., GUVERNYYUK, S.V., ZUBIN, M.A. & PRIGORODOV, YU.S. 2000 Numerical and physical modeling of a low-velocity air flow in a channel with a circular vortex cell. *J. Eng. Phys. Thermophys.* **73**, 337–343. 2
- JACOBS, E.N. & SHERMAN, A. 1937 *Airfoil Section Characteristics as affected by Variations of the Reynolds Number*. Report 586. NACA. 74, 75
- JACOBS, S.J., HOSPERS, J.M. & HOEIJMAKERS, H.W.M. 2008 Numerical simulation of ice accretion on multiple-element airfoil sections. In *ICAS 2008, 26th international congress of the aeronautical sciences, Anchorage, AK*. 53
- JONES, W.P. 1957 *Wind-tunnel Interference Effects on Oscillating Aerofoils in Subsonic Flow*. R. and M. No. 2943. A.R.C. Technical Report. 22
- JONES, W.P. 1958 *Wind-Tunnel Interference Effects on Measurements of Aerodynamic Coefficients for Oscillating Aerofoils*. R. and M. No. 2786. A.R.C. Technical Report. 22
- KRUPPA, E.W. 1977 A wind tunnel investigation of the Kasper vortex concept. *AIAA* (115704). 2

- LAFON, P., CAILLAUD, S., DEVOS, J.P. & LAMBERT, C. 2003 Aeroacoustical coupling in a ducted shallow cavity and fluid/structure effects on a steam line. *J. Fluid. Struct.* **18**, 695–713. 63
- LANDAU, L.D. & LIFSHITZ, E.M.Y.C. 1959 *Fluid Mechanics, Vol. 6*. Dover Publications. 39
- LARCHEVÊQUE, L., SAGAUT, P. & LABBÉ, O. 2007 Large-eddy simulation of a subsonic cavity flow including asymmetric three-dimensional effects. *J. Fluid. Mech.* **577**, 105–126. 63
- LARCHEVÊQUE, L., SAGAUT, P., MARY, I., LABBÉ, O. & COMTE, P. 2003 Large-eddy simulation of a compressible flow past a deep cavity. *Phys. Fluids* **15**, 193–211. 94
- LEE, I. 1988 Plenum chamber effect on wind-tunnel resonance by the finite element method. *AIAA J.* **29**, 1087–1093. 35
- LEWIS, R.I. 1991 *Vortex Element Methods for Fluid Dynamic Analysis of Engineering Systems*. Cambridge University Press. 24
- LIEPMANN, H.W. 1943a *Investigations on Laminar Boundary Layer Stability and Transition on Curved Boundaries*. W-107. NACA Wartime Report. 94, 95
- LIEPMANN, H.W. 1943b *Investigations on Laminar Boundary Layer Stability and Transition on Curved Boundaries*. Rm 7302. ARC. 94, 95
- LIN, J. & ILIFF, K.W. 2000 *Aerodynamic Lift and Moment Calculations Using a Closed-Form Solution of the Possio Equation*. TM-2000-209019. NASA. 28
- MCWILLIAMS, J.C. 1984 The emergence of isolated coherent vortices in turbulent flow. *J. Fluid. Mech.* **146**, 21–43. 30
- MICHALKE, A. 1965 On spatially growing disturbances in an inviscid shear layer. *J. Fluid Mech.* **23**, 521–544. 77
- MOSHER, M. 1986 *The Influence of Wind-Tunnel Walls on Discrete Frequency Noise*. PhD thesis, Stanford University. 35, 39
- NAKANO, T., FUJISAWA, N. & LEE, S. 2006 Measurement of tonal-noise characteristics and periodic flow structure around NACA0018 airfoil. *Exp. Fluids* **40**, 482–490. 72, 74

- PARKER, R. 1967 Resonance effect in wake shedding from parallel plates: calculation of resonant frequencies. *J. Sound Vib.* **5**, 330–343. 47
- ROCKWELL, D. & NAUDASHER, E. 1978 Self-sustained oscillations of flow past cavities. *Trans. ASME: J. Fluid Eng.* **100**, 152–165. 2, 4, 77
- ROCKWELL, D. & NAUDASHER, E. 1979 Self-sustained oscillations of impinging free shear layers. *Annu. Rev. Fluid Mech.* **11**, 67–94. 2, 4
- ROSSOW, V.J. 1978 Lift enhancement by an externally trapped vortex. *J. Aircraft* **15**, 618–625. 2
- SAFFMAN, P.G. 1992 *Vortex Dynamics*. Cambridge University Press. 23
- SAFFMAN, P.G. & SHEFFIELD, J.S. 1977 Flow over a wing with an attached free vortex. *Stud. Appl. Maths* **57**, 107–117. 2
- SAVELSBERG, R. & CASTRO, I.P. 2008 Vortex flow in open cylindrical-section cavities. *Exp. Fluids* **46**, 485–497. 93, 95
- SCHEWE, G., MAI, H. & DIETZ, G. 2003 Nonlinear effects in transonic flutter with emphasis on manifestation of limit cycle oscillations. *J. Fluid. Struct.* **18**, 3–22. 34
- SCHLICHTING, H. 1968 *Boundary-Layer Theory*. McGraw-Hill, sixth edition. 94
- SEARS, W.R. & VON KÁRMÁN, TH. 1938 Airfoil theory for non-uniform motion. *J. Aeronautical Sci.* **5**, 379–390. 8, 15
- STREETER, V.L. 1961 *Handbook of Fluid Mechanics*. McGraw-Hill. 8, 56
- SUBRAMANIAM, S. 1996 *A New Mesh-Free Vortex Method*. PhD thesis, Florida State University. 24
- SYSNOISE 2005 by LMS International, Rev. 5.6. 41
- TAIRA, K. & COLONIUS, T. 2007 The immersed boundary method: a projection approach. *J. Comput. Phys.* **225**, 2118–2137. 29, 68
- THEODORSEN, TH. 1935 *General Theory of Aerodynamic Instability and the Mechanism of Flutter*. Report 496. NACA. 4, 5, 8



- TIMMAN, R. 1951 The aerodynamic forces on an oscillating aerofoil between two parallel walls. *Appl. Sci. Res.* **A3**, 31–57. 22
- TIMMER, W.A. 2008 Two-dimensional low-Reynolds number wind tunnel results for airfoil NACA0018. *Wind Eng.* **32**, 525–537. 74, 75
- VIRTUAL OSCILLATION - 2D 2006 version 1.1.0, College Master Hands, Inc. <http://www.cmhands.com>. 24, 25
- VORTEXCELL2050 2005 The VortexCell2050 project funded by the European Commission within its FP6 Programme, contract number AST4-CT-2005-012139 (more information available at [www.vortexcell2050.org](http://www.vortexcell2050.org)). 34
- ZAMAN, K.B.Q. 1992 Effect of acoustic excitation on stalled flows over an airfoil. *AIAA J.* **30**, 1492–1499. 35
- ZAMAN, K.B.M.Q., MCKINZIE, D.J. & RUMSEY, C.L. 1989 A natural low-frequency oscillation of the flow over and airfoil near stall conditions. *J. Fluid Mech.* **202**, 403–442. 74

# Summary

## Influence of a cavity on the dynamical behaviour of an airfoil

A new wing design has been the subject of study in the European project VortexCell2050. For several reasons (structural and fuel load) it is desirable to use relatively thick wings. However, thick wings promote flow separation and/or massive vortex shedding, reducing flight performance. The new design airfoil is equipped with a cavity (“vortex cell”) in the wing in order to prevent massive flow separation. This thesis aims to obtain insight into the dynamical behaviour of such a wing with a cavity and to explore which numerical methods are suitable for estimating the unsteady forces.

In this thesis experiments and computations are presented, using a geometry that was inspired by cavity shapes which are considered in the VortexCell2050 project. For an airfoil with a cavity, oscillations of the shear layer are expected at Strouhal numbers of order unity, based on the width of the cavity opening. For the size of the cavities considered this implies high values,  $O(10)$ , of the reduced frequency, based on the chord length of the airfoil. In order to conduct experiments in this high reduced frequency range, a new experimental method has been developed. In this experimental setup the airfoil is fixed to the wind tunnel wall and the first acoustic transversal eigenmode of the wind tunnel test section is used to drive an oscillating flow. In the conventional method the airfoil is oscillating. The main fundamental difference between the two methods is the presence of a time dependent uniform pressure gradient, which drives the oscillating flow, in the new method. The results obtained with both methods are equivalent after correcting for an effective buoyancy force induced by this driving

pressure gradient. The new method avoids the use of a complex mechanical system to drive the oscillation of the airfoil. The acoustical forcing amplitude is very easy to vary within two orders of magnitude. The method appears to be most suitable for the conduction of experiments at high values of the reduced frequency.

The new measurement method is validated by means of experiments on a standard NACA0018 airfoil complemented with two-dimensional Euler simulations. Thereafter two airfoils with slightly different cavity geometries are investigated in the wind tunnel. These experiments consist of measurements of local surface pressures.

For the case of an airfoil with a cavity the Euler equations are not suitable. Two-dimensional simulations using the frictionless flow approximation approach a so-called Batchelor flow, with a uniform rotation in the cavity. This flow is not observed in experiments.

For this reason two-dimensional incompressible Navier–Stokes simulations at a Reynolds number, based on the chord length of the airfoil, of  $2 \cdot 10^4$  are performed and indicate shear layer oscillations. In order to validate these low Reynolds number numerical results and to gain more insight in the flow physics, flow visualisations are performed in a waterchannel at the same Reynolds numbers as the numerical simulations. The visualisations also show oscillations of the shear layer at the first and second hydrodynamic mode, this is confirmed by hot-wire measurements in the wind tunnel at low Reynolds numbers. The hot-wire measurements also demonstrate that the expected lock-in of the shear layer does occur in a limited range of Reynolds numbers, based on the chord, sufficiently low such that no turbulence is generated, but higher than a critical value.

Experiments and two-dimensional Navier–Stokes simulations indicate that for values of the reduced frequency, in the range of 2–10, no significant deviations in the unsteady lift force occur between an airfoil with cavity and the same airfoil without cavity. The cavity does display shear layer oscillations around the expected Strouhal numbers, however, the associated fluctuations in the lift coefficient appear to be negligible. For the geometries considered the pressure differences over the airfoil are dominated by the added mass of the airfoil.

# Samenvatting

## Invloed van een caviteit op het dynamisch gedrag van een vleugelprofiel

Binnen het Europese VortexCell2050 project is een nieuwe vleugel onderzocht. Het heeft verschillende voordelen om grote vliegtuigen uit te rusten met dikke vleugels (structurele stijfheid en brandstofcapaciteit). Echter, dikke vleugels vergroten het risico op loslating van de stroming en grootschalige wervelafschudding, wat de aerodynamische efficiëntie negatief beïnvloed. De nieuwe vleugel is voorzien van een caviteit (“wervel cel”) in de vleugel om grootschalige wervelafschudding te voorkomen. Het doel van dit proefschrift is om inzicht te verkrijgen in het dynamisch gedrag van een vleugel met caviteit en te bepalen welke numerieke methoden geschikt zijn om de instationaire krachten op deze vleugel te berekenen.

In dit proefschrift worden experimenten en berekeningen gepresenteerd, waarbij gebruik is gemaakt van een geometrische vorm die geïnspireerd is door de geometrische vormen die binnen het VortexCell2050 project zijn beschouwd. Voor een vleugel met caviteit worden oscillaties van de schuiflaag verwacht bij een Strouhalgetal van orde één, gebaseerd op de breedte van de opening van de caviteit. Voor de afmetingen van de caviteiten die zijn overwogen impliceert dit hoge waarden,  $O(10)$ , van de gereduceerde frequentie, gebaseerd op de koorde lengte van het vleugelprofiel. Voor het uitvoeren van experimenten bij deze hoge waarden van de gereduceerde frequentie is een nieuwe experimentele methode ontwikkeld. In deze experimentele opstelling is het vleugelprofiel gefixeerd aan de wand van de windtunnel en wordt de eerste akoestische transversale eigenmode van de testsectie gebruikt om een oscillerende stroming op te wekken. Bij de conventionele methode oscilleert het vleugelprofiel. Het voornaamste funda-

mentele verschil tussen de twee methoden is de aanwezigheid van een tijdsafhankelijke uniforme drukgradiënt, die de oscillerende stroming opwekt. De resultaten verkregen met beide methoden zijn equivalent na correctie voor een effectieve draagkracht die wordt veroorzaakt door deze tijdsafhankelijke drukgradiënt. De nieuwe methode vereist geen gecompliceerd mechanisch systeem om het vleugelprofiel te laten oscilleren. De amplitude van de akoestische oscillatie is gemakkelijk te variëren in een bereik van tenminste twee ordes van grootte. De nieuwe methode is het meeste geschikt voor experimenten bij hoge waarden van de gereduceerde frequentie.

De nieuwe meetmethode is gevalideerd met experimenten aan een standaard NACA0018 profiel zonder caviteit, aangevuld met twee-dimensionale Euler berekeningen. Vervolgens zijn twee vleugelprofielen met kleine verschillen in de vorm van de caviteit onderzocht in de windtunnel. Hierbij zijn de drukken aan het oppervlak van het profiel gemeten.

Voor een vleugelprofiel met caviteit zijn de Euler vergelijkingen niet geschikt. Twee-dimensionale berekeningen, waarbij de aanname van een wrijvingsloze stroming wordt gedaan, benaderen een zogenaamde Batchelor stroming met uniforme rotatie in de caviteit. Deze stroming is niet waargenomen in experimenten.

Om de bovengemelde reden zijn incompressibele Navier–Stokes berekeningen uitgevoerd bij een Reynoldsgetal van  $2 \cdot 10^4$ , betrokken op de koorde van het profiel. De berekeningen vertonen schuiflaag oscillaties. Ter validatie van deze numerieke resultaten en om meer inzicht te verkrijgen in de stroming, zijn stromingsvisualisaties uitgevoerd in een waterkanaal. De visualisaties laten ook schuiflaag oscillaties zien en dit is bevestigd door hittedraadmetingen in de windtunnel bij lage Reynoldsgetallen. De hittedraadmetingen demonstreren ook dat de verwachte lock-in van de schuiflaag zich manifesteert in een beperkt gebied van Reynoldsgetallen, boven een kritische waarde, maar voldoende laag, zodat er geen turbulentie optreedt.

Experimenten en twee-dimensionale Navier–Stokes berekeningen impliceren dat voor hoge waarden van de gereduceerde frequentie, in het gebied 2–10, geen significante afwijkingen optreden tussen een vleugelprofiel met caviteit en hetzelfde profiel zonder caviteit. De schuiflaag boven de caviteit oscilleert bij de verwachte waarden van het Strouhalgetal. Echter, de hiermee samengaande oscillaties in de liftcoëfficiënt zijn verwaarloosbaar. Voor de caviteiten met de afmetingen die hier beschouwd zijn is het drukverschil over het vleugelprofiel gedomineerd door de toegevoegde massa van het profiel.

# Dankwoord

De laatste twee bladzijden van dit proefschrift wil ik graag gebruiken om mensen die mij geholpen hebben bij de totstandkoming van dit proefschrift te bedanken.

GertJan, Ruben en Mico wil ik bedanken voor het bieden van de mogelijkheid om mijn promotie onderzoek te doen in Eindhoven, hun begeleiding en suggesties. Hierbij noem ik Mico in het bijzonder. Beste Mico jouw ideeën en vele jaren ervaring met het uitvoeren van experimenten hebben een zeer belangrijke bijdrage geleverd aan dit proefschrift. Ook wist jij me telkens weer te motiveren na een mislukt experiment of na ontvangst van de zoveelste negatieve reactie van een reviewer.

De meeste in dit proefschrift toegepaste numerieke codes heb ik niet zelf ontwikkeld. De ontwikkeling van dit soort tools is vaak een promotie onderzoek opzich. Daarom ben ik voor het gebruik van numerieke codes (en de daarbij behorende ondersteuning) vooral veel dank verschuldigd aan Steven Hulshoff, Edwin van der Weide, Christophe Schram en Tim Colonius.

Reeds aan het begin van mijn promotie heb ik aan mijn begeleiders aangegeven dat het me leuk leek om voor een langere tijd in het buitenland te verblijven. Aan bezoeken aan het buitenland (13 stuks in totaal) heeft het dan ook niet geschort tijdens mijn promotietraject. En aan het begin van mijn vierde jaar deed zich (dankzij Mico en Harry) de mogelijkheid voor om een aantal maanden door te brengen aan The California Institute of Technology bij Prof. Tim Colonius. Ik wil hem en de mensen van The Computational Flow Physics Group hartelijk bedanken voor hun gastvrijheid en hulp binnen en buiten Caltech (Cheryl, Keita, Arnab, Kristjan, Won Tae, Jeff, Shusuke, Vedran, Toshiyuki, Jen).

Het opzetten/ontwikkelen van een nieuwe meetmethode brengt onvermijdelijk (onvoorziene) problemen met zich mee. Bij het oplossen hiervan

heb ik telkens op de steun kunnen rekenen van de technische staf, waaronder Freek, Gerald, Ad, Eric en Henny. Hierbij noem ik in het bijzonder Jan W. voor zijn grote bijdragen aan de ontwikkeling van de meetopstelling en het bouwen van de meetvleugels.

Mijn stagiar Alex en mijn twee afstudeerstudenten Marlies en Ries bedank ik voor hun bijdragen aan mijn onderzoek en dit proefschrift.

Zoals veel van mijn collega promovendi (met uitzondering van Laurens) had ook ik last van desk entropy. Gelukkig leek dit probleem bij mij altijd nog beheersbaar vergeleken bij dat van mijn kamergenoot Matías. Ik hoop dat zijn desk entropy geen super exponentiële groei zal aannemen na het vrijkomen van mijn bureau. Voor de goede werksfeer binnen Cascade bedank ik mijn (ex)collega promovendi en de vaste staf, in willekeurige volgorde: Devis, Rudie, Laurens, Rinie, Werner, Ralf, Marleen, Petra, Gerben, Vincent, Daniel, Ergün, Lorenzo, Francisco, Geert, Jorge, Berend, Gunes, Herman C., Rini, Leon, Jan L., Willem, Jos, Jens, Anton en Harry.

Voor hulp bij zaken van zeer uiteenlopende aard kon ik altijd rekenen op de secretaresses van Cascade: Marjan, Anita, en Brigitte.

Als laatste wil ik mijn ouders, mijn kleine zus en Linda bedanken voor al hun onvoorwaardelijke steun in de afgelopen vier jaar.

# Curriculum Vitae

6 January 1981	Born in Hilversum, The Netherlands
1993-1999	VWO Goois Lyceum Bussum, The Netherlands
1999-2005	Mechanical Engineering University of Twente Enschede, The Netherlands
2005	Project Engineer Hanzehogeschool Groningen, The Netherlands
2006-2010	PhD candidate Vortex dynamics and Turbulence group Department of Applied Physics Eindhoven University of Technology Eindhoven, The Netherlands



